A Neural-network-based Solver for the Three Dimensional Shape of Vesicle Membranes

by

Yousef Rohanizadegan

A thesis
presented to the University of Waterloo
in fulfillment of the
thesis requirement for the degree of
Doctor of Philosophy
in
Physics

Waterloo, Ontario, Canada, 2025

© Yousef Rohanizadegan 2025

Examining Committee Membership

The following served on the Examining Committee for this thesis. The decision of the Examining Committee is by majority vote.

External Examiner:	Greg van Anders Associate Professor, Dept. of Physics, Queen's University
Supervisor(s):	Jeff Z. Y. Chen Professor, Dept. of Phyiscs and Astronomy, University of Waterloo
Internal Member:	Bae-Yeun Ha Professor, Dept. of Phyiscs and Astronomy, University of Waterloo
Internal-External Member:	Pierre-Nicholas Roy Professor, Dept. of Chemistry, University of Waterloo
Other Member(s):	David Yevick Professor, Dept. of Phyiscs and Astronomy, University of Waterloo

Author's Declaration

This thesis consists of material all of which I authored or co-authored: see Statement of Contributions included in the thesis. This is a true copy of the thesis, including any required final revisions, as accepted by my examiners.

I understand that my thesis may be made electronically available to the public.

Statement of Contributions

This thesis has 6 chapters and is written based on 2 co-authored papers:

1. Chapter 4: **Yousef Rohanizadegan**, Hong Li, and Jeff Z. Y. Chen. Soft Matter, 20:5359–5366, 2024.

2. Chapter 5: **Yousef Rohanizadegan**, and Jeff Z. Y. Chen. Physics-informed deep learning for shapes of phospholipid vesicles in hard-wall confinements. In preparation.

As first author, I conducted research, collected results, implemented analysis, and drafted manuscripts.

Abstract

A neural-network-based numerical solver is developed for computing three-dimensional (3D) equilibrium shapes of deformable biomembranes, specifically phospholipid vesicles modeled by Helfrich's curvature elasticity theory. The solver represents vesicle morphology using a phase-field formulation, in which a scalar field distinguishes the interior and exterior of the vesicle through a diffuse interface. The phase field is parameterized by a compact feedforward neural network, and the equilibrium shape is obtained by direct minimization of the Helfrich bending energy subject to global surface-area and volume constraints, enforced via Lagrange multipliers. Automatic differentiation is used to evaluate all spatial derivatives, thereby avoiding finite-difference truncation errors and explicit surface discretization.

This framework produces both axisymmetric and fully non-axisymmetric vesicle shapes without imposing symmetry assumptions. Canonical free-space branches, namely prolates, oblates, and stomatocytes, are reproduced, and the classical bending-energy–reduced-volume diagram is recovered in close quantitative agreement with established results in the literature. In addition, a phase-field expression for the bilayer area-difference constraint is derived and incorporated into the solver, providing a numerical setting for the computation of non-axisymmetric equilibrium morphologies in free space.

A major contribution of this work is a systematic investigation of vesicle morphology under confinement. Vesicles are studied within a range of hard-wall geometries, including cylindrical (tube), slit, spherical, and cubic confinements. By varying confinement size and reduced volume, the solver captures a rich spectrum of deformations, including biaxial squeezed states, bent prolates, squeezed stomatocytes, and cubic and clam-like morphologies. Stability diagrams, bending-energy curves, and phase diagrams are constructed for each confinement, revealing both discontinuous (first-order) and continuous (second-order) shape transitions, as well as hysteresis and metastable branches. These results extend existing confinement studies by providing fully three-dimensional, non-axisymmetric solutions across multiple geometries and different regimes of confinement (free space to weak to strong) within a unified computational framework.

Overall, this work establishes a versatile and scalable neural-network-based phase-field

approach for vesicle shape modeling. By unifying classical membrane elasticity theory with modern machine-learning optimization, the solver facilitates a structured exploration of equilibrium morphologies, phase transitions, and confinement effects beyond the reach of traditional axisymmetric or surface-discretization methods. The framework provides a foundation for future extensions to more complex membrane models, dynamic processes, and biologically relevant geometries in soft-matter and biophysical systems.

Acknowledgements

I would like to express my sincere gratitude to my supervisor, Prof. Jeff Chen, whose guidance and support made the research presented in this thesis possible. I am also grateful to my advisory committee members for their generosity with their time and for their thoughtful feedback in assessing my progress throughout the PhD program. I gratefully acknowledge the funding provided by the Natural Sciences and Engineering Research Council of Canada, which made the pursuit of a PhD in Physics financially feasible.

Finally, I would like to thank my family, friends, and officemates for their kindness, encouragement, and support throughout this long journey.

Table of Contents

Examining Committee ii

Author's Declaration iii

Statement of Contributions iv

Abstract v

Acknowledgements vii

List of Figures xii

1 Introduction 1

1.1 Background and Motivation 1

1.2 Scope and Achievements 7

1.3 Outline of Thesis 11

2 Helfrich Model and Phase-Field Formalism 13

2.1 Helfrich Model 14

2.1.1 Bending Energy Expression 14

2.1.2 Examples for Bending Energy of Elementary Shapes 15
2.2 A Review of Theory and Experiment 16
2.2.1 Curvature-dependent Bending Energy of Biomembranes 16
2.2.2 Experimental Studies 21
2.3 Numerical Calculation of Helfrich's Bending Energy 27
2.4 Application of Machine Learning to Vesicles 32
2.5 Phase Field Model 36
2.5.1 Phase-field Approach to Helfirch Model 36
2.5.2 Phase-field Approach to Area Difference Modeling 43

3 Artificial Neural Networks for Phase Fields **46**
3.1 Artificial Neural Networks 46
3.1.1 Feedforward Neural Networks with an Example 48
3.1.2 Cost Function of an NN 50
3.1.3 Improvements to Learning 52
3.1.4 Stochastic Gradient Descent 54
3.1.5 Backpropagation Algorithm 56
3.2 Neural Network for Vesicle Shapes 58
3.2.1 NN Representation of a Scalar Phase Field 58
3.2.2 Cost Function for Phase Field NN 60

4 Neural Network Solver for 3D Membranes **62**
4.1 Introduction 62
4.2 Model 64
4.2.1 NN Representation of Phase-field 65

4.2.2 Selection of the Number of Parameters and Hidden Layers 66
4.2.3 Numerical Minimization of the Cost Function 66
4.3 Results 67
4.3.1 Convergence Criteria 68
4.3.2 Initial Θ for Axisymmetric Shapes 69
4.3.3 Axisymmetric Shapes in Free Space 74
4.3.4 Non-axisymmetric Shapes in Free Space 75
4.3.5 Vesicles in Hard-wall Confinements 79
4.4 Conclusions 83

5 Vesicles in Confinements **85**
5.1 Introduction 85
5.2 Modeling Methods 89
5.3 Results 91
5.3.1 Cylindrical or Tube Confinement 92
5.3.2 Slit Confinement 97
5.3.3 Spherical Confinement 103
5.3.4 Cubic Confinement 113
5.4 Discussion 117

6 Discussion and Conclusion **121**
6.1 Summary of Contributions 121
6.2 Interpretation of Key Findings 123
6.2.1 Biaxial and bent intermediates under confinement 123
6.2.2 Area difference and division-prone morphologies 124

6.2.3 Energetic trends and phase boundaries 124
6.3 Relation to Prior Work 124
6.4 Methodological Considerations 126
6.4.1 Initialization, continuation, and hysteresis 126
6.4.2 Resolution, interface width, and accuracy 126
6.4.3 Scalability and portability 127
6.5 Limitations and Future Work 127
6.6 Concluding Remarks 128

References **130**

APPENDICES **149**

A Phase-field Formulation of Helfrich Model **150**

B Phase-field Formulation of Mean Curvature **153**

List of Figures

1.1 Schematics of lipid molecules, bilayer, micelle and vesicle 2

1.2 Examples of axisymmetric and non-axisymmetric shapes of vesicles 8

1.3 Examples of shapes of vesicles inside hard-wall confinements 10

2.1 Spherical and cylindrical shells' bending energy 16

2.2 Bending energy vs. reduced volume for axisymmetric shapes from Seifert et al. 28

2.3 Cross-sectional schematic of a spherical vesicle modeled by phase field . . . 37

2.4 Bending energy vs. reduced volume for axisymmetric shapes by Campelo et al. 42

2.5 Area difference schematic for a vesicle with a spherical bilayer 44

3.1 Schematic of a typical feedforward neural network 49

3.2 Phase-field FNN 59

4.1 Neural-network representation of the phase field $\phi(\mathbf{r})$ 65

4.2 Cost function J and bending energy E_b as functions of calculation steps (epochs) 69

4.3 Spherical initial guess for prolates 70

4.4 Initial guess for prolate $\bar{u} = 0.8$ 71

4.5 Initial guess for prolate $\bar{u} = 0.7$ 72
4.6 Initial guess for oblate $\bar{u} = 0.55$ 73
4.7 Initial guess for stomatocyte $\bar{u} = 0.55$ 73
4.8 Examples of axisymmetric shapes and their reduced bending energy vs. reduced volume diagram 74
4.9 Examples of non-axisymmetric shapes: elongated oblate and starfish 76
4.10 Initial guess for an elongated oblate shape $\bar{u} = 0.60$, $\Delta a = 1.10$ 77
4.11 Initial guess for a starfish $\bar{u} = 0.50$, $\Delta a = 1.50$ 78
4.12 Cylindrical, slit, and spherical hard-wall confinements with their characterizing dimensions 79
4.13 Reduced bending energy vs. reduced confinement dimension diagram for cylindrical confinement 80
4.14 Reduced bending energy vs. reduced confinement dimension diagram for slit confinement 81
4.15 Reduced bending energy vs. reduced confinement dimension diagram for spherical confinement 83

5.1 Cubic confinement with its characterizing dimension 91
5.2 Stability diagrams of vesicles in a cylindrical (tube) confinement 93
5.3 Bending energies of vesicles in a cylindrical (tube) confinement for various $\bar{u}$ 95
5.4 Phase diagram of vesicles in a cylindrical (tube) confinement 97
5.5 Stability diagrams of vesicles in a slit confinement 99
5.6 Bending energies of vesicles in a slit confinement for various $\bar{u}$ 101
5.7 Phase diagram of vesicles in a slit confinement 102
5.8 Stability diagrams of vesicles in a spherical confinement 105
5.9 Bending energies of vesicles in a spherical confinement for various $\bar{u}$ 107

5.10 Locally stable shapes at $\bar{u} = 0.60$ and $\bar{u} = 0.65$ 108
5.11 Phase diagram of vesicles in a spherical confinement 110
5.12 Bending energies of vesicles in a spherical confinement for a given area difference and various $\bar{u}$ 112
5.13 Bending energies of vesicles in a cubic confinement for various $\bar{u}$ 115

Chapter 1

Introduction

In this chapter, we lay out the main objective of this thesis: introducing an artificial-neural-network-based solver for vesicle shapes in three-dimensional (3D) space, along with the motivation behind it. We include some background material on lipid bilayers and phospholipid membrane formation. Furthermore, we elaborate on the relevance and significance of designing a novel solver for calculating 3D shapes of vesicles in different physical settings, with regard to its pertinence to the existing literature. Lastly, we briefly discuss the outline of the thesis.

1.1 Background and Motivation

Natural vesicles have a variety of functions both inside cells and in the extracellular environment, e.g., protein and enzyme transport, buoyancy control, and serving as vessels for chemical reactions [1, 2, 3, 4, 5]. In addition to these natural functions, with the advent of modern medical technology, vesicles have become prominent for performing engineered functions inside the human body [6]. For instance, unilamellar and multilamellar liposomes (synthesized spherical vesicles) and cell-derived (extracellular vesicles) have become prominent in modern medicine as vehicles for targeted drug delivery, gene therapy, and regenerative treatments [7, 8, 9, 10, 11, 12]. In particular, in the field of immunology against

infectious diseases, liposome-based and lipid-nanoparticle platforms have become central to modern vaccine design, allowing antigen and mRNA delivery with high efficiency, stability, and immunogenicity [13, 14, 15, 16, 17].

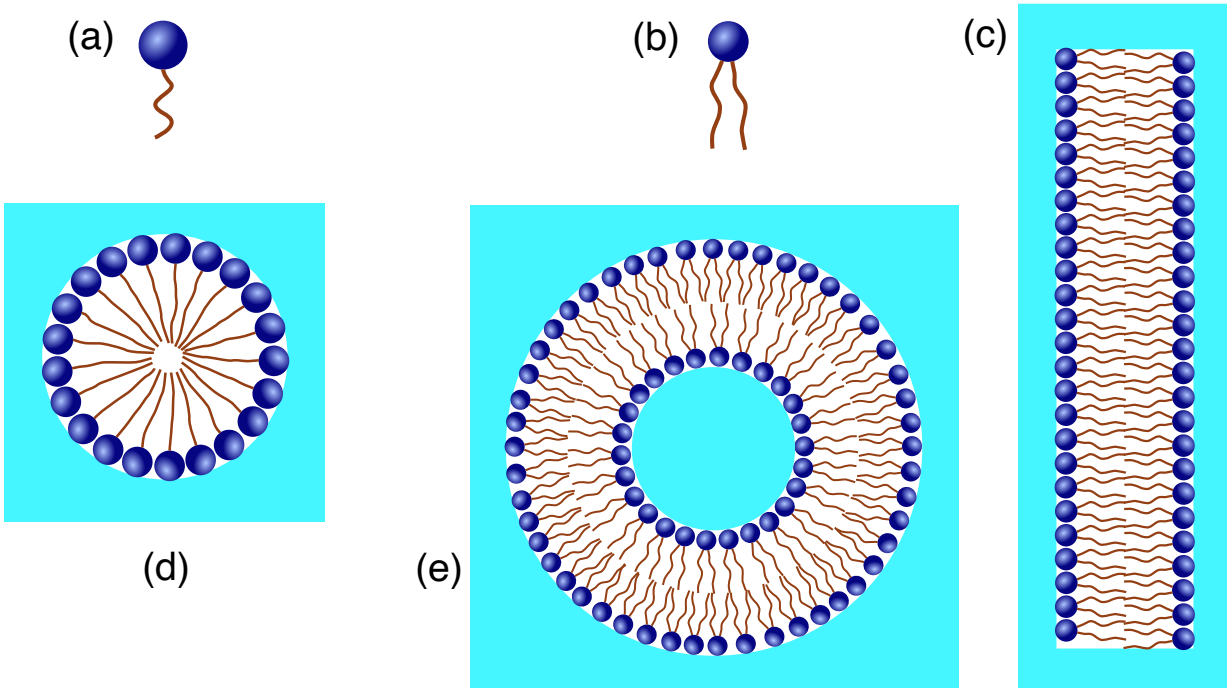


Figure 1.1: Schematics of (a) single-chain amphiphile, (b) double-chain amphiphile, (c) lipid bilayer, (d) micelle, and (e) vesicle formed by lipid bilayer (unilamellar liposome in this case). The light blue areas in (c), (d), and (e) indicate the aqueous phase (e.g., water) made of polar molecules and the structures are shown by their 2D cross sections. The dark blue spheres are the headgroup of the lipid molecules, which are polar and hydrophilic. The brown tails (hydrocarbon chains) are non-polar and hydrophobic.

The main building blocks of vesicles are lipid molecules (Fig. 1.1 (a) and (b)), which form a membranous structure called a lipid bilayer (Fig. 1.1 (c)), separating the exterior space from the interior one [18, 19]. The formation of lipid bilayers in an aqueous phase is favored by the constituent lipid molecules, e.g., amphiphilic phospholipids, when the loss in overall entropy due to aggregation is compensated by the lowered interaction energy between the hydrophobic tails of these molecules and the polar molecules of the aqueous

phase [20].

Additionally, the emergence of a flat bilayer configuration, as opposed to micelles (Fig. 1.1 (d)), is mainly governed by the shape and overall geometry of the lipid molecules. Double-chain phospholipids with comparable cross-sectional areas between the tails and headgroup are more amenable to a flat bilayer structure. Adopting a closed configuration, i.e., a vesicle (Fig. 1.1 (e)), further minimizes the interaction energy of hydrophobic tails by eliminating their exposure at the edges of the bilayer [20].

Based on the type of constituent lipid molecules and other bilayer-embedded molecules such as cholesterol and membrane proteins, the lipid bilayer possesses an inherent bending resistance and, as such, has associated stored energy when in its closed configuration [20]. Naturally, under neutral physical conditions, vesicles attain a specific shape in 3D space that favors a minimum value of this stored energy. Depending on the conditions that determine the physical properties of the phospholipid membrane (lipid bilayer), namely, whether it comprises a finite number of molecules and/or whether it is impermeable to the exterior of the vesicle, the surface area and the volume of vesicles remain unchanged. As such, these factors can restrict the magnitude of the bending energy of the membrane [21, 22, 23, 24, 25].

The attempts at theoretical modeling of the deformable membrane of a vesicle as a 2D fluid [26] culminated in the Helfrich equation for the bending energy in 1973 [27]. This equation relates the bending energy of a surface area element ($\mathrm{d}S$) of the membrane to its principal curvatures, or more precisely, to its mean (H) and Gaussian (K) curvatures; it can be written as a surface integral over H and K for the entire membrane, namely $E_b \propto \int_S H^2 \mathrm{d}S + \int_S K \mathrm{d}S$. [28, 29]. The constraints on the surface area A and volume V of a closed interface made of these surface area elements (i.e., the vesicle) are introduced by including the appropriate Lagrange multipliers. Finding the 3D shape of the vesicle using this formulation of the bending energy and constraints is equivalent to solving a variational problem for the bending energy, namely $\delta(E_b + \Sigma A + PV) = 0$ with δ denoting variation and Σ and P being the Lagrange multipliers for surface area and volume, respectively [30, 31, 32].

Among the numerical methods developed for solving this variational problem are: a

shooting method to resolve the 2D contour of axisymmetric shapes, where a Lagrangian approach is used to formulate the governing variational equation [31, 32]; triangulation methods that incorporate finite element analysis for calculating the equilibrium shape of both axisymmetric and non-axisymmetric shapes in 3D [33, 34, 35, 36, 37] (e.g., Surface Evolver package [38]); a Ritz method based on expansion in terms of spherical harmonics that can approximate non-axisymmetric shapes as well [39, 40]; a method of shape parameterization that is achieved by solving an elliptic partial differential equation for generating 3D axisymmetric and non-axisymmetric shapes [41]; level-set methods [42, 43, 44]; and conventional finite difference schemes that discretize field-based approaches such as the phase-field model [45, 46, 47, 48, 49].

These numerical approaches differ primarily in how the vesicle shape is represented, how curvature is computed, and how the variational problem is solved. In shooting methods, the membrane is reduced to a one-dimensional contour in the two-dimensional space by assuming axial symmetry, and the Helfrich bending energy is expressed in terms of arc-length–parameterized geometric variables. The resulting Euler–Lagrange equations form a boundary-value problem for a system of coupled ordinary differential equations, which can be solved by shooting or relaxation techniques [31, 32]. While this approach provides high accuracy for axisymmetric shapes, it cannot capture symmetry-breaking instabilities or intrinsically three-dimensional morphologies, as the reduction to a two-dimensional contour is imposed *a priori*.

Triangulation- and finite-element–based methods instead discretize the membrane as a two-dimensional surface embedded in three-dimensional space [33, 34, 35, 36, 37]. In these approaches, curvature quantities are evaluated either directly on the mesh or via weak formulations that lower the order of derivatives [50]. This enables the computation of fully three-dimensional, non-axisymmetric equilibrium shapes and allows for topological changes in principle. However, explicit surface tracking introduces challenges related to mesh quality, including element distortion and entanglement, which often necessitate remeshing and complicate convergence near regions of high curvature, such as necks or budding sites [50, 51]. Packages such as Surface Evolver [38] mitigate some of these issues, but at the cost of increased algorithmic complexity and sensitivity to discretization choices.

Alternative shape-representation strategies avoid explicit surface meshes by expanding

the membrane geometry in a predefined basis or by introducing implicit surface descriptions. In the Ritz method, the vesicle shape is parameterized by a truncated expansion in spherical harmonics, and the Helfrich energy is minimized with respect to the expansion coefficients [39, 40]. This approach naturally accommodates non-axisymmetric perturbations around nearly spherical shapes and is computationally efficient for modest deformations; however, its accuracy deteriorates for strongly deformed morphologies and is limited by the chosen truncation order. Relevant to this, elliptic-PDE–based parameterization methods generate vesicle surfaces by solving auxiliary elliptic equations whose solutions define smooth surfaces (the membrane) in three dimensions [41]. These methods provide geometric flexibility but still require careful numerical treatment of curvature and constraints.

The level-set method takes a fundamentally different approach by representing the vesicle implicitly as a sharp interface of a scalar field defined on a fixed grid. This method is closely related to the phase field method where the interfuse is more diffuse. In other words, the level-set method is the sharp interface limit of the phase field method. Curvature and geometric quantities are computed directly from this field, eliminating explicit surface tracking and naturally handling topological changes. Conventional implementations evolve the scalar field dynamically via gradient-flow equations discretized by finite differences or finite elements [42, 43, 44]. While robust, such PDE-based formalisms can be sensitive to time-stepping stability, and discretization errors in high-order derivatives.

The results presented in this thesis are based on the phase-field formulation of the Helfrich model [45, 52, 46, 48, 47, 49]. The phase-field approach assigns scalar values to spatial points of a prescribed domain that contains the vesicle. The advantages of this approach include its simplicity for numerical implementation, where a finite rectangular grid can be readily introduced for calculating various quantities as functions of the underlying phase field. It requires no remeshing schemes or other advanced numerical techniques, as the interface (membrane) is located on the transition layer, with a given length scale, between the highest and lowest values of the field. Moreover, it is applicable to both axisymmetric and non-axisymmetric shapes [47, 49].

The phase-field approach has been implemented numerically using spatial finite differences, the implicit Euler method for temporal integration, and/or Fourier spectral method [45, 52, 47, 48, 49]. However, a numerical framework that eliminates the need for finite dif-

ference schemes, while being flexible and versatile enough to adapt to a variety of simulation scenarios, could accelerate progress in this area. Specifically, developing an independent and adaptable solver that requires minimal modification for simulating various physical conditions a vesicle might encounter—such as confinement, translocation, and others—is crucial. This will significantly enhance our understanding of vesicle shape transformations, phase transitions, and the overall energy landscape of vesicle shapes.

The primary objective of this thesis is to develop and implement a solver that operates within the phase-field formalism. In essence, it "learns" the underlying physical model of membranes by being "trained" on the phase-field formulation of the model. It is important to emphasize that no axial symmetry is imposed when obtaining the shapes generated by the solver; instead, the symmetry (or lack thereof) emerges naturally through the process of energy minimization (training).

The core of the novel solver presented here is an artificial neural network (NN) [53, 54]. These networks are modeled after their biological counterparts, where nodes (neurons) are connected via nonlinear functions with weighted inputs (activation signals) [55, 56]. The weights and type of nonlinearity determine the NN's output for a given set of inputs. These properties enable the NN to represent the solution, which in this case is the phase-field function (NNs are universal approximators of continuous functions [57, 58, 59]). In other words, the NN represents the 3D shape of the solution to the problem of finding the minimum Helfrich bending energy subject to geometric constraints. The shape representation can be easily embedded in different simulation scenarios or interact with other NNs representing other shapes, without the need to recalculate the shape for each numerical computation. This framework retains the advantages of an implicit surface description while replacing the explicit variational treatment of the Helfrich bending energy with a direct parametric minimization, using precise analytical differentiation of curvature terms and flexible incorporation of global constraints without remeshing or time integration.

In addition to the fact that NNs are universal approximators, there are robust machine learning techniques and optimization algorithms for training (or optimizing) them [60, 61, 62]. These, along with other aspects such as new network designs, remain an active area of research [63, 64, 65, 66, 67, 68]. The fundamentals of NN structure and training will be elaborated on in a subsequent chapter.

1.2 Scope and Achievements

The physics-based modeling and numerical calculation of vesicle shapes has a fifty-year history in the literature [69, 27, 70]. The study of the Helfrich model for the elastic bending energy using a scalar field—inspired by the Ginzburg–Landau energy functional—is more recent, dating back to the early 1990s [71]. Both axisymmetric and non-axisymmetric shapes have been explored, with examples including oblate shapes (e.g., red blood cells, also known as erythrocytes), prolate shapes (also known as dumbbell or cigar-shaped vesicles), stomatocytes (spherical shapes with a mouth), and starfish and racket-shaped vesicles (see Fig. 1.2 for examples of these shapes). In the case of phase-field-modeled vesicles, calculating a complete phase diagram that exhibits good agreement with the literature, e.g., Seifert et al. [31] for axisymmetric shapes, has been largely neglected. To our knowledge, there are only two papers by Campelo et al. [48] and Banham et al. [49], which use phase-field modeling to reproduce parts of the phase diagram for axisymmetric shapes. Our NN-based solver is able to reproduce a diagram with as many data points as required for reconstructing a more complete picture. Therefore, our numerical approach addresses the scarcity of phase diagrams in the context of the phase-field approach.

For non-axisymmetric shapes studied and numerically calculated using the phase field model, a direct reformulation of the area difference model [72, 73, 31] is lacking in the literature. It accounts for the difference between the internal and external surface areas of the lipid bilayer and can be approximated by $\Delta A \approx 2s \int_S H \mathrm{d}S$ where s is the distance between the monolayers and H is the local mean curvature [31]. The variational treatment then requires finding shape solutions to $\delta(E_b + \Sigma A + PV + Q\Delta A) = 0$, where Q is an additional Lagrange multiplier that enforces the constraint on the area difference ΔA; this variational problem is converted into a cost minimization procedure in our NN solver framework where the area difference is included as a constraint. We have derived a phase field equivalent of the area difference model and have obtained non-axisymmetric shapes such as the so-called starfish [35, 74, 75]. The details for the derivation of the phase-field area difference are provided towards the end of the next chapter.

The placement of vesicles inside a confinement imposes a different type of external potential on a vesicle. The literature on this topic is largely focused on symmetric con-

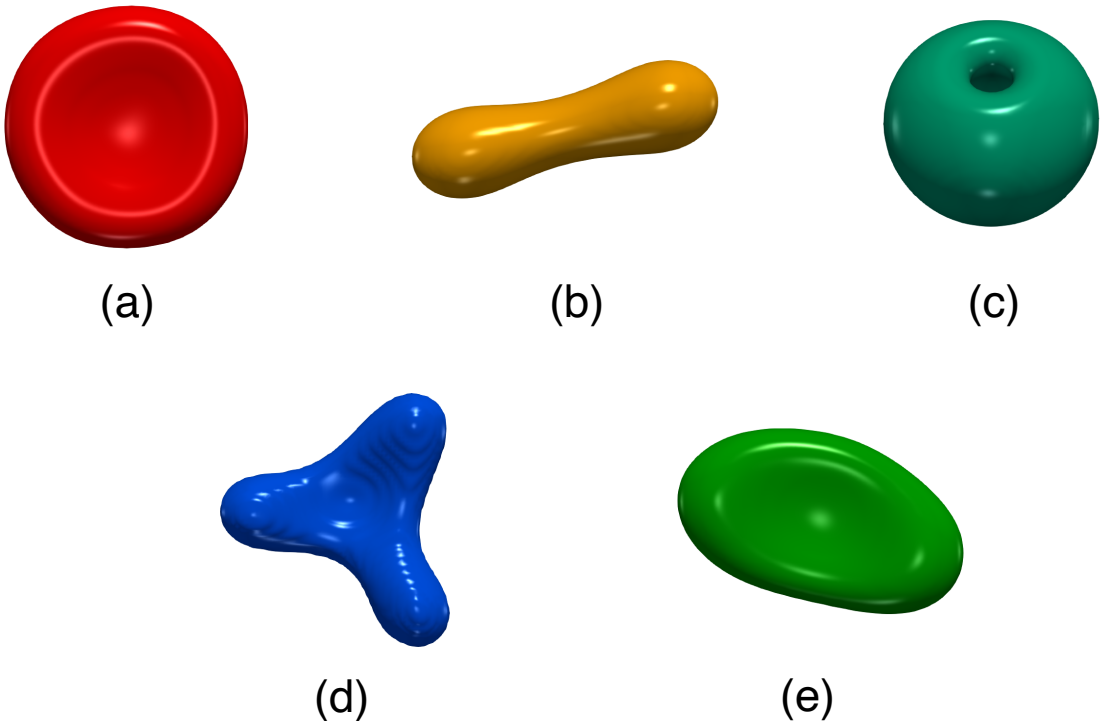


Figure 1.2: Axisymmetric and non-axisymmetric shape examples: (a) oblate, (b) prolate, (c) stomatocyte, (d) starfish, and (e) racket-like shape.

finements [36, 76, 37, 77, 78]. Under these conditions, the axial symmetry of the adopted equilibrium shape can be broken. To simulate these effects, the confinement size is reduced such that the confinement walls come into contact with the membrane, i.e., the phase field interface. In the numerical framework established here, this can be accomplished by introducing a mathematically formulated hard-wall constraint using familiar 3D equations that describe elementary shapes. We have produced results for spherical, cylindrical, and slit hard-wall confinements; however, it should be mentioned that simulations using a variety of confinement shapes are readily possible in our framework. Moreover, the strong confinement limit, which has a body of work devoted to it [36, 37, 77], is another avenue that can be examined by the proposed NN solver. In this thesis, the confinement is referred to as strong when the characteristic size of the confining geometry becomes comparable to

or smaller than the smallest intrinsic length scale of the vesicle, such that the membrane is forced into sustained contact with the confining walls and its equilibrium shape is no longer determined primarily by free-space bending energy minimization. Here, the characteristic confinement size may be defined by the minimal width, radius, or edge length of the confining geometry, while the intrinsic vesicle length scale is set by the equivalent spherical radius R_0.

In addition to confirming the main axisymmetric families of shapes under confinement, our numerical study revealed a variety of non-axisymmetric morphologies and shape transformations. For example, in cylindrical confinements, oblates lose their axial symmetry under compression and evolve into biaxial shapes, and stomatocytes are squeezed and elongated before transforming into prolates at stability limits. In slit confinements, prolates deform into squeezed biaxial configurations, while oblates develop flattened profiles, some of which exhibit divergent behavior at critical confinement sizes. Spherical confinement gives rise to both bent and confined cup-like shapes [36, 37], with regions of unstable morphologies marked by large fluctuations in bending energies. Finally, cubic confinement produces a distinct class of cuboidal and quadriconcave shapes that resemble experimentally observed Knizocytes [34], highlighting the solver's ability to capture shape classes with reduced symmetry and complex morphology (see Fig. 1.3 for illustrations of the aforementioned shapes).

The confinement studies not only reproduce several known results in the literature [36, 76, 79, 80, 77], but also extend them by identifying the energetic landscape and classifying the nature of phase transitions—whether first-order, second-order, or continuous. The neural-network framework thus provides a unified setting where stability diagrams, energy diagrams, and phase diagrams can be constructed for a wide variety of confinement geometries. This capability demonstrates that our solver is versatile enough to accommodate external potentials of different symmetries and strengths, while maintaining high accuracy in capturing transitions between competing morphological states.

The shape transformation process can also occur during the translocation of a vesicle through an opening in a barrier [81, 82, 83, 84, 85, 86, 87]. Axial symmetry can be broken during this process, particularly when the vesicle is passing through the barrier's opening. Our solver can easily simulate translocation, and we consider this direction of research a

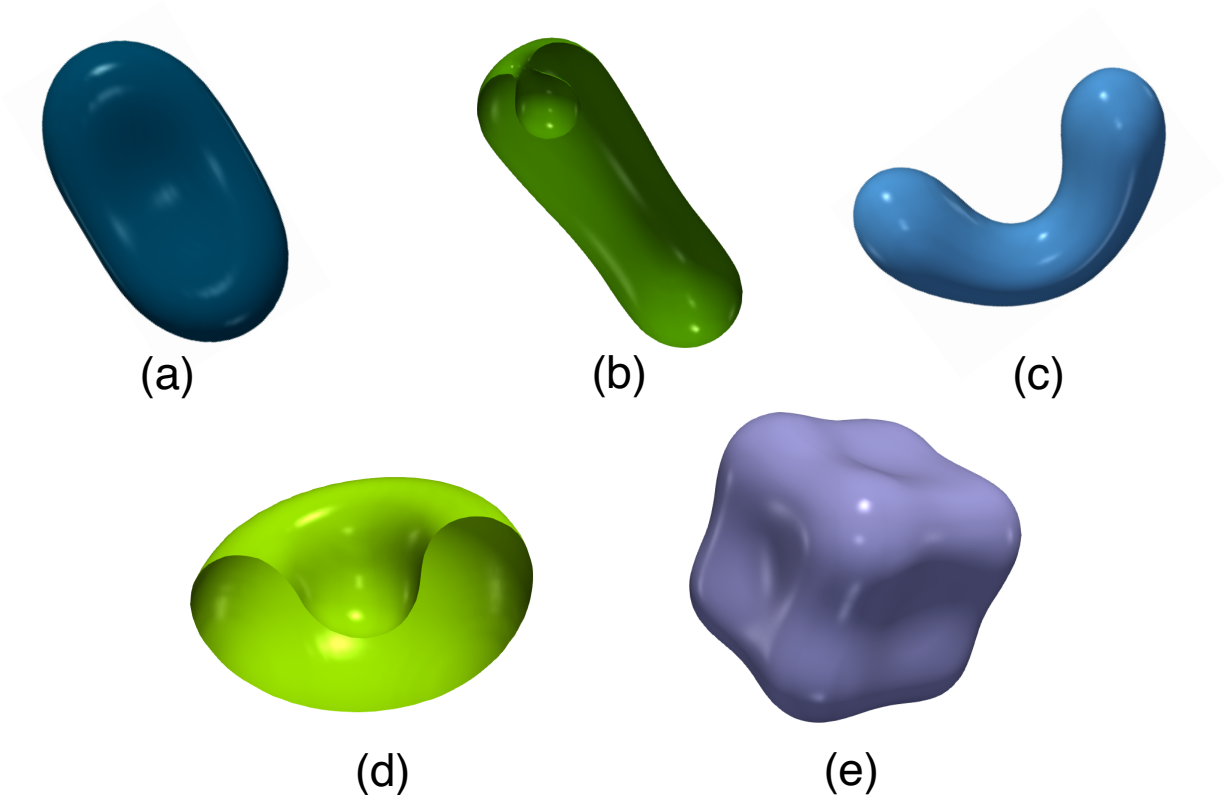


Figure 1.3: Shape examples obtained as a result of confinement: (a) biaxial, (b) elongated stomatocyte, (c) bent prolate, (d) cup-like, and (e) cuboidal and quadriconcave. (b) and (d) shapes are cut into halves to reveal their interior and provide a better overall view.

viable approach for studying the physics and energy landscape of the process. This will be investigated in future work. It should be noted that our solver has the flexibility to calculate shape displacements through openings of different sizes and geometries. Furthermore, this can be implemented for both axisymmetric and non-axisymmetric vesicles.

In summary, our solver has the capability to resolve the 3D shape of both axisymmetric and non-axisymmetric structures without imposing axial symmetry as a separate requirement. It can be readily adapted to different simulation scenarios by introducing various types of constraints to the solver's cost function.

1.3 Outline of Thesis

In the next chapter, we introduce the Helfrich theory for the lipid bilayer bending energy, and then we provide a comprehensive review of the literature on theoretical, experimental, and numerical/computational phospholipid-vesicle research. We then introduce the phase-field formulation of the Helfrich theory for bending energy. The derivations of the bending energy, surface area, and volume in this framework are discussed with details provided in the Appendices. The area-difference model and its phase-field equivalent are also discussed here, along with their physical implications for modeling non-axisymmetric vesicle conformations.

Chapter 3 expounds on the specifics of artificial neural networks and the algorithms involved in training them, particularly in the context of the mathematical modeling discussed in this work. The backpropagation algorithm, computational graph construction in PyTorch, and the implementation of cost-function gradients are described in detail. The architecture of the NN for representing the vesicle phase field is introduced here, together with its numerical advantages and limitations.

Chapter 4 presents the deployment of the NN solver for the phase-field-formulated Helfrich model. Both axisymmetric and non-axisymmetric vesicle shapes are computed and illustrated. The chapter also provides implementation details of the cost function and training process, including the use of the Adam optimization algorithm. Bending energy vs. reduced volume diagram is reproduced and compared with the literature, showing excellent agreement, and demonstrating the solver's capacity to capture known shape transitions as well as produce novel non-axisymmetric conformations.

Chapter 5 is dedicated to confinement studies of vesicles. We expand the investigation of vesicle shapes confined in different types of hard-wall confinements by including a larger range of reduced volumes and various initial shapes. In addition to spherical, cylindrical, and slit confinements, we introduce cubic confinement as a new case. Bending energy diagrams, stability diagrams, and phase diagrams are constructed for each confinement, and the solver's ability to handle both axisymmetric and non-axisymmetric transitions is highlighted. We also provide a preliminary study of the bilayer area-difference constraint in spherical confinement, which reveals rich morphological transitions such as clam-like

shapes and division into disjoint vesicles.

Finally, in the Discussion and Conclusion chapter, we lay out the possibilities that the vesicle-shape NN solver has opened for numerical calculations and, most importantly, simulations that can inform the physics of vesicles, especially phospholipid vesicles. The accomplishments of this work are summarized, including its contributions beyond existing methods such as finite element and triangulation approaches. We also outline areas for improvement, such as extending the solver to more advanced NN architectures, incorporating flow effects, and adopting the area-difference-elasticity model. We close with a discussion of future research directions and a brief recap of the central contributions.

Chapter 2

Helfrich Model and Phase-Field Formalism

In this chapter, we first introduce the mathematical formalism of the Helfrich model for the bending energy of deformable membranes. Then we continue by reviewing both the theoretical and experimental research that contributed to the development and consolidation of the Helfrich framework. Due to its nonlinear nature and mathematical complexity, various computational methods have been proposed over the past four decades for solving the model numerically; we provide an in-depth overview of these approaches. In addition, we briefly survey recent applications of machine learning to the study of lipid bilayers and vesicles.

We then show how the geometric formulation of the Helfrich model can be recast in a field-based framework. Specifically, we demonstrate how a phase field can be used to reformulate the Helfrich energy. To this end, we introduce two distinct approaches to phase-field reformulation, with mathematical details presented in Appendices A and B. Finally, we present a phase-field-based expression for the area difference between the two monolayers of the lipid bilayer. This quantity can be incorporated as an additional constraint into the Helfrich model, enabling the generation of asymmetric (zero spontaneous curvature) and non-axisymmetric vesicle shapes in free space.

2.1 Helfrich Model

Lipid bilayers exhibit resistance to deformation as a result of interactions that the constituent amphiphiles can experience from stretching and compression. These include steric interactions that oppose compression and surface tension of water and amphiphiles that oppose stretch [20]. The bending of a bilayer causes one leaflet to stretch and the other to compress, resulting in stored bending energy within the bilayer. Naturally, the bilayer adopts a conformation that minimizes this energy at equilibrium, subject to any internal as well as external constraints.

2.1.1 Bending Energy Expression

The bending energy stored in an element of the surface area of the bilayer is related to its curvature, i.e., the higher the curvature, the higher the energy. The density of this energy (bending energy per unit surface area) has the following form, where H and K are the mean and Gaussian curvatures [69, 27, 70]:

$$e_b = 2\kappa(H - H_0)^2 + \kappa_G K, \tag{2.1}$$

where κ and κ_G are bending modulus and Gaussian modulus, respectively, and have units of energy. Typical values of κ obtained by numerous experiments are on the order of 10^{-19}J or $5 - 30\ k_B T$, where k_B is the Boltzmann constant and T is the temperature ($20 - 30$ °C) [20, 88]. Typical experimental values reported for κ_G are negative [20, 89].

Here, $H = (C_1 + C_2)/2$ and $K = C_1 C_2$, where C_1 and C_2 are the local principal curvatures. In general, the curvature of a surface depends on the direction along which the curvature is determined. The minimum and maximum curvatures of a particular surface (or its local values for an area element) are called the principal curvatures. These can be calculated using differential geometric relations for the directional curvature of a surface in 3D and finding the extremum values [20, 28, 29].

We also notice that the first term (contribution of mean curvature) on the right-hand side of (2.1) includes H_0. This is known as spontaneous curvature and is a constant,

introduced phenomenologically to account for the curvature that some bilayers exhibit even in their equilibrium state [20]. This intrinsic curvature can arise due to asymmetries in the composition of the two leaflets (monolayers) of a bilayer [90] or from other effects, such as the asymmetric distribution of electric charges [91].

The bending energy of a surface element, $\mathrm{d}S$, can be calculated by (2.1) as $E_b = e_b \times \mathrm{d}S$. For a closed surface, i.e., the deformable membrane (phospholipid bilayer) of a vesicle, this energy is obtained by performing a surface integral over the whole surface:

$$E_b = 2\kappa \int_S (H - H_0)^2 \, \mathrm{d}S + \kappa_G \int_S K \mathrm{d}S. \tag{2.2}$$

We should note an important property with respect to the second term in (2.2), namely the contribution from the Gaussian curvature K. For vesicle shapes that are topologically similar, this term remains unchanged. This in turn is related to the Gauss-Bonnet theorem, which states that for a spherical surface with an Euler characteristic $\chi = 2$, the surface integral of K remains invariant and equal to $2\pi\chi = 4\pi$ as long as it is bent and deformed without topological transformation to a different shape (e.g., a torus) [92]. As such, since all the shapes presented throughout this thesis have this property, we omit the Gaussian term from the Helfrich bending energy in our numerical calculations.

2.1.2 Examples for Bending Energy of Elementary Shapes

Here, we calculate the bending energy of elementary shapes, using (2.2). For this, we consider the schematics in Fig. 2.1 where a spherical shell with radius R_s and a cylindrical shell with radius R_c and length L are illustrated. The principal curvatures for the spherical shell are constants and the same everywhere on the shell, namely $C_1 = C_2 = 1/R_s$. Hence, the mean and Gaussian curvatures for the spherical shell are $H = 1/R_s$ and $K = 1/R_s^2$, respectively. By carrying out the surface integral in (2.2) and setting the spontaneous curvature $H_0 = 0$, we obtain the bending energy of a spherical shell as $E_b = 4\pi(2\kappa + \kappa_G)$.

For a cylindrical shell, the principal curvatures are $C_1 = 1/R_c$ and $C_2 = 0$, since the radius of curvature is infinite along the length of the cylinder. Therefore, the mean curvature is $H = 1/(2R_c)$ and the Gaussian curvature is zero. Using (2.2) and setting

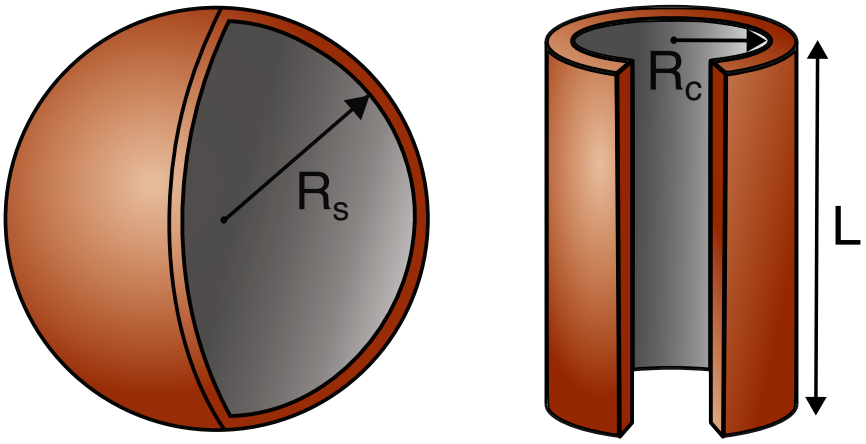


Figure 2.1: Schematics of a spherical shell with radius R_s and a cylindrical shell with radius R_c and length L. The bending energy for these shapes can be calculated by substituting the principal curvatures of each shape in (2.2).

$H_0 = 0$, the surface integral of the squared mean curvature is easily evaluated, yielding a bending energy of $E_b = \kappa\pi L/R_c$.

2.2 A Review of Theory and Experiment

Both experimental and theoretical efforts have been made to understand the processes that determine the morphology of phospholipid vesicles and the underlying physical principles governing their formation and shape transformations. In this section, we review these foundational studies, which culminated in the formulation of the Helfrich model for vesicle shape and the associated bending energy [27].

2.2.1 Curvature-dependent Bending Energy of Biomembranes

The biconcave morphology of human erythrocytes (red blood cells) has been a long-standing subject of inquiry, prompting numerous hypotheses regarding the underlying biophysical mechanisms. In his influential 1970 paper, Canham addressed this problem by introducing a theoretical framework based on the minimization of bending energy [69].

Previous theories frequently invoked factors such as internal pressures, regional membrane specialization, or tensional forces to explain the shape of erythrocytes. However, Canham's hypothesis significantly simplified the problem by attributing the morphology of erythrocytes exclusively to the mechanical properties inherent in the membrane. He posited that the erythrocyte membrane adopts a configuration that minimizes bending energy, aligning closely with concepts from elasticity theory and structural mechanics [93].

In Canham's model, the erythrocyte membrane is treated as a thin elastic shell. The membrane bending energy density is taken as proportional to the sum of the squares of its principal curvatures, assuming homogeneous mechanical properties and a conserved membrane area during osmotic volume changes. Using this formulation, Canham systematically evaluated potential membrane configurations to identify shapes associated with minimal bending energy. For this, a modified version of the classical Cassini ovals equation was used to mathematically generate these theoretical cell profiles. The modified version of the equation in the (x, y)-plane reads

$$y = c[(b^4 + 4a^2x^2)^{\frac{1}{2}} - a^2 - x^2]^{\frac{1}{2}}, \tag{2.3}$$

where c is a dimensionless parameter introduced in this modified version to provide an extra degree of freedom for the tunability of shapes, and a and b are the usual parameters (in units of length) that control the overall shape of the ovals [69]; when b^2, the product of the distances of a point from two fixed points (foci of the Cassini oval $2a$ apart) is kept constant, the locus of these points forms a Cassini oval. Through numerical experimentation, parameters were varied within this equation to produce numerous plausible shapes, each with fixed area and volume; to obtain these three-dimensional shapes, Canham assumed axial symmetry and rotated the 2D profiles around the axis of symmetry. The calculated bending energies of these theoretical profiles were consistent with shapes that closely matched the actual erythrocyte profiles observed under isotonic and hypotonic conditions.

In summary, Canham's analysis provided compelling evidence that the biconcave morphology of erythrocytes (red blood cells) arises fundamentally from the principles of minimizing bending energy.

Following this work on red blood cells, Evans investigated the mechanics underlying

bending resistance and chemically induced moments in membrane bilayers [70]. Evans rigorously addressed the scenario of pure bending in bilayers, emphasizing differences in mechanical properties between the two distinct membrane leaflets. His analysis distinguishes between connected bilayers, where no relative sliding occurs between the leaflets, and unconnected bilayers, where such sliding is permitted. The resistance to curvature in connected bilayers was explicitly formulated, revealing it as a function of local curvature. Evans further clarified that, unlike connected bilayers, the bending resistance of unconnected bilayers is governed by average curvature over the entire membrane surface rather than local curvature. Importantly, Evans also accounted for the structural rigidity provided by the cytoskeletal components of biological membranes, acknowledging that this rigidity must be overcome for significant shape changes. For instance, the expression adopted for calculating the mechanical energy of a deformed combination of lipid bilayer and membrane skeleton (a more accurate description for red blood cells) in modern literature contains both a bending energy term, which is dependent on the mean curvature, and another term dependent on the resistance of the membrane skeleton against shearing and stretching [94, 95].

In general, the work on theoretical modeling of the shape of red blood cells demonstrated that it is linked to the bending energy of the cell membrane, which is driven by the curvature of the membrane. However, as mentioned earlier, another contribution from the membrane skeleton also influences the equilibrium shape of red blood cells. Since the focus in this thesis is mainly on phospholipid vesicles, which are made up of a closed lipid bilayer that may contain other components such as cholesterol molecules and membrane proteins [20], but not a cytoskeletal structure, only the contribution of curvature-induced bending energy is considered to be the main driver of the equilibrium shape (with constraints on the surface area and volume of the vesicle). Before we introduce the original theoretical model that describes the elasticity of the lipid bilayers, a brief account of the underlying structural model of the bilayers is provided. This bilayer model is integral to the theoretical elasticity model.

In their influential 1972 paper, Singer and Nicolson introduced the fluid mosaic model, a groundbreaking conceptual framework describing the structural organization of biological membranes [26]. Prior to this work, existing membrane models typically portrayed

membranes as static structures. Singer and Nicolson's model, however, emphasized the dynamic nature of membranes, proposing them as fluid bilayers of phospholipids within which integral proteins are embedded, creating a mosaic-like arrangement.

The fluid mosaic model draws heavily on thermodynamic principles, arguing that the stable configuration of membranes involves maximizing hydrophobic interactions internally while presenting hydrophilic groups externally to the aqueous environment.

By proposing a dynamic two-dimensional solution of proteins and lipids, Singer and Nicolson transformed the understanding of membrane biology. Their model not only reconciled disparate experimental findings, but also provided a robust theoretical foundation for subsequent research into cellular membranes. Specifically, the two-dimensional fluid bilayer is the starting point for the Helfrich model of the bending energy, as it leads to a vanishing shear modulus [27], eliminating its effect on the equilibrium shape of the phospholipid vesicles.

In his foundational paper, Helfrich developed a comprehensive theoretical framework to describe the elastic properties of lipid bilayers [27]. Helfrich proposed a continuum mechanical model that characterizes lipid membranes through distinct elastic strains, specifically addressing stretching, tilt, and curvature. However, he emphasized that curvature elasticity predominantly determines the shapes of vesicles, particularly in the absence of external constraints or forces. On the basis of this insight, Helfrich derived an expression for the bending energy of the lipid bilayer, using the mean and product of the local principal curvatures.

Helfrich derived explicit Euler-Lagrange equations governing vesicle shapes under external influences such as magnetic fields and pressure differences. He demonstrated theoretically that spherical vesicles could deform into ellipsoidal shapes when subjected to magnetic fields. Additionally, Helfrich predicted that under an external pressure difference, spherical vesicles exhibit instability at a defined threshold, subsequently adopting non-spherical configurations.

A notable insight from Helfrich's analysis is the introduction of the concept of "spontaneous curvature", which accounts for bilayers that inherently prefer a certain curvature due to asymmetries in molecular composition. This parameter critically affects the equilibrium

shapes of the vesicles and the magnitude of their deformation.

Moreover, Helfrich discussed experimental methodologies to validate his theoretical predictions, notably using magnetic fields and controlled osmotic pressures to measure bilayer elasticity experimentally. These approaches laid the groundwork for subsequent experimental validations of membrane elasticity theories.

Helfrich's theory has become fundamental in membrane biophysics, significantly influencing subsequent research on biological membranes, vesicle dynamics, and the mechanics underlying cellular morphology. By presenting clear theoretical foundations alongside practical experimental proposals, Helfrich established a framework that remains pivotal in contemporary studies of soft matter and biophysical membranes.

In another seminal paper, Deuling and Helfrich systematically investigated the Helfrich model for the bending energy due to membrane curvature—assuming negligible membrane stretching and shear—for lipid bilayer membranes, providing a comprehensive catalog of vesicle shapes [96]. Their theoretical approach focused on the elasticity of closed vesicles, such as those composed of lecithin bilayers in aqueous environments, under the assumption of rotational symmetry.

Deuling and Helfrich derived and solved the Euler-Lagrange equations governing vesicle shapes, explicitly accounting for parameters such as vesicle volume, membrane surface area, and spontaneous curvature. They presented an extensive set of solutions, numerically calculating various equilibrium shapes, including oblate and prolate ellipsoids, discocytes, stomatocytes, torocytes, and more complex asymmetric forms. Each of these shapes emerges from different boundary conditions applied to the Helfrich model.

Because vesicles are closed surfaces, no physical boundary conditions are imposed in space; instead, the shape is determined by geometric regularity conditions and symmetry constraints. Under the assumption of axisymmetry, the surface is generated by revolving a planar contour, and smooth closure at the poles requires the radial distance from the symmetry axis to vanish, ensuring a closed, non-singular surface and the curvature to remain finite, which fixes the boundary conditions there. Additional constraints arise from symmetry: imposing reflection symmetry about an equatorial plane yields prolate and oblate shapes, while relaxing this symmetry allows asymmetric solutions such as stomatocytes.

For shapes involving membrane self-contact, internal boundary conditions in the form of curvature jump conditions are introduced to balance normal forces and prevent interpenetration. Thus, different vesicle morphologies emerge from the same variational problem through the selection of admissible boundary conditions and symmetry assumptions.

An essential insight resulting from their work is the significant role that spontaneous curvature plays in determining the shapes of stable vesicles. For instance, their analysis showed critical thresholds for spontaneous curvature that separate stability regions between oblate and prolate configurations. Moreover, they demonstrated that as the vesicle volume changes, transitions between different stable shapes occur, sometimes involving discontinuous morphological transformations.

Their theoretical predictions also explained experimentally observed vesicle morphologies, including those encountered in red blood cells and artificially prepared lipid vesicles. Deuling and Helfrich emphasized the practical applicability of their model by comparing their results with experimental observations, highlighting excellent agreement.

This foundational paper not only cataloged various possible shapes of fluid lipid vesicles but also laid the groundwork for understanding and predicting vesicle morphology based solely on curvature elasticity principles. Their rigorous theoretical framework has since become a cornerstone in the field of soft matter and biophysics, profoundly influencing subsequent research into membrane mechanics and vesicle dynamics.

2.2.2 Experimental Studies

Experimental efforts have been undertaken to characterize biomembrane vesicles, their physical properties, and morphological behaviors using a variety of experimental setups and vesicle preparation methods. These studies have yielded data used to construct phase diagrams, bending energy versus reduced volume plots, and to determine key elastic and structural properties such as the bending modulus and membrane thickness. Moreover, experimental investigations have provided valuable insight into vesicle shape transformations and transitions, both in free space and under confinement.

Among the well-established experimental techniques for probing membrane mechanics

is micropipette aspiration, which is primarily used to measure mechanical properties such as the bending modulus of cell and vesicle membranes. This technique involves applying suction pressure through a micropipette to draw a small segment of the membrane at the tip of the pipette. For example, micropipette aspiration was used to measure the bending modulus of red blood cells [97]. However, as noted earlier, red blood cell membranes include a cytoskeletal network, making their mechanical response distinct from that of phospholipid vesicles, which consist mainly of lipid bilayers without such structural components.

In early work on lipid bilayers, the bending modulus was determined for giant thin-walled vesicles using micropipette aspiration and tethering methods [98]. A seminal study by Evans and Rawicz [99] extended this technique to several types of phospholipid vesicles. They demonstrated that the relative change in the apparent (projected) area of a vesicle—resulting from the suppression of thermal undulations—is linearly related to the bilayer tension in the low-tension regime. This relationship enables the extraction of the bending modulus from experimental data via linear fitting [100].

In another important contribution, Needham and Nunn examined the influence of cholesterol content on the mechanical properties of lipid bilayers, including the area compressibility modulus and membrane lysis tension [101]. Overall, micropipette aspiration remains one of the principal experimental methods for investigating the mechanical properties of lipid membranes [102, 103, 104].

Imaging and microscopy techniques represent another major class of experimental methods used to study phospholipid vesicles. These approaches are primarily employed to investigate vesicle shape transformations, size and morphology distributions, and to construct phase and bending energy diagrams. In this section, we provide a concise review of selected studies that have utilized these techniques to extract data for a range of purposes, including the analysis of shape transitions, the construction of phase diagrams based on various physical parameters, and the experimental validation of theoretical predictions.

Using dark-field light microscopy, Hotani observed liposomes (single or multilayered lipid bilayer vesicles, also known as unilamellar and multilamellar vesicles) composed of equal molar mixtures of dipalmitoylphosphatidylcholine (DPPC) and cholesterol [105]. He found that these vesicles underwent sequential and reproducible transformations driven

predominantly by osmotic pressure gradients (range of sizes between a few and $10\mu m$). Initially adopting a circular biconcave morphology, liposomes consistently transitioned into several geometrically defined intermediate shapes, including elliptical and polygonal forms (triangular, square, and pentagonal). These morphological transitions involved distinctive undulations, vertex formation, and progressive geometric stabilization. Further transformation pathways bifurcated into more complex structures, producing either branched tubular shapes or head-and-tail configurations (see Fig. 2 in [105]). The osmotic pressure was emphasized as a primary driving force behind these morphological transformations, demonstrated experimentally through controlled variations in the ionic strength and solute concentration.

This study highlighted the generality of the findings in both artificial and biological lipid bilayer systems. The results implied that the vesicle morphology could be stabilized by additional structural components, such as membrane-associated proteins. It was explicitly demonstrated that lipid bilayer fluidity and osmotic pressure govern vesicle morphogenesis.

Berndl et al. systematically examined the shape transformations of giant vesicles (diameters $\approx 10\mu m$) composed solely of dimyristoylphosphatidylcholine (DMPC) in pure water, revealing a striking sensitivity of the vesicle morphology to minute asymmetries in the lipid bilayer [106]. Through careful experimental control, they observed shape transformations induced by temperature variations. These observations were made using the phase contrast microscopy technique [107].

Experimentally, three distinct transformation pathways were identified: symmetric-to-asymmetric transitions from dumbbell to pear-shaped vesicles, vesicle budding (expulsion of smaller vesicles), and discocyte-to-stomatocyte transitions. These transformations were accurately replicated by theoretical modeling based on bilayer bending energy, considering two critical assumptions: minimal lipid exchange between bilayer leaflets and a small difference in thermal expansivity between the inner and outer lipid monolayers. The authors demonstrated that even small differences (on the order of 10^{-3}) in thermal expansivity between bilayer monolayers drastically influenced the vesicle shapes. This sensitivity arose from subtle asymmetries, possibly due to residual impurities or minor compositional variations.

By comparing experimental observations with theoretical trajectories derived from the bilayer-coupling (BC) model (this model is based on the area difference between the inner and outer monolayers, which can translate into asymmetries in the shape of the vesicle [73, 31]), Berndl et al. effectively mapped the observed shape on a reduced area difference vs. reduced volume phase diagram (see Fig. 4 in [106]). Contrasting this with Helfrich's spontaneous curvature model, they underscored the descriptive capability of the BC model in more accurately capturing experimental results, particularly in explaining the continuous nature of observed shape transformations.

In another study, Döbereiner et al. systematically analyzed the shapes of fluid-phase phospholipid bilayer vesicles (sizes $\approx 10-20\mu m$), providing an unprecedented quantitative comparison between experimental observations and theoretical predictions based on the area-difference-elasticity (ADE) model [108]; this model besides the Helfrich's bending energy also takes into account the energy contribution from the difference between the measured/calculated area difference of the monolayers and the relaxed (preferred) area difference, which is determined by the difference between the number of lipid molecules in the inner and outer monolayers times the cross section of a lipid molecule. Utilizing phase-contrast microscopy, the authors meticulously recorded real-time thermal fluctuations of vesicle contours, subsequently digitizing and analyzing these shapes to map them onto the theoretical ADE phase diagram (see Fig. 1 in [108]).

The study demonstrated that temperature variations effectively altered the vesicle parameters, causing the vesicles to traverse distinct trajectories within the theoretical phase diagram. Experimental vesicles exhibited shape transformations, including budding, characterized by the formation of smaller vesicles or buds. The authors carefully identified these transitions as mechanical instabilities occurring at theoretically predicted boundaries. They found strong consistency between observed morphological transformations, such as transitions from prolate to pear-shaped vesicles, and theoretical predictions of local shape instabilities. Complexities such as gravitational effects were also addressed, and their influence on vesicle deformation and orientation was quantified. They showed that gravitational forces could significantly influence shape and stability, necessitating careful correction when interpreting experimental results.

Employing confocal fluorescence microscopy, Yanagisawa, Imai, and Taniguchi docu-

mented the dynamic shape changes associated with phase separation, identifying distinctive morphological transformation pathways [109]. They explored the morphological transformations of lipid vesicles undergoing phase separation under differences in osmotic pressure. The authors used giant vesicles composed of dipalmitoylphosphatidylcholine (DPPC), dioleoylphosphatidylcholine (DOPC), and cholesterol, closely mimicking biologically relevant membranes.

Their results revealed that the vesicle morphology exhibited substantial sensitivity to both the osmotic conditions and the stage at which phase separation was induced. The initial spherical vesicles, upon experiencing osmotic stress and subsequent phase separation, exhibited inward or outward budding depending on the available excess area. The authors used a multidomain ADE model to explain these observations.

In their comprehensive study, Sakashita et al. provided a detailed three-dimensional analysis of lipid vesicle shape transformations using advanced fast confocal laser microscopy techniques [80]. Their investigation offered significant methodological advancements for capturing the full spectrum of vesicle morphologies, encompassing both axisymmetric and non-axisymmetric shapes. Using a detailed computational approach, the authors quantitatively determined critical parameters such as reduced volume and reduced area difference, thus characterizing observed shapes that include stomatocytes, discocytes, cigars, necklaces, elliptocytes, and various complex non-axisymmetric shapes (see Fig. 4 in [80]).

An important achievement of this study was the validation of vesicle transformations against theoretical predictions and phase diagrams based on the BC and ADE models. The authors showed that shape transitions occurred through discrete, step-like changes in the reduced area difference, consistent with the ADE framework. Their experiments allowed a detailed examination of transition pathways such as the cigar–racket–discocyte–stomatocyte and necklace–cigar trajectories. In particular, some transformations exhibited bidirectional and hysteresis-like behavior, providing deeper insights into the metastable states and energy landscapes of vesicle morphology. Furthermore, Sakashita et al. rigorously evaluated their experimental shapes using custom-developed computational techniques combined with the Surface Evolver software [38].

One active area of theoretical research in vesicle characterization involves the confine-

ment of phospholipid vesicles within various types of cavities [110, 76, 36, 79, 111, 78]. Despite growing interest, experimental studies in this domain remain limited, and only a few relevant investigations can be cited.

Sakashita et al. studied the morphological transformations of lipid vesicles confined within spherical vesicles to explore new vesicle shapes induced by confinement[37]. Using fast confocal laser microscopy combined with numerical simulations based on a dynamically triangulated membrane model incorporating the ADE model, they observed previously unreported vesicle morphologies such as double and quadruple stomatocytes, slit vesicles, and vesicles partitioned into multiple compartments.

Experimentally, vesicles consisting of single-component lipids (1,2- dioleoyl-sn-glycero-3-phosphocholine, DOPC) exhibited a variety of distinctive morphologies driven primarily by spatial confinement. The simulation results closely matched the experimental observations, providing robust support for the ADE model as an accurate framework to interpret shape dynamics under confinement. By varying parameters such as the reduced volume and intrinsic area differences between membrane leaflets, the authors systematically mapped the observed vesicle shapes onto morphological phase diagrams (see Figs. 1 and 3 in [37]).

Specifically, confinement-induced shapes resembled biological structures, such as mitochondrial cristae (folds in the inner membrane of the mitochondrion), highlighting the broader biological relevance of their findings. In addition, transitions between different shapes and hysteresis behaviors associated with shape transformations were identified in this combined theoretical and experimental study.

In another mainly theoretical study, Kavčič et al. extensively explored the limiting shapes of lipid vesicles under confinement within spherical cavities, employing both BC and ADE theoretical frameworks [77]. They systematically categorized confined vesicle shapes into distinct morphological classes, explicitly addressing both compartmentalized and non-compartmentalized shapes. Using simplified geometric structures, including flat, spherical, and cylindrical surfaces, they developed an analytical approximation known as the "tight confinement approximation".

The tight confinement approximation refers to a controlled asymptotic limit in which the vesicle volume V nearly saturates the confining cavity V', i.e., the packing fraction

$Z = V/V' \to 1$. In this regime, the membrane is in contact with the confining wall almost everywhere, and the dominant contributions to the bending energy arise from narrow, highly curved edge or neck regions where the remaining free volume is localized. The approximation consists of neglecting small curvature components along these edges while retaining the diverging transverse curvature, which allows the authors to compute area, volume, area difference, and bending energy analytically and to construct limiting shape classes and phase boundaries. This tight confinement approximation therefore represents a subset of the strong confinement regime, designed specifically to extract analytical insight into vesicle morphologies near maximal packing, rather than to describe the full range of deformation pathways encountered at finite confinement sizes.

Their analysis revealed a wide variety of vesicle shapes, including single-compartment configurations such as invaginated torocytes and U-shaped vesicles, two-compartment forms such as double stomatocytes, and more intricate three-compartment configurations. The authors demonstrated how transitions among these shapes are governed by the reduced volume and reduced area difference, which they used for the construction of phase diagrams within the ADE framework (see Figs. 5, 6 and 7 in [77]).

Furthermore, the authors compared their theoretical results for the predicted vesicle shapes inside a spherical vesicle (size around $10\mu m$) with the experimental observations they obtained using fast confocal microscopy of single-component vesicles (DOPC) at room temperature. They noted that their observations here were a qualitative confirmation of their theoretical predictions for tightly confined vesicles.

2.3 Numerical Calculation of Helfrich's Bending Energy

When the goal is to calculate the 3D shape of a vesicle using the Helfrich equation (2.2), the general approach involves minimizing this energy to obtain the equilibrium shape. However, in addition to energy minimization, the equilibrium shape must satisfy specific surface area and volume constraints, which must be incorporated into the minimization process. This can be accomplished by including these constraints using the method of Lagrange

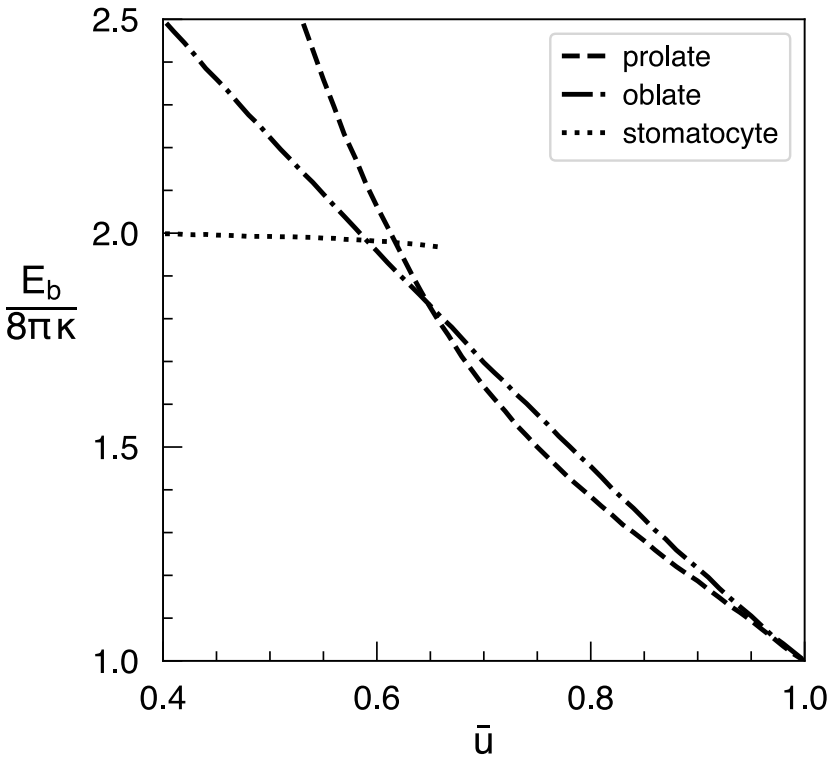


Figure 2.2: Minimum bending energy (normalized by the bending energy of a sphere) of prolate, oblate and stomatocyte shapes vs. the reduced volume (normalized by the volume of a sphere). The data for this diagram was obtained by digitizing Fig. 8 in [31].

multipliers. Consequently, shape determination becomes a variational problem for the bending energy, subject to constraints on the surface area A and volume V [96, 30, 32].

Numerical approaches to this variational problem require a spatial characterization of the vesicle membrane in order to represent constrained energy minimization through the resulting 3D morphology. One such approach achieves this by parameterizing the membrane using arc length, which forms a two-dimensional (2D) contour that is subsequently revolved to generate the three-dimensional shape. The energy functional, along with the constraints on surface area and volume, is then written in terms of this arc length. Numerically, the minimization of the resulting Euler–Lagrange equations can be carried out

using various methods—for example, by converting the equations into a system of ordinary differential equations, or by directly treating the governing equations for bending energy, surface area, and volume using finite-difference methods or Monte Carlo techniques [96, 31, 112, 113, 114].

The primary limitation of this method is that it is intrinsically restricted to three-dimensional axisymmetric shapes, since the reduction to a 2D contour relies explicitly on rotational symmetry. In this formulation, the 2D problem must first be solved, and the resulting shape is then extended to 3D by symmetry, making non-axisymmetric morphologies inaccessible within this framework. One of the major accomplishments of this approach is illustrated in Fig. 2.2, which is reproduced using digitized data from [31]. The figure shows the bending energy (normalized by that of a sphere) of the main axisymmetric vesicle shapes as a function of reduced volume (the vesicle volume normalized by that of a sphere).

Using various surface discretization methods—where a 2D surface embedded in 3D space is represented by a set of points (nodes)—the numerical minimization of the bending energy can be extended to more general cases beyond axisymmetric shapes. In these approaches, integration and differentiation are performed through numerical approximations or interpolations based on the discretization nodes. Several techniques utilize these nodes to compute the bending energy, including:

- Flat triangle meshes or spring networks built upon triangular elements,
- Higher-order elements such as curved triangles,
- Subdivision methods, which introduce new nodes based on refinement rules,
- Spectral methods using basis function expansions, such as spherical harmonics or Fourier series,
- Cubic B-splines and nonuniform rational B-splines (NURBS) for constructing smooth, twice-differentiable surfaces,
- The level-set method,

- The 3D phase-field model, which assigns a scalar field to the spatial domain.

Each of these techniques enables the computation of vesicle shapes [50].

These techniques are implemented in various ways in practice. For instance, the principle of virtual work may be applied, or more direct approaches (referred to as strong formalisms) can be used, where the fourth-order derivatives arising from variational calculus and leading to the Euler–Lagrange equation for the bending energy are treated analytically using geometric arguments, or numerically via finite-difference schemes, such as the cotangent method for the differentiation operator [50, 51]. In addition, the finite element method (a weak formalism) can be coupled with surface representation techniques to effectively reduce the order of derivatives from four to two [50]. For example, an adaptive finite element method has been applied to the phase-field formulation of the Helfrich bending energy [115], and Brakke's Surface Evolver package uses a triangulation-based representation of the surface (a finite element method in nature), incorporating a combination of exact expressions and finite-difference approximations to compute the surface curvature derivatives [38].

The techniques and numerical approaches discussed so far are not limited to calculating the bending energy and equilibrium shapes of vesicles in static conditions. A substantial body of research focuses on vesicle behavior in hydrodynamic flows, such as shear flow, where hydrodynamic forces induce membrane deformations and alter vesicle morphology. These scenarios require coupling fluid dynamics with Helfrich bending energy calculations to capture the dynamic evolution of vesicle shapes.

Various numerical schemes have been developed and applied to model vesicles in fluid flow, including the immersed boundary method, boundary integral method, and multiparticle collision dynamics [116, 117, 118, 119, 120, 121, 122]. The phase-field model has also been widely used for vesicle dynamics due to its straightforward treatment of the membrane as a diffuse interface. Multiple research groups have conducted extensive analytical and numerical studies on vesicle deformation and shape transitions in hydrodynamic flow using the phase-field framework [46, 123, 124, 125].

A major challenge with surface discretization methods, such as triangulation, is the need to track the evolving surface, which can suffer from mesh entanglement and irregularity.

This necessitates remeshing schemes, thereby increasing the complexity of the numerical treatment [50]. A phase-field approach to the Helfrich model circumvents these issues by extending the phase field across the entire computational domain that contains the vesicle. This eliminates the need to explicitly track the deformable surface (i.e., the diffuse interface) [45, 126].

One of the most commonly used numerical tools for calculating equilibrium vesicle shapes is Brakke's Surface Evolver package, which minimizes the bending energy subject to constraints such as surface area and volume [38]. A comparison between the Surface Evolver framework and the phase-field framework for bending energy minimization is warranted, particularly in light of our use of the phase-field formulation for modeling the deformable membrane of phospholipid vesicles in 3D. This formulation serves as the foundation for our proposed neural network (NN) solver, which is then used to calculate a variety of vesicle shapes under different constraint conditions.

Both Surface Evolver and phase-field models offer powerful frameworks for modeling the shapes of bilayer vesicles, but they differ significantly in their assumptions, implementation, and scope. For equilibrium shape calculations, Surface Evolver provides a direct and efficient method by minimizing the bending energy (via gradient descent) over a triangulated surface with fixed constraints [38]. It can capture a wide range of known vesicle morphologies and supports constraints on surface area, volume, and even bilayer leaflet area difference [34, 35]. However, its reliance on a discrete mesh means that resolving sharp features or narrow necks requires significant mesh refinement. Additionally, the method often converges to a local minimum, necessitating multiple runs with varied initial conditions to explore the full shape landscape.

In contrast, phase-field models represent the membrane as a diffuse interface and recover equilibrium shapes by solving a variational problem for the bending energy [45, 48]. These models can naturally produce asymmetric (e.g., non-axisymmetric) shapes by imposing various types of constraints, handle abrupt transitions when instabilities arise, and accommodate complex morphologies without requiring remeshing. In fact, meshfree schemes have been developed for the phase-field approach [127]. However, convergence to equilibrium is typically slower and more computationally intensive, primarily due to the high-resolution grids needed to resolve sharp interfaces.

In terms of modeling dynamics, Surface Evolver is inherently limited—it does not simulate temporal evolution but instead generates static configurations for a given set of constraints. It cannot capture shape transitions, dynamic instabilities, or topological changes such as vesicle fission, largely due to its reliance on mesh tracking. In contrast, phase-field methods are specifically designed for dynamic simulations. They can model time-dependent phenomena such as budding, shape transformations, and even vesicle splitting or fusion, all within a consistent framework [128]. These methods also allow coupling with hydrodynamics, making them well suited for studying vesicle behavior in flow or under external forces [46, 123, 124, 125, 129].

Numerically, Surface Evolver is relatively lightweight and straightforward to implement. It offers efficient computations and rapid convergence for static problems, and is accessible to users interested in calculating equilibrium shapes under various physical constraints. However, it lacks the flexibility needed for modeling dynamic processes or systems undergoing topological changes. Phase-field models, while more computationally demanding—especially in 3D—provide a unified framework for both equilibrium and dynamic behavior. They require careful numerical treatment of higher-order PDEs and are more complex to implement, but they can accommodate a broader range of physical phenomena, including multicomponent membranes [128] and local incompressibility constraints [46, 48].

In summary, Surface Evolver is best suited for precise equilibrium studies where shape transitions or topological changes are not expected, and the simulation goals are compatible with the software's mesh-based framework. In contrast, phase-field approaches are indispensable for investigating vesicle dynamics and are better suited for scenarios requiring greater flexibility, adaptability, and versatility.

2.4 Application of Machine Learning to Vesicles

The use of artificial neural networks (ANNs) has become a cornerstone of machine learning (ML) techniques. Their capability as universal approximators of continuous functions was established in early foundational work [57, 58, 59]. As differential equation solvers, ANNs have been implemented as viable numerical alternatives to conventional schemes for solving

ordinary and partial differential equations (ODEs and PDEs) [130, 131, 132, 133, 134, 135]. The central idea in these studies is that a simple feedforward neural network can represent the trial solution of a numerical problem. By minimizing an error or loss function—constructed from the residuals of the governing ODE or PDE, along with penalty terms enforcing boundary or initial conditions—the network output converges toward the actual solution. A key advantage of this method is that the solution is represented as a continuous, differentiable function over the domain, rather than as a discrete set of values evaluated at mesh or grid points.

In recent years, the advent of deep learning [56] and the development of machine learning libraries such as PyTorch, TensorFlow, and JAX, which streamline the implementation of scientific computing algorithms, have significantly renewed interest in applying neural networks to the solution of partial differential equations (PDEs). This is especially true for high-dimensional PDEs, which traditionally suffer from the curse of dimensionality [136], and have now become more tractable using deep neural network approaches [137, 138, 139, 140, 141].

The introduction of physics-informed neural networks (PINNs) has initiated a new paradigm in numerical methods for solving PDEs [63, 64]. This approach is particularly well-suited for problems governed by nonlinear PDEs. The central idea is to embed the structure of the governing equations directly into the training process by penalizing the residuals of the PDE in the loss function. This enables the learned solution to incorporate both observational data and known physical laws. The PINN framework has also been extended to inverse problems, where unknown parameters are inferred and latent quantities—such as pressure fields—are reconstructed solely from auxiliary observations, even in the absence of direct measurements. In other words, PINNs have demonstrated capabilities for both solving and discovering PDEs.

While PINNs are primarily designed to solve partial differential equations by embedding governing equations into the training loss, their application to vesicle shape modeling via phase-field formulations has thus far been limited, particularly for equilibrium problems. More recently, Poudel et al. introduced a distinct neural-network-based framework—Functional Optimization using Neural Networks (FONN)—aimed at directly minimizing energy functionals defined on discretized spatial domains rather than evolving a time-

dependent PDE [142].

The proposed FONN framework is used to minimize the Helfrich bending energy under a global area constraint in 2D. The scalar field $\phi(x, y)$ is defined on a fixed uniform grid, and a neural network does not parameterize $\phi(x, y)$ globally. Instead, two trainable networks learn local update rules that propagate information between neighboring grid points through a message-passing mechanism. One network (f_R) models interactions between adjacent nodes, while the other (f_O) updates the value of $\phi(x, y)$ at each node based on the accumulated local interactions (these are both feedforward neural networks, but each has a different number of input nodes). Energy minimization is achieved through a progressive training strategy in which successive applications of these learned local updates reduce the total energy, bypassing explicit time stepping and traditional gradient flows [142].

While this approach shows promise for calculating equilibrium vesicle shapes, its extension to 3D geometries and its capability to produce quantitative results, such as bending energy vs. reduced volume plots or phase diagrams, has not yet been explored.

Conceptually, FONN replaces traditional finite-difference update rules with neural networks: instead of using fixed numerical stencils to compute how the phase field should change on a grid, the neural networks learn these local update rules directly from the energy minimization process, while the field itself remains defined on a fixed spatial grid. In contrast, the NN solver developed in this thesis adopts a continuous, meshfree parameterization of the phase field itself via a compact feedforward neural network, enabling direct functional minimization using automatic differentiation for spatial derivatives. This distinction highlights two complementary NN-based paradigms for variational problems: learning local update rules on discretized domains (FONN) versus learning a global parametric representation of the solution to the Helfrich model (our NN solver).

With the increasing volume of experimental research on lipid bilayers and phospholipid vesicles, ML techniques, particularly deep neural networks, are becoming increasingly prevalent. These methods are being applied to analyze experimental data for various purposes, such as image processing and denoising [143]. In a recent study, convolutional neural networks (CNNs) were employed to automate the analysis of fluorescence microscopy images of giant unilamellar vesicles (GUVs), addressing a persistent challenge in vesicle

research: the subjective and time-intensive nature of manual image classification [144].

The authors developed a modular software toolset, GUVanalysis, which integrates CNN-based classification routines with conventional pixel-intensity calculations to enable a high-throughput and reproducible analysis of vesicle morphology and phase state. The CNN was trained to identify valid unilamellar vesicles and to distinguish phase-separated vesicles from homogeneous ones, using both experimentally acquired images and synthetically generated training data to improve generalization and accuracy. This study highlights how CNNs can serve as effective surrogates for expert visual analysis in soft matter microscopy, particularly in applications requiring large-scale statistical sampling of vesicle shapes and phase behavior.

Deep learning techniques are not limited to analyzing experimental data; they are also increasingly applied to outputs from molecular dynamics (MD) simulations of lipid bilayers. For example, a recently introduced hybrid computational framework combines MD simulations with deep learning to predict the free energy of permeation for small drug-like molecules across lipid bilayers [145]. Recognizing the limitations of traditional methods such as umbrella sampling, which are computationally intensive and time-consuming, this framework aims to accelerate and improve the accuracy of permeability predictions, a critical factor in both drug development and membrane biophysics.

In this approach, coarse-grained MD simulations are used to generate multidimensional time-series data that capture the interactions of solute molecules within aqueous environments and lipid bilayers. These datasets serve as input for two deep learning models: one based on Long Short-Term Memory (LSTM) layers, and another incorporating LSTM layers with attention mechanisms. Both models are designed to capture temporal dependencies and extract salient features from the simulation trajectories. The results demonstrate strong predictive performance, with the basic LSTM model achieving high accuracy on test datasets, indicating a strong correlation with reference free energy values. Notably, these deep learning models significantly reduce computational costs, providing predictions in a fraction of the time required by conventional MD-based methods.

2.5 Phase Field Model

The phase field model and its application to interfacial problems can be traced back to Landau's theory for free energy expanded in powers of a scalar field ϕ, also known as the order parameter [146]. The more generalized theory by Ginzburg and Landau extended this approach by including first- and second-order gradients of the field, accounting for the energetic effects of interface formation [71, 126]. In a related approach, the phenomenon of phase separation in binary solutions and alloys was described by considering an intensive scalar quantity, such as the fluid/alloy concentration, which characterizes the coexisting phases. The temporal evolution of this process was shown to be well described and mathematically governed by the Cahn–Hilliard and Allen–Cahn equations for solutions and alloys, respectively [147, 148].

The application of the phase-field model to the problem of finding the equilibrium shape of vesicles made of deformable membranes has a strong foundation in classical field-theoretic approaches to interfacial problems. Instead of discretizing the membrane directly, e.g., using a triangulation mesh, a scalar phase field $\phi(\mathbf{r})$ is assigned to each point in the 3D space, with values ranging between ± 1. The morphology of the vesicle is determined by the position of the interface, which is formed by intermediate values of the phase field. Inside the vesicle, far from the interface, the phase field is $\phi(\mathbf{r}) = +1$, and similarly outside the vesicle in the far-field limit, $\phi(\mathbf{r}) = -1$. This is shown graphically in Fig. 2.3, where a schematic diagram of a spherical vesicle is used as an example. The interface is depicted by a transition of colors from lighter to darker in the diagram. The thickness of the interface is determined by the characteristic length parameter ϵ, which is schematically shown between the yellow dashed lines.

2.5.1 Phase-field Approach to Helfirch Model

Using this definition to determine the 3D shape of the vesicle membrane, the bending energy defined by (2.2) is rewritten by incorporating a derivation of the mean curvature in terms of $\phi(\mathbf{r})$ and $\nabla^2\phi(\mathbf{r})$, constrained by the specified surface area and volume (both defined in terms of $\phi(\mathbf{r})$ and $\nabla\phi(\mathbf{r})$). This expression is then minimized by numerically

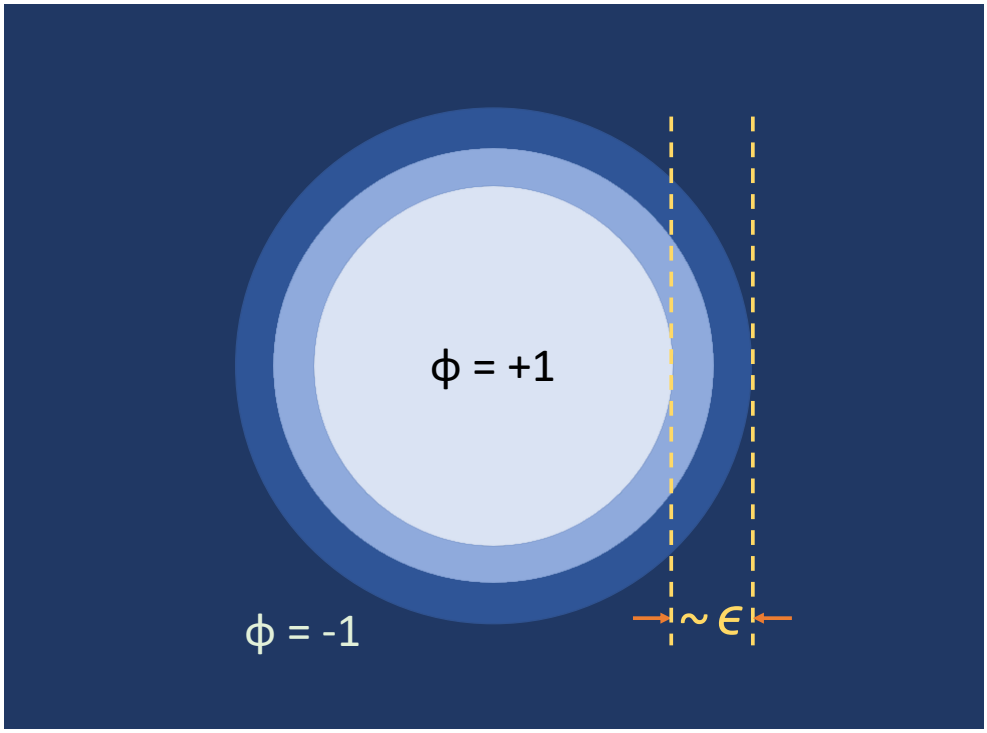


Figure 2.3: Cross-sectional schematic of a spherical vesicle, characterized by assigned values of a phase field. The interior has $\phi(\mathbf{r}) = 1$, and the exterior has $\phi(\mathbf{r}) = -1$. The interface is delineated by shades of blue, which are lighter toward the inside and darker toward the outside. Here, ϵ is a length scale that characterizes the interface thickness.

solving the resulting Euler-Lagrange equations. Conventional approaches to numerical solution have employed finite difference schemes, Fourier spectral methods, finite element analysis, and time integration schemes such as the semi-implicit Euler method [45, 47, 48, 115, 127, 49, 149]. However, in this thesis, we introduce a completely different and novel scheme to carry out the numerical calculations that determine the solution to the underlying variational problem. For this purpose, we adopt the phase-field treatment of the Helfrich model introduced in [45].

In Appendix A, we show the detailed steps for reformulating the Helfrich model using the phase field model following [150]. The starting point is to take an ansatz for the phase field, namely $\phi(\mathbf{r}) = \tanh(d(\mathbf{r})/\sqrt{2}\epsilon)$, where $d(\mathbf{r})$ is the signed distance from the interface,

and calculate an expression for the mean curvature. As it turns out, this particular ansatz is the minimizer solution of the Helfrich's bending energy functional written in its phase-field formulation [45, 48]. We later show that the approach adopted by [48] can be used to demonstrate that the proposed ansatz is a solution to the phase-field formulated Helfrich bending energy functional.

In another approach laid out in Appendix B, we use a different analytical derivation to obtain a phase-field-based expression for the mean curvature. To this end, we introduce a functional ansatz for the surface area, which is inspired by the Ginzburg–Landau energy functional [71, 126].

The expression for the mean curvature in terms of a tanh-like phase field is given by

$$H[\phi] = -\frac{\epsilon}{\sqrt{2}\,(1-\phi^2)}\left[\nabla^2\phi + \frac{1}{\epsilon^2}\phi(1-\phi^2)\right]. \tag{2.4}$$

This expression for the mean curvature provides a pathway for rewriting the Helfrich model, specifically (2.2), to incorporate the phase-field formalism. In Appendix A, we show how the surface integral in (2.2) can be converted to a volume integral for calculating the bending energy of a phase-field-modeled vesicle.

The bending energy $E_b[\phi]$, reformulated using the phase-field model, can be minimized subject to constraints on the membrane surface area $A[\phi]$ and the enclosed vesicle volume $V[\phi]$. This leads to the following variational problem for determining the minimizing phase field ϕ:

$$\frac{\delta E_b[\phi]}{\delta\phi} + \lambda_A\frac{\delta A[\phi]}{\delta\phi} + \lambda_V\frac{\delta V[\phi]}{\delta\phi} = 0, \tag{2.5}$$

where $\delta/\delta\phi$ denotes the functional derivative with respect to the phase field ϕ, and λ_A and λ_V are the Lagrange multipliers enforcing the area and volume constraints, respectively. This is one of the most common formulations for computing equilibrium vesicle shapes [45, 47, 150], and it can be solved numerically using traditional methods such as finite-difference approximations and gradient descent.

In another common approach, surface area and volume constraints are imposed through penalty terms in the phase-field energy functional rather than via Lagrange multipliers [45, 52, 150, 49]. This approach is more straightforward, since the coefficients of the penalty terms are chosen as large constant values and, unlike Lagrange multipliers, do not need to be updated during the numerical calculations.

Campelo et al. in Ref. [48] adopt a different approach to formulating the phase-field representation of the Helfrich energy functional, as well as a distinct minimization dynamic for solving the variational problem associated with constrained equilibrium shapes. They introduce the following ansatz for the free energy functional, denoted by $\mathcal{F}$ (to distinguish it from E_b), which is inspired by the Cahn–Hilliard equation [147]. In this formulation, the integrand is the square of the chemical potential, which is defined as the functional derivative of the free energy:

$$\mathcal{F}[\phi] = \int \left[-\phi(\mathbf{r}) + \phi(\mathbf{r})^3 - \epsilon^2 \nabla^2 \phi(\mathbf{r})\right]^2 \mathrm{d}\mathbf{r}, \tag{2.6}$$

where ϵ is the length scale characterizing the interface width, and $\phi(\mathbf{r})$ is the phase field with the same properties as before: $\phi = +1$ inside the vesicle, $\phi = -1$ outside, and a transition layer centered around $\phi = 0$ where the field changes between these two values.

The phase field is defined as a regular function of the signed distance $d(\mathbf{r})$, scaled by the interface width ϵ, namely $\phi(\mathbf{r}) = f(Cd(\mathbf{r})/\epsilon)$, where C is an undetermined constant. With this definition of the phase field, we have

$$\begin{aligned} \nabla\phi &= \frac{C\nabla d(\mathbf{r})}{\epsilon} f', \\ \nabla^2\phi &= \frac{C^2}{\epsilon^2} f'' + \frac{C\nabla^2 d(\mathbf{r})}{\epsilon} f', \end{aligned} \tag{2.7}$$

where $|\nabla d(\mathbf{r})|^2 = 1$ is used [151]. Using (2.7), the ansatz (2.6) can be rewritten in terms of $f(Cd(\mathbf{r})/\epsilon)$

$$\mathcal{F}[f] = \int \left[C^2 f'' + f(1-f^2) + C\epsilon f' \nabla^2 d(\mathbf{r})\right]^2 \mathrm{d}\mathbf{r}. \tag{2.8}$$

In the limit $\epsilon \to 0$, the minimum of the energy functional (2.8) is attained when

$$C^2 f'' + f(1 - f^2) = 0. \tag{2.9}$$

The solution to this equation takes the form $\tanh(Cd(\mathbf{r})/\epsilon)$, which satisfies the equation when $C = 1/\sqrt{2}$. Therefore, the phase field solution becomes $\phi(\mathbf{r}) = \tanh(d(\mathbf{r})/\sqrt{2}\epsilon)$. Substituting this expression back into (2.8), one obtains

$$\mathcal{F}[f] = \int \frac{\epsilon^2}{2} \left(1 - \tanh^2\left(\frac{d(\mathbf{r})}{\sqrt{2}\epsilon}\right)\right)^2 |\nabla^2 d(\mathbf{r})|^2 \mathrm{d}\mathbf{r}, \tag{2.10}$$

or equivalently

$$\mathcal{F}[f] = \frac{8\sqrt{2}\epsilon^3}{3} \int \frac{3}{4\sqrt{2}\epsilon} \left(1 - \tanh^2\left(\frac{d(\mathbf{r})}{\sqrt{2}\epsilon}\right)\right)^2 |\frac{1}{2}\nabla^2 d(\mathbf{r})|^2 \mathrm{d}\mathbf{r}. \tag{2.11}$$

In the sharp interface limit ($\epsilon \to 0$), the expression,

$$\frac{3}{4\sqrt{2}\epsilon} \left(1 - \tanh^2\left(\frac{d(\mathbf{r})}{\sqrt{2}\epsilon}\right)\right)^2 \approx \delta(d(\mathbf{r})) \tag{2.12}$$

approximates the Dirac delta function $\delta(d(\mathbf{r}))$. This approximation allows the volume integral to be converted into a surface integral:

$$\mathcal{F}[d] \sim \int_S |\frac{1}{2}\nabla^2 d(\mathbf{r})|^2 \mathrm{d}S, \tag{2.13}$$

where $\nabla^2 d(\mathbf{r})$ corresponds to the negative of the sum of the local principal curvatures of the surface [152, 153], and thus the integrand in (2.13) represents the square of the mean curvature. Consequently, the ansatz for the free energy functional in (2.6) serves as the phase-field equivalent of the Helfrich bending energy, with the spontaneous curvature set to zero. For nonzero spontaneous curvature, it can be shown that the full Helfrich energy given by (2.2) is recovered [48].

To enforce the area constraint, Ref. [48] argues that the lipid membrane does not exchange a significant number of molecules with the surrounding medium. Furthermore,

under the assumption of local membrane incompressibility, the following effective free energy functional is introduced, incorporating a constraint on the local area of the membrane:

$$\mathcal{F}_{eff}[\phi] = \mathcal{F}[\phi] + \int \sigma(\mathbf{r}) a[\phi] \mathrm{d}\mathbf{r}, \tag{2.14}$$

where $\sigma(\mathbf{r})$ is a local Lagrange multiplier and $a[\phi]$ is the local surface area assumed to have the form

$$a[\phi] = \frac{3}{2\sqrt{2}} \epsilon |\nabla \phi|^2. \tag{2.15}$$

When the expression for $a[\phi]$ is combined with the hyperbolic tangent solution, it yields a delta function that peaks at the interface location—specifically, the expression in (2.12) in the limit $\epsilon \to 0$. Consequently, the volume integral of $a[\phi]$ becomes equivalent to a surface integral in the sharp interface limit, recovering the total surface area of the vesicle.

To impose a volume constraint for impermeable vesicles, the authors in Ref. [48] employ a Model-B type dynamics, given by

$$\frac{\partial \phi}{\partial t} = \nabla^2 \left(\frac{\delta \mathcal{F}_{eff}}{\delta \phi} \right), \tag{2.16}$$

which ensures the conservation of the volume integral of the phase field, i.e., $\int \phi(\mathbf{r}), \mathrm{d}\mathbf{r} =$ const.

The bending energy vs. the reduced volume diagram reported in Ref. [48] is shown in Fig. 2.4. The data obtained by numerically solving (2.16)—using a second-order finite difference for spatial approximations and the Euler scheme for time integration—is represented by the gray symbols and error bars. These data points overlap the lines reproduced by the data from Fig. 8 in [31], indicating consistency between the two approaches. However, the number of data points is insufficient to construct the complete diagram using the phase-field formulation of the Helfrich energy proposed in [48].

Campelo et al. argue that using (2.16) to minimize the bending energy is more appropriate, as the enclosed volume of the vesicle remains fixed under Model-B dynamics, which ensures the conservation of the phase field (order parameter) [154]. In contrast, they contend that the phase-field formulation leading to (2.5), as proposed and used in [45, 47], does not inherently conserve the internal volume of the vesicle.

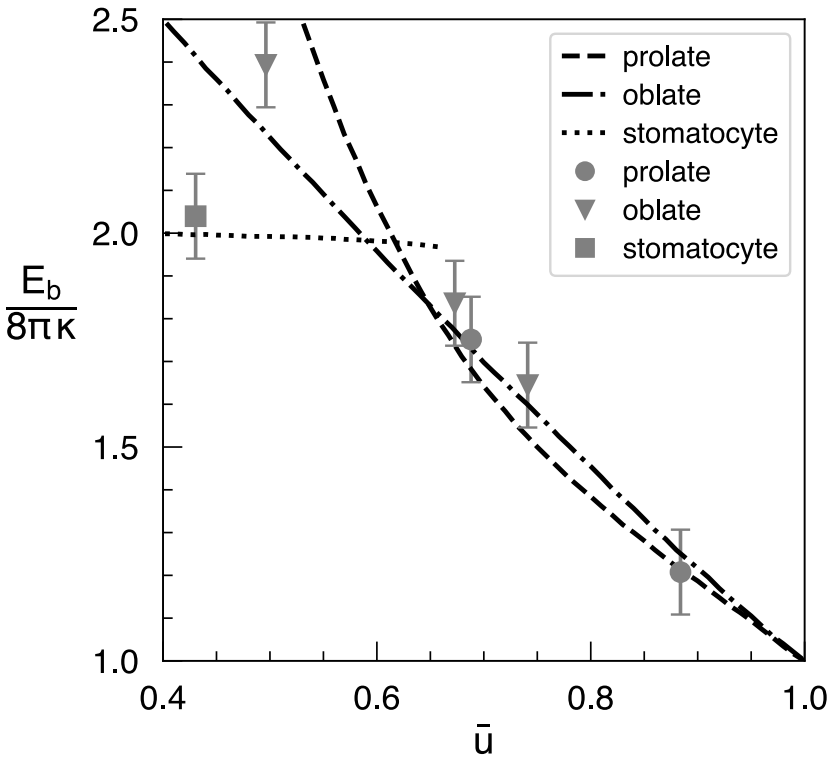


Figure 2.4: Minimum bending energy (normalized by the bending energy of a sphere) of prolate, oblate and stomatocyte shapes vs. the reduced volume (normalized by the volume of a sphere). The gray symbols with error bars are reported by Campelo et al. [48] and the lines are included as reference (obtained by digitizing Fig. 8 in [31]).

As explained earlier, the inner volume of the vesicle is enforced through a Lagrange multiplier, λ_V, as shown in Eq.(2.5). One could argue that Eq.(2.5) resembles Model-A dynamics, which is typically used for systems with non-conserved order parameters [154]. However, in the formulation adopted by Refs. [45, 47], the non-conserving nature of Model-A dynamics is addressed by explicitly incorporating the volume constraint into the energy functional.

In Chapter 3, we present the formulation of this problem within our neural network solver. Specifically, we show that the minimization method employed in our approach—

where the phase-field model is represented by an ansatz encoded in a feedforward neural network—leads to a parametric energy minimization framework. Although this formulation is conceptually similar to the variational equation given in Eq. (2.5), it differs in that it does not involve functional derivatives with respect to the phase field ϕ. Instead, it is based on derivatives with respect to the network parameters, which collectively represent the phase-field solution.

2.5.2 Phase-field Approach to Area Difference Modeling

Typical lipid bilayer thickness is about 4-5 nanometers, which is relatively small compared to the overall size of a vesicle [20]. As a result of this characteristic, the two monolayers (leaflets) comprising the bilayer exhibit a difference in their surface areas. In Fig. 2.5, a schematic of a spherical vesicle in 2D illustrates this effect. The internal surface of the vesicle (A^{in}) is smaller than the external surface (A^{ex}). This area difference is proportional to the bilayer thickness, indicated by the separation distance s; the thinner the bilayer, the smaller the area difference.

The area difference model (this model is referred to as bilayer-coupling model in [31]) seeks to quantify this disparity between the internal and external surface areas. The assumption here is that the monolayers maintain fixed surface areas and that no exchange of lipid molecules occurs between them [31, 73]. The difference in area, $\Delta A = A^{\text{ex}} - A^{\text{in}}$, can be calculated using a reference surface, with area A and mean curvature H, located between the two monolayers. The position of this reference surface depends on the bending moduli (κ) of the monolayers; for identical moduli, the surface is positioned halfway between the internal and external surfaces [31]. Quantitatively, the area difference, up to order s^2/A, is proportional to the surface integral of H (the mean curvature of the reference surface), denoted by M:

$$\Delta A \approx 2sM = 2s \int_S H \mathrm{d}S. \tag{2.17}$$

This expression provides the means to calculate the area difference from the mean

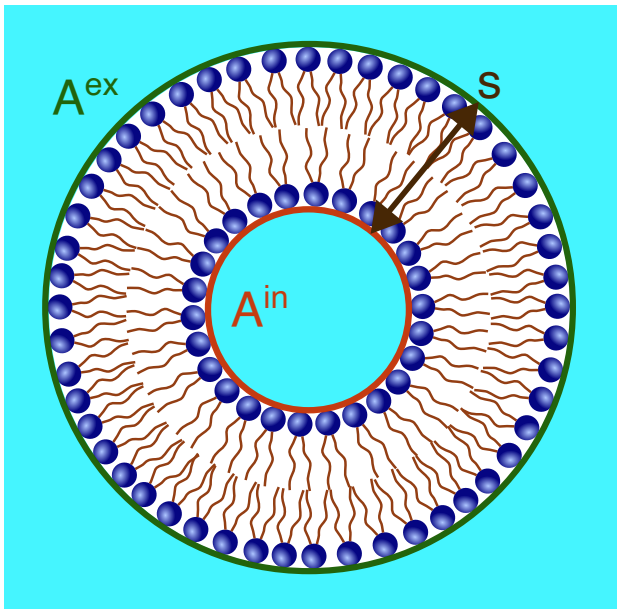


Figure 2.5: Cross-sectional schematic of a spherical vesicle, with the constituent bilayer shown for reference. The interior monolayer has a surface area (red circle) denoted by A^{in}, while the exterior monolayer has a surface area (green circle) denoted by A^{ex}. The leaflets (monolayers) are separated by a distance s.

curvature. Using (B.13), we have

$$M = \int_S -\frac{\epsilon}{\sqrt{2}\,(1-\phi^2)} \left[\nabla^2\phi + \frac{1}{\epsilon^2}\phi(1-\phi^2)\right] \mathrm{d}S, \tag{2.18}$$

for a phase-field approach to calculating the area difference given by (2.17). Later in this thesis, we show how (2.18) is converted to a volume integral and how M is used to introduce a dimensionless quantity for the area difference, namely the reduced area difference Δa, which equals one for a spherical vesicle. It has been shown that for a range of values of Δa and reduced volume (non-dimensionalized volume), the shapes of vesicles become non-axisymmetric in free space [35, 74]. We will show examples of these shapes, such as starfish, in Chapter 4, where we detail the inclusion of area difference as an additional constraint in the variational problem for determining the equilibrium shape.

We emphasize that the phase-field area difference model presented here is based on the

bilayer-coupling model [31, 73], which represents a limiting case of the more general area-difference-elasticity (ADE) model. In the ADE framework, the actual (or calculated) area difference and the preferred (or relaxed) area difference are not necessarily equal, leading to an additional contribution to the total energy known as the non-local bending energy. In the special case where the actual and preferred area differences coincide, the ADE model reduces to the bilayer-coupling model [108, 155].

Chapter 3

Artificial Neural Networks for Phase Fields

In this chapter, we provide background on artificial neural networks and describe the implementation of the backpropagation algorithm for updating the weights and biases that collectively define the network parameters. We then demonstrate how this neural network framework is applied to solve the phase-field formulation of the Helfrich model. Specifically, we show that when the original problem is mapped onto a neural network representing the phase field, the solutions that satisfy the imposed constraints correspond to those that minimize the network's cost function. In the following chapter, we validate these numerical solutions by reproducing the bending energy versus reduced volume diagram for axisymmetric vesicle shapes.

3.1 Artificial Neural Networks

Artificial neural networks (NNs) are computational models inspired by the structure and function of the human brain. They are generally composed of multiple layers, each containing a set of interconnected processing units known as neurons (or nodes). The earliest model of a neuron, known as a perceptron, was introduced in the 1940s as a simple unit

that computes a binary output from a set of binary inputs [53]. This idea was further developed in the 1960s with the introduction of multilayer architectures, leading to what are now known as multilayer perceptrons (MLPs) [54]. These early developments laid the foundation for modern neural networks, including the key architectural features of layered structures and neuron-based computation.

A typical neural network (NN) consists of three types of layers: the input layer, one or more hidden layers, and the output layer. The input layer comprises neurons that receive raw input data, such as floating-point values representing coordinates in three-dimensional space (3D) or pixel intensities in an image. These neurons are connected to neurons in the subsequent layer—usually the first hidden layer—via weighted connections and nonlinear activation functions. Each neuron in the hidden layer receives a linearly weighted sum of its inputs, along with a bias term, which is then passed through a non-linear activation function to produce the neuron's output [55].

Formally, if the jth input neuron has value z_j, the input to the ith neuron in the next layer is given by $\sum_j w_{ij} z_j + b_i$, where w_{ij} is the weight associated with the connection from neuron j to neuron i, and b_i is the bias term. The weights and biases together constitute the trainable parameters of the neural network. This process is repeated layer by layer until the network produces an output in the final layer. Neural networks that follow this structure—where neurons are fully connected between adjacent layers and information flows strictly forward—are known as fully connected feedforward neural networks. In contrast, recurrent neural networks (RNNs) allow connections within the same layer or between non-adjacent layers, enabling the modeling of temporal or sequential data [156, 157].

Activation functions introduce nonlinearity into neural networks, enabling them to approximate complex, nonlinear mappings. One of the most well-known activation functions is the sigmoid function, defined as

$$\sigma(u) = \frac{1}{1 + e^{-u}}, \tag{3.1}$$

which maps real-valued inputs into the interval (0, 1). Originally inspired by binary threshold units in the perceptron model, the sigmoid function provides a smooth, differentiable approximation of a binary switch.

Other widely used activation functions include the hyperbolic tangent (tanh), rectified linear unit (ReLU), softplus, and Gaussian functions. These functions are selected based on the specific task or architecture. For example, the ReLU function, defined as $\max(0, u)$, has become the default activation function in many deep learning applications, particularly in convolutional neural networks (CNNs) used for image classification tasks [158]. Each activation function brings different advantages in terms of gradient flow, computational efficiency, and representational capacity, making the choice of activation function a crucial design decision in neural network architecture.

Neural networks are considered universal approximators, meaning they can approximate any continuous function to arbitrary accuracy, provided they have sufficient depth and width in their architecture [57, 58, 59]. In essence, when an NN is trained on a specific task, it learns a function that maps a set of input variables to a desired output with high precision. For neural networks designed to approximate scalar-valued functions—whether with single or multiple inputs—there exist theoretical results that prescribe the necessary number of hidden layers and neurons to achieve a high level of approximation accuracy [159, 160].

3.1.1 Feedforward Neural Networks with an Example

The architecture of a typical feedforward neural network (FNN) is illustrated schematically in Fig. 3.1. FNNs are widely used for tasks such as function approximation and classification. In the following sections, we demonstrate how an FNN is employed in our proposed neural network-based solver for calculating vesicle shapes.

One of the well-known classification problems for which a feedforward neural network (FNN) can be used is handwritten digit recognition [55]. A widely used dataset for this task is MNIST, which contains 60,000 labeled images of handwritten digits for training. In this application, the pixel values of each image serve as inputs to the FNN, so the input layer must contain the same number of nodes as the number of pixels in an image. The number and size of the hidden layers are chosen to optimize performance, typically measured by classification accuracy. Each training image is labeled with its corresponding digit, which is encoded as a one-hot vector: for example, the digit 0 is represented as

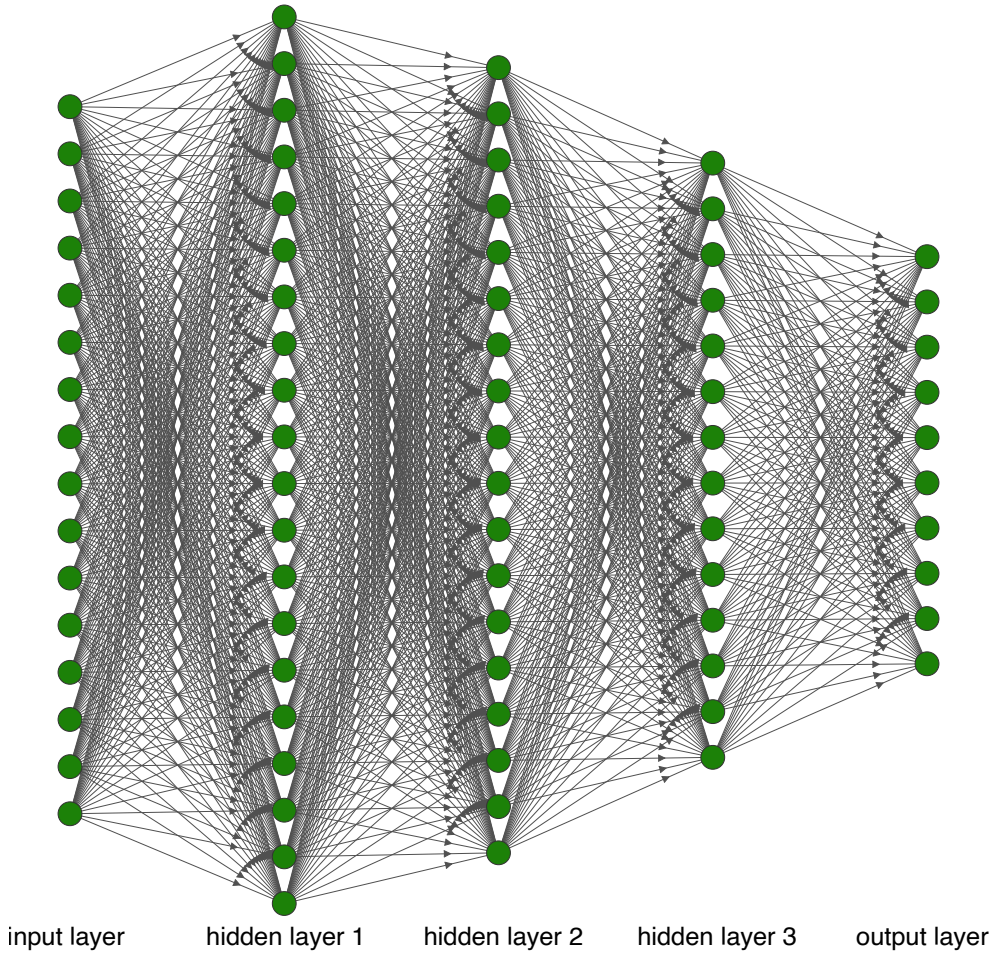


Figure 3.1: . An example of a feedforward neural network. Green circles represent neurons (nodes), and the arrows indicate unidirectional connections from one layer to the next, progressing toward the output layer. Each connection is associated with a weight, and each neuron—except those in the input layer—is assigned a bias. The inputs from the previous layer are linearly combined using these weights and biases, and the result is passed through an activation function (e.g., the sigmoid function in Eq. (3.1)). The weights and biases collectively constitute the trainable parameters of the network, which are optimized to produce a desired output. This example shows three hidden layers, each with an arbitrary number of nodes.

$(1,0,0,0,0,0,0,0,0,0)^T$, the digit 1 as $(0,1,0,0,0,0,0,0,0,0)^T$, and so on. During training, the FNN's output (i.e., the values of the ten output neurons) is compared to the target one-hot vector. The difference between them—referred to as the residual—is used to define a scalar objective function, commonly known as the cost function, loss function, or error function. This function, often taken as the sum of squared differences or its average, is minimized by adjusting the network parameters (weights and biases) through an optimization algorithm.

After the training session concludes—typically involving multiple epochs, where each epoch consists of shuffling and feeding the entire training dataset to the network—the performance of the trained neural network is evaluated using a separate dataset known as the test set, which contains 10,000 images. During this evaluation phase, no cost function minimization or parameter updates are performed. The sole purpose is to evaluate how well the trained FNN generalizes to classifying digits it has not encountered during training. This test accuracy provides a measure of the model's ability to perform on unseen data, which is critical to validating its practical utility.

3.1.2 Cost Function of an NN

The cost function is a scalar function that takes as its argument the output of a neural network. Focusing on the FNN example of digit recognition, a typical cost function can be defined as follows [55]:

$$J_{\text{quad}}(\Theta) = \frac{1}{2n} \sum_{(\mathbf{X}_{\text{tr}}, \mathbf{X}_0)} |F(\mathbf{X}_{\text{tr}}, \Theta) - \mathbf{X}_0|^2, \tag{3.2}$$

where $\mathbf{X}_{\text{tr}}$ denotes the input data (that is, the pixel values of a training image), $\mathbf{X}_0$ is the corresponding target vector that encodes the correct digit label, and n is the total number of training samples. This particular form of the cost, also known as the quadratic or mean square error (MSE) cost, quantifies the average squared difference between the network's output $F(\mathbf{X}_{\text{tr}}, \Theta)$ and the desired output $\mathbf{X}_0$ in the training set. The objective is to find a set of NN parameters Θ that minimizes the cost function in Eq. (3.2).

The minimization of a cost function can be implemented using a gradient descent algorithm. To demonstrate this, we consider a Taylor expansion of the cost function $J(\Theta + \delta\Theta)$, where $\delta\Theta$ denotes an infinitesimal variation in the neural network parameters:

$$J(\Theta + \delta\Theta) \approx J(\Theta) + \delta\Theta^T \nabla_\Theta J(\Theta) + \frac{1}{2!}\delta\Theta^T \nabla_\Theta^2 J(\Theta)\delta\Theta + \dots \tag{3.3}$$

Here, $\nabla_\Theta J(\Theta)$ is the gradient (i.e., the Jacobian of the scalar-valued function J with respect to the vector Θ), and $\nabla_\Theta^2 J(\Theta)$ is the Hessian matrix. Retaining only the first-order term, we approximate the change in the cost function as

$$\delta J = J(\Theta + \delta\Theta) - J(\Theta) \approx \delta\Theta^T \nabla_\Theta J(\Theta). \tag{3.4}$$

To ensure that δJ is negative—i.e., that $J(\Theta)$ decreases—we choose $\delta\Theta = -\eta\nabla_\Theta J(\Theta)$, where $\eta > 0$ is a small scalar. In machine learning, η is known as the learning rate and is treated as a tunable hyperparameter. With this choice, we have

$$\delta J = -\eta |\nabla_\Theta J(\Theta)|^2, \tag{3.5}$$

which is always negative, ensuring descent along the cost function. Therefore, the parameters are updated using the rule $\Theta' = \Theta - \eta\nabla_\Theta J(\Theta)$, which is the essence of the gradient descent algorithm [55].

It should be noted that the second-order term in Eq. (3.3) can be retained to incorporate information about the curvature (i.e., the Hessian) of the cost function. This enables the use of second-order optimization methods that adjust the learning rate according to the local concavity of the cost landscape. However, evaluating the Hessian matrix is computationally expensive, especially for NNs with a large number of parameters. To avoid this cost, more sophisticated variants of the gradient descent algorithm have been developed. These include momentum-based stochastic gradient descent [60], RMSProp [61], and Adam [62]. Such methods introduce additional tunable hyperparameters and adaptively modify the learning rate using running averages of the gradients and, in some cases, their second moments. These techniques accelerate convergence and improve stability, particularly in problems involving noisy or sparse gradients.

3.1.3 Improvements to Learning

Some cost functions can lead to slower learning, such as the quadratic cost function (3.2). This slowdown is often attributed to the vanishing gradient problem, which arises when sigmoid activation functions saturate and produce gradients that are nearly zero [55]. One way to alleviate this issue is to adopt a cost function that mitigates the effect of vanishing gradients caused by saturated sigmoid activations. The cross-entropy cost function, given by

$$J_{\text{cross}}(\Theta) = -\frac{1}{n} \sum_{(\mathbf{X}_{\text{tr}}, \mathbf{X}_0)} \sum_i \left[\mathbf{X}_{0i} \ln \left(F(\mathbf{X}_{\text{tr}}, \Theta)_i \right) + (1 - \mathbf{X}_{0i}) \ln \left(1 - F(\mathbf{X}_{\text{tr}}, \Theta)_i \right) \right], \tag{3.6}$$

has this property, and learning slowdown can be avoided by using it instead of the quadratic cost function $J_{\text{quad}}(\Theta)$ (3.2) [55]. Here, the second summation is over all output nodes in the final layer of the FNN.

The vanishing gradient problem arises when the sigmoid activation function saturates—that is, when the weighted input to the neuron becomes very positive or very negative. In these regions, the derivative of the sigmoid activation

$$\sigma'(u) = \sigma(u) \left[1 - \sigma(u) \right], \tag{3.7}$$

becomes very small. When the quadratic cost function $J_{\text{quad}}(\Theta)$ (3.2) is used in conjunction with the sigmoid activation, the gradient of the cost with respect to a weight in the output layer becomes proportional to

$$\frac{\partial J_{\text{quad}}}{\partial w} \propto \left[F(\mathbf{X}_{\text{tr}}, \Theta)_i - \mathbf{X}_{0i} \right] \cdot \sigma'(u), \tag{3.8}$$

where $F(\mathbf{X}_{\text{tr}}, \Theta)_i = \sigma(u)$ is the ith NN output node and $\mathbf{X}_{0i}$ is the ith component of the target label vector. When $F(\mathbf{X}_{\text{tr}}, \Theta)_i$ approaches 0 or 1, $\sigma'(u) \to 0$, and the gradient vanishes, even if the output is far from the target. This considerably slows the training process.

In contrast, when the cross-entropy cost function $J_{\text{cross}}(\Theta)$ (3.6) is used with a sigmoid activation, the gradient of the cost to a weight in the output layer simplifies to

$$\frac{\partial J_{\text{cross}}}{\partial w} \propto F(\mathbf{X}_{\text{tr}}, \Theta)_i - \mathbf{X}_{0i}, \tag{3.9}$$

which avoids the multiplicative factor $\sigma'(u)$ entirely. Therefore, even when $F(\mathbf{X}_{\text{tr}}, \Theta)_i$ is close to 0 or 1, the gradient remains significant as long as the output differs from the target. This accelerates convergence and avoids learning slowdown due to vanishing gradients. Similar arguments can be made with respect to biases to show slowdown suppression when the cross-entropy cost is used.

Other ways to improve the learning process include techniques aimed at preventing overfitting. The most common among these is regularization, with L2 regularization (also known as weight decay) being widely used. It is implemented by adding a penalty term to the cost function, leading to the modified expression [55]:

$$J_{\text{reg}}(\Theta) = J(\Theta) + \frac{\lambda}{2n} \sum_{w} w^2, \tag{3.10}$$

where the summation is over all the weights in the neural network parameters Θ (excluding biases), and λ is a hyperparameter that controls the strength of the regularization. A larger λ penalizes large weights more heavily, encouraging the network to keep them small.

The weight update rule is modified accordingly:

$$w' = \left(1 - \frac{\eta\lambda}{n}\right) w - \eta \nabla_w J(\Theta), \tag{3.11}$$

while the update rule for biases remains unchanged. Keeping the weights small promotes smoother and more generalizable functions, making the network less sensitive to noise and spurious correlations in the training data. Without regularization, larger weights may cause the network to memorize training data, resulting in poor generalization performance on the test set [55].

Another widely used regularization technique is dropout [161]. Unlike weight decay, which modifies the cost function, dropout alters the structure of the neural network during training. Specifically, at each training iteration, a fixed percentage of neurons in the hidden layers is randomly "dropped out"—i.e., temporarily removed from the network by setting their output to zero. The forward and backward passes are then performed on this thinned network.

This process is repeated at every training step with a new random subset of neurons dropped. As a result, the network effectively trains an ensemble of smaller subnetworks

that share weights. Once training is complete, all neurons are reinstated and their outputs are appropriately scaled (typically by multiplying by the dropout rate) to approximate the average prediction of the ensemble.

This technique significantly reduces overfitting by preventing neurons from co-adapting too strongly and encourages the network to learn more robust and distributed representations [55].

3.1.4 Stochastic Gradient Descent

So far, when we have referred to training an NN or the learning of network parameters, we have essentially meant the optimization of the weights and biases such that the cost function is minimized in the high-dimensional parameter space. One straightforward approach to this optimization is to use the entire training dataset at each iteration to compute the cost function and its gradient; this method is known as batch gradient descent. However, although conceptually simple, batch gradient descent is computationally inefficient for large datasets, as it requires a complete pass through all training samples before each parameter update.

Stochastic gradient descent (SGD) is a variation of the gradient descent algorithm that significantly accelerates the learning process by dividing the training set into smaller chunks, commonly known as mini-batches [55]. To update the NN parameters, one must compute the gradient of the cost function with respect to those parameters, denoted by $\nabla_\Theta J(\Theta)$. For the quadratic cost function (3.2), the gradient can be expressed as:

$$\nabla_\Theta J_{\text{quad}}(\Theta) = \frac{1}{n} \sum_{\mathbf{X}_{\text{tr}}} \nabla_\Theta J_{\mathbf{X}_{\text{tr}}}(\Theta), \tag{3.12}$$

where $J_{\mathbf{X}_{\text{tr}}}(\Theta) = \left| F(\mathbf{X}_{\text{tr}}, \Theta) - \mathbf{X}_0 \right|^2 / 2$ denotes the cost associated with a single training sample. This formulation shows that the full gradient is the average over all training samples. However, for large datasets, computing this sum in every iteration becomes computationally expensive.

The SGD approach approximates this average by using a randomly selected mini-batch of the training data (typically without replacement), which is substantially smaller than the full dataset. That is,

$$\nabla_\Theta J_{\text{quad}}(\Theta) \approx \frac{1}{m} \sum_{X_m} \nabla_\Theta J_{X_m}(\Theta), \tag{3.13}$$

where X_m denotes a mini-batch with m entries. This approximation leads to an updated rule for the NN parameters:

$$\Theta' = \Theta - \frac{\eta}{m} \sum_{X_m} \nabla_\Theta J_{X_m}(\Theta). \tag{3.14}$$

Using this approach, each parameter update becomes computationally cheaper, enabling faster iterations and often better generalization in practice.

The update rule for training an NN can, in principle, be applied by computing the cost function over the entire training set. However, in practice, such as in the case of handwritten digit recognition, training with mini-batches significantly accelerates the learning process. This is implemented by selecting a subset (mini-batch) of the training data and updating the NN parameters using the rule $\Theta' = \Theta - \eta \nabla_\Theta J(\Theta)$. These updates are repeated until all mini-batches have been used, which constitutes one epoch of training.

This approach results in multiple parameter updates per epoch, in contrast to just one update when using the full training set. As a result, learning progresses more rapidly. The key insight here is that the gradient used in the update rule does not need to be exact; rather, an approximate gradient that generally points in the direction of the steepest descent is sufficient to guide the network toward a minimum of the cost function [55]. Thus, SGD enhances the efficiency of the learning process by reducing the number of epochs required to achieve convergence.

So far, we have seen that regardless of the algorithm employed for cost minimization, the gradient $\nabla_\Theta J(\Theta)$ must be computed to update the NN parameters. The algorithm responsible for calculating this gradient is the backpropagation algorithm, which we discuss next.

3.1.5 Backpropagation Algorithm

To update the NN parameters using the rules discussed earlier, it is necessary to compute the gradient of the cost function, $\nabla_\Theta J(\Theta)$. This computation is performed using the backpropagation algorithm, whose core mechanism is the application of the chain rule from calculus. The systematic use of this algorithm for learning the parameters of NNs was first thoroughly studied in the seminal work by Rumelhart et al. [162].

In general, two distinct passes over a neural network (assumed here to be a feedforward neural network, or FNN, for simplicity) are required to update the parameters Θ. During the forward pass, inputs from the training set are fed into the input nodes and propagated through the network—via application of the weights, biases, and activation functions—culminating in the output layer, where the cost is computed based on the predicted outputs. In the backward pass, the derivatives of the cost function with respect to the network parameters (i.e., weights and biases) are calculated. This involves starting at the output layer and determining how infinitesimal changes in the weights and biases affect the cost function, using the chain rule of calculus. These gradients are then "backpropagated" through the network, layer by layer, toward the input layer. Taken together, the forward and backward passes comprise the full backpropagation algorithm for computing the gradients necessary for parameter updates.

Denoting the activation functions by f, their inputs by $\mathbf{z}$, and their outputs by $\mathbf{a}$ (i.e., $\mathbf{a}$=f($\mathbf{z}$)), the weight matrices between layers by $\mathbf{W}$ (since in a fully connected NN, the weights between consecutive layers can be represented as matrices), and the bias vectors by $\mathbf{b}$, the backpropagation algorithm can be expressed through the following four main equations [55]:

$$\boldsymbol{\delta}_{ll} = \nabla_{\mathbf{a}} J \odot f'(\mathbf{z}_{ll}), \tag{3.15}$$

$$\boldsymbol{\delta}_{l} = ((\mathbf{W}^{l+1})^T \boldsymbol{\delta}_{l+1}) \odot f'(\mathbf{z}_{l}), \tag{3.16}$$

$$\nabla_{\mathbf{b}} J = \boldsymbol{\delta}_{l}, \tag{3.17}$$

$$\nabla_{\mathbf{W}} J = \mathbf{a}_{l-1} \otimes \boldsymbol{\delta}_{l}, \tag{3.18}$$

where ll denotes the last layer, and all preceding layers are indexed by l. The symbol $\odot$ denotes the element-wise (Hadamard) product, and $\otimes$ denotes the outer product. The

vectors $\boldsymbol{\delta}_l$ represent the sensitivities or error signals, quantifying how the values at each node change due to infinitesimal perturbations in their inputs. These expressions are direct applications of the chain rule of calculus [55]. Note that f' denotes the derivative of the activation function with respect to its input, and we have omitted the explicit dependence of the cost function $J(\mathbf{W}, \mathbf{b})$ on the weights and biases for brevity.

These expressions provide a practical way to calculate the gradients for the weights and biases of the NN, which, in turn, are used to implement parameter updates using a gradient descent method. They can be readily translated into computer code; however, in practice, the backpropagation algorithm is commonly implemented using well-established machine learning libraries. For example, the PyTorch library [163] provides built-in methods for computing gradients via backpropagation, which can be easily applied to a predefined NN using simple function calls.

To perform the backpropagation algorithm, the library framework constructs computational graphs [56] that track the variables and operations involved. In PyTorch [163], these are referred to as "directed acyclic graphs" where the nodes represent operations and the edges represent the flow of data between them. During the forward pass, this computational graph is dynamically built by recording all operations performed on the inputs of the NN, and it is stored in memory. Variables intended for differentiation are flagged with `grad=True`, signaling the framework to include them in the graph. When the backpropagation algorithm is invoked, the graph is traversed in reverse to compute the gradients of the NN parameters (weights and biases).

It should be noted that the same automatic differentiation engine used to construct computational graphs and implement the backpropagation algorithm can also be employed to compute derivatives with respect to any variable in the NN. For instance, if derivatives of the NN output with respect to the input variables are required, the input nodes can be flagged as `grad=True` variables. A computational graph is then constructed to record all operations involving these inputs. Derivatives of the output are subsequently obtained by invoking the `autograd` function. The order of differentiation is limited primarily by the available memory, rather than algorithmic constraints. When graphics processing units (GPUs) are used, these computations can be efficiently parallelized, although the available GPU memory sets the upper bound on the number of data points processed simultaneously.

Importantly, the derivatives obtained via automatic differentiation are exact up to machine precision (assuming the NN has sufficient depth and width), in contrast to those computed using finite-difference methods, which are subject to discretization error.

3.2 Neural Network for Vesicle Shapes

Here, we focus on the neural network architecture employed in our proposed vesicle shape solver. The core of the solver is an FNN that represents a phase field characterizing the three-dimensional shape of a vesicle. The input layer receives the Cartesian coordinates of the simulation domain that encloses the vesicle, while the single output node returns the value of the phase field at each input coordinate. We demonstrate how this FNN architecture can be utilized to obtain solutions to a constrained energy minimization problem, analogous to Eq. (2.5), by encoding the constraints and energy terms into a suitably defined cost function.

3.2.1 NN Representation of a Scalar Phase Field

The structure of the NN that represents the vesicle phase field is illustrated in Fig.3.2. As discussed earlier, this is an FNN, which means that the data flow is unidirectional, from the input layer toward the output layer. The input to the network is the spatial coordinates of a point in three dimensions, denoted by $\mathbf{r} := (x, y, z)$, within the simulation box. The activation functions used to introduce nonlinearity in the first and second hidden layers are standard sigmoid functions, given by Eq.(3.1). The output node, which evaluates the phase field ϕ, uses a hyperbolic tangent activation function. This function is related to the sigmoid function by a simple transformation: $\tanh(u) = 2\sigma(u) - 1$, and maps its input to the range $[-1, 1]$. To determine the appropriate depth and width of the network, that is, the number of hidden layers and the number of nodes in each layer, we follow the lower bound estimates for these hyperparameters provided in Ref. [160], which are discussed in more detail in Section4.2.2.

The numerical value of the jth node is obtained by scaling and shifting the output of

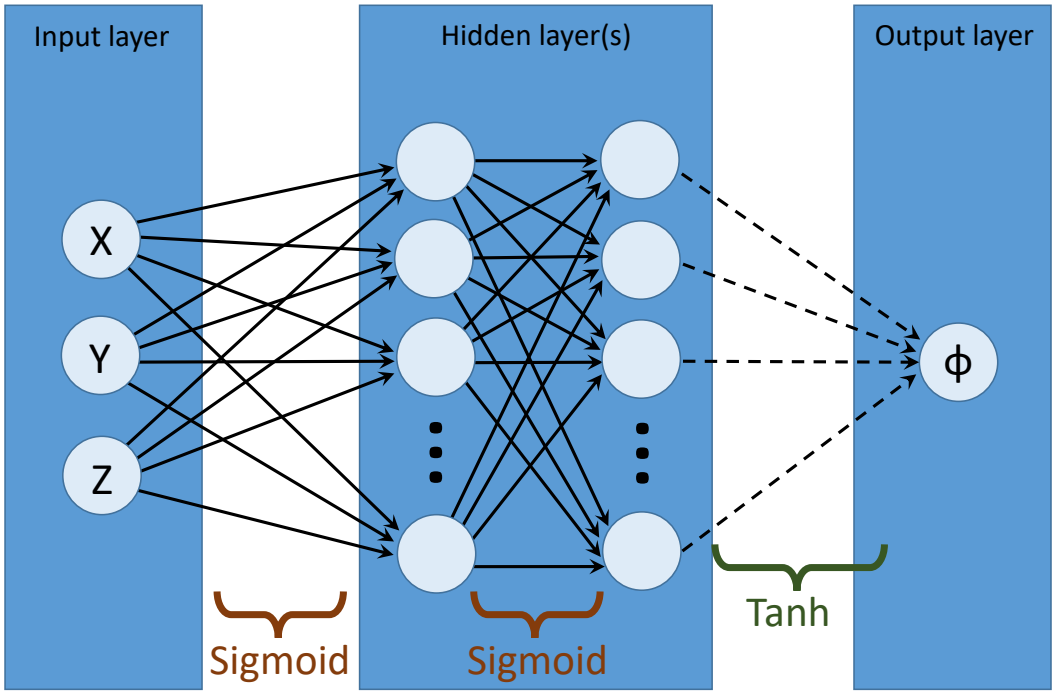


Figure 3.2: Neural network representation of the phase field ϕ. The network consists of two hidden layers, each containing an arbitrary number of hidden nodes. The input layer takes the spatial coordinates, and the output layer returns the value of the phase field ϕ at the corresponding point. Nonlinear activation functions are applied to each hidden node to enable the network to approximate complex spatial variations in ϕ. These activation functions are indicated alongside the respective layers.

the ith node from the previous layer using the NN weights and biases—collectively denoted by Θ—and applying the activation function. This is given by $u'_j = f\left(\sum_i w_{ji}u_i + b_j\right)$, where f denotes the activation function. Consequently, the phase field represented by NN is a function of the spatial coordinates and the NN parameters, written as $\phi(\mathbf{r};\Theta)$. If the NN parameters are grouped into three subsets, Θ_1, Θ_2, and Θ_3, corresponding to three layers, and assuming that all activation functions are hyperbolic tangent functions (with the rescaling and shift absorbed into Θ), the composition can be expressed as

$$\phi(\mathbf{r};\Theta) := \tanh(\tanh(\tanh(\mathbf{r};\Theta_1);\Theta_2);\Theta_3) \tag{3.19}$$

3.2.2 Cost Function for Phase Field NN

To obtain a vesicle shape that minimizes the bending energy subject to surface area and volume constraints, we aim to solve the variational problem given by Eq. (2.5). To this end, we reformulate the problem as the minimization of a cost function defined over the phase-field NN. As discussed earlier, minimizing this cost function yields the optimal set of NN parameters that define the phase-field solution corresponding to the constrained bending energy minimization problem.

The functional expressions for the bending energy, surface area and volume of a vesicle, formulated in terms of a phase field, are provided in the next chapter (see Eqs.(4.1), (4.3), and (4.4)). These expressions can be rewritten in terms of the NN-represented phase field and its spatial derivatives as $E_b[\phi(\mathbf{r};\Theta), \nabla^2\phi(\mathbf{r};\Theta)]$, $A[\phi(\mathbf{r};\Theta), \nabla\phi(\mathbf{r};\Theta)]$, and $V[\phi(\mathbf{r};\Theta)]$. A suitable cost function that incorporates these expressions and enforces the desired geometric constraints is given by

$$J(\Theta) = E_b(\Theta) + \lambda_A[A(\Theta) - A_0] + \lambda_V[V(\Theta) - V_0], \tag{3.20}$$

where the dependence on $\mathbf{r}$ is suppressed, as the integrals in (4.1), (4.3), and (4.4) yield scalar quantities. Here, λ_A and λ_V are Lagrange multipliers that impose the surface area and volume constraints, and A_0 and V_0 are the prescribed target values for the surface area and volume of the vesicle, respectively.

Minimizing the cost function in Eq.(3.20) requires calculating its gradient with respect to the NN parameters Θ, which is performed in practice using the backpropagation algorithm. To update the parameters according to the rule $\Theta' = \Theta - \eta\nabla_\Theta J(\Theta)$ after each training epoch, the gradient $\nabla_\Theta J(\Theta)$ must be computed. For the cost function given in (3.20), the gradient takes the form

$$\nabla_\Theta J(\Theta) = \nabla_\Theta E_b(\Theta) + \lambda_A\nabla_\Theta A(\Theta) + \lambda_V\nabla_\Theta V(\Theta). \tag{3.21}$$

When this cost reaches its minimum with respect to the NN parameters, $\nabla_\Theta J(\Theta) = 0$, which provides the optimal set of parameters Θ^* that yield the phase field solution minimizing the bending energy under the prescribed constraints. In other words, we have

$$\nabla_\Theta E_b(\Theta) + \lambda_A\nabla_\Theta A(\Theta) + \lambda_V\nabla_\Theta V(\Theta) = 0, \tag{3.22}$$

which resembles the structure of the variational problem given in (2.5), except that the functional derivatives $\delta/\delta\phi$ are replaced here by gradients with respect to the NN parameters. In this formulation, the NN solver explores the multidimensional parameter space to minimize the cost function, while the Lagrange multipliers are concurrently updated using a gradient ascent scheme. As a result, the critical points of $J(\Theta)$ identified by this approach correspond to saddle points in the joint space of NN parameters and Lagrange multipliers.

We note that, under the NN representation (3.19), the spatial derivatives of the phase field ($\nabla\phi$ and $\nabla^2\phi$), as well as the parameter gradient $\nabla_\Theta\phi(\mathbf{r};\Theta)$ involve powers of the factor $(1-\tanh^2(u))$. When the NN solver is initialized with a set of parameters Θ that produces a rough morphology resembling vesicle shapes, where $\phi=-1$ at the boundaries of the simulation box, this factor, which becomes $(1-\phi^2)$ in the output layer, acts to preserve these boundary conditions throughout the cost minimization process.

Furthermore, the spatial derivatives of the phase field can be interpreted as outputs of separate NNs. In practice, when automatic differentiation in the PyTorch library is invoked to compute these derivatives, the chain rule is applied through the computational graph from the output node back to the input nodes. These intermediate computations are cached in memory and subsequently used to construct the computational graph for the cost function. This graph is then employed to evaluate $\nabla_\Theta J(\Theta)$, which is needed to update the NN parameters.

In the next chapter, this NN solver is deployed to numerically solve the phase-field-formulated Helfrich model. Both axisymmetric and non-axisymmetric vesicle shapes are computed and illustrated. Furthermore, we provide further details on the numerical implementation of the cost function and the optimization process, including the use of a more advanced gradient-based method, namely the Adam algorithm [62].

Chapter 4

Neural Network Solver for 3D Membranes

The content of this chapter overlaps with the text in reference [164].

4.1 Introduction

Recent progress in developing machine learning methods for studying physical systems has opened the door to new approaches that were not possible a decade ago. A well-known capability of machine learning is its ability to analyze large volumes of condensed matter data, aiding in the discovery of previously unrecognized physical properties. More directly, an artificial neural network can be incorporated into a physical model, enabling quantitative analysis where conventional mathematical and computational physics methods encounter difficulties. One such difficulty in soft matter physics is calculating non-axisymmetric membrane conformations under various physical conditions, based on the fundamental theoretical model proposed by Helfrich half a century ago [27]. Here, we demonstrate that this challenge can be addressed by utilizing a neural-network representation of membrane morphology.

The importance of modeling fluid membranes made of lipid bilayers for studying biolog-

ical and soft-matter systems has been well recognized [6]. In a coarse-grained version, such membranes are typically described as deformable elastic surfaces, where the energy cost of bending a surface element is locally described by the squared mean and Gaussian curvatures [27, 29]. Thus, developing an adaptable, robust, and reliable numerical framework for calculating the full three-dimensional (3D) shapes of membranes becomes a fundamental task. Axisymmetric systems significantly reduce the complexity of the problem, and many theoretical tools have been developed over the years to handle these calculations [96, 30, 73, 32, 165, 112, 113, 114].

Recognizing the computational challenges of representing a 3D deformable surface directly, an active research area in applied mathematics is the characterization of such a surface by a phase field $\phi(\mathbf{r})$, where the 3D variation of the function is assumed. This function takes constant values (e.g., ± 1) far from the membrane surface and varies between these values to represent the 3D profile of the membrane. The Helfrich energy is then rewritten in terms of a functional $E_b[\phi(\mathbf{r}), \nabla\phi(\mathbf{r})]$, the minimization of which, to produce the membrane profile, is usually performed by solving the resulting Euler-Lagrange equation using finite-difference or finite element analysis [45, 46, 48]. This approach requires no initial specification of a surface in 3D space and can capture non-axisymmetric shapes.

Here, we propose the representation of the phase field by a neural network (NN). Instead of directly calculating $\phi(\mathbf{r})$, the Helfrich energy is minimized with respect to the NN parameters by implementing recent machine learning optimization methods. The spatial dependence of the shape function $\phi(\mathbf{r})$ and its gradient are both handled analytically, avoiding the potential pitfalls of finite-difference representation of derivatives. Any required spatial sampling is carried out separately from the NN parameterization. We first recover the axisymmetric calculation of vesicle shapes in free space, followed by the presentation of non-axisymmetric conformations when vesicles are either in free space or confined in finite space.

4.2 Model

Using the concept of a deformable, closed surface, the Helfrich model is expressed in terms of the bending energy 2.2 [27], namely

$$E_b = 2\kappa \int_S (H - H_0)^2 \, \mathrm{d}S + \kappa_G \int_S K \mathrm{d}S,$$

where κ and κ_G are the bending and Gaussian moduli, respectively. The surface element $\mathrm{d}S$ has a local mean curvature H, a spontaneous curvature H_0, and Gaussian curvature K. In this work, we consider the case where $H_0 = 0$, and vesicles maintain the same Euler characteristic, for which the second term is a constant and can be removed.

In the phase-field description, the entire vesicle morphology is represented by a continuous $\phi(\mathbf{r})$, which takes the values $+1$ and -1 in the interior and exterior regions, sufficiently far from the phase-field interface. A significant variation in $\phi(\mathbf{r})$ occurs over the membrane surface area between the interior and exterior, with thickness characterized by ϵ. It can be shown that the first term in the Helfrich energy (with $H_0 = 0$) is equivalently expressed as [45]

$$E_b[\phi] = \frac{3\kappa}{4\sqrt{2}\epsilon} \int \mathrm{d}\mathbf{r} \left[\epsilon \nabla^2 \phi(\mathbf{r}) + \frac{1}{\epsilon} \phi(\mathbf{r})[1 - \phi(\mathbf{r})^2] \right]^2 . \tag{4.1}$$

To calculate the vesicle shape, the above functional must be minimized with respect to $\phi(\mathbf{r})$, subject to constraints that account for other physical conditions. Due to the finite number of lipid molecules making up the vesicle surface, the surface area is conserved as A_0, and for an impermeable vesicle, the enclosed volume is also constant, denoted as V_0. Hence,

$$A[\phi] = A_0, \quad V[\phi] = V_0, \tag{4.2}$$

where

$$A[\phi] = \frac{3}{4\sqrt{2}} \int \mathrm{d}\mathbf{r} \left[\epsilon |\nabla \phi(\mathbf{r})|^2 + \frac{1}{2\epsilon} [1 - \phi(\mathbf{r})^2]^2 \right], \tag{4.3}$$

$$V[\phi] = \frac{1}{2} \int \mathrm{d}\mathbf{r} [1 + \phi(\mathbf{r})], \tag{4.4}$$

according to the phase-field model (see Appendix A, Phase-field Formulation of Helfrich Model).

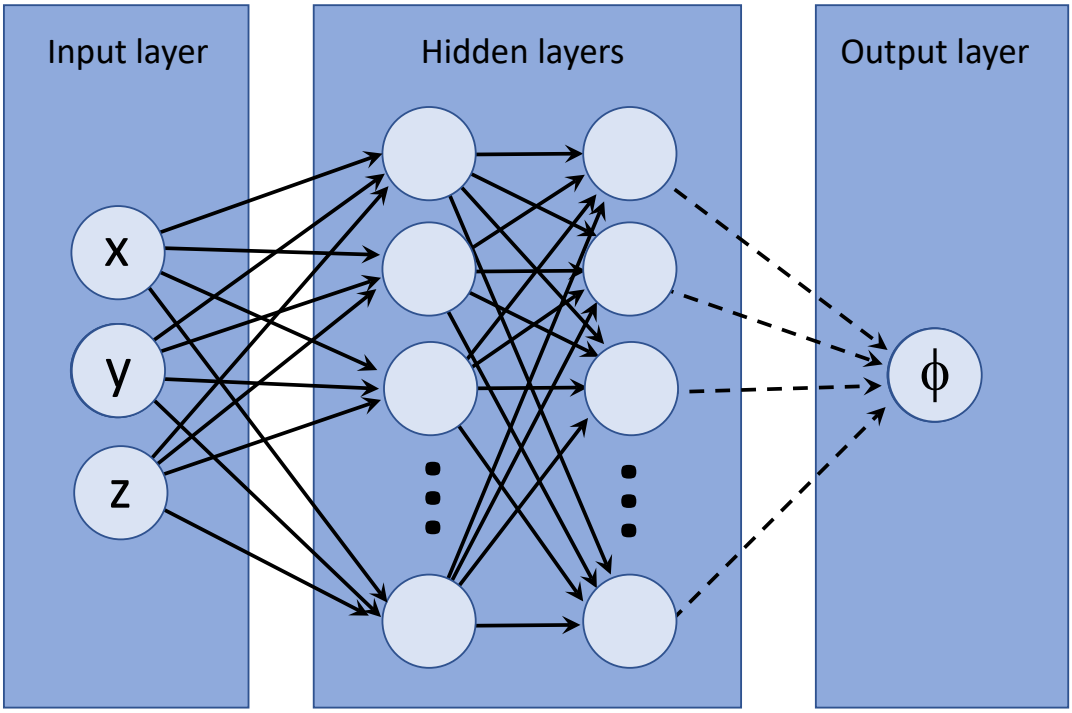


Figure 4.1: NN representation of $\phi(\mathbf{r})$. Solid arrows leading to a node indicate the use of the sigmoid function, while dashed arrows indicate the tanh function. Two hidden layers, with 20 and 10 nodes respectively, are used in the computation.

4.2.1 NN Representation of Phase-field

Here, the phase field is represented by a simple NN, as shown in Fig. 4.1. The value of the jth node in a hidden layer, z'_j, is calculated from all the nodes in the previous layer by $z'_j = f\left(\sum_i w_{ji} z_i + b_j\right)$, where w_{ji} and b_j are network parameters, known as weights and biases, and $f(u)$ is the activation function. For the hidden layers, $f(u)$ takes the form of the sigmoid function $\sigma(u) = [1 + \exp(-u)]^{-1}$. The final output, the scalar ϕ, is calculated similarly, but using the hyperbolic tangent, $f(u) = \tanh(u)$, to produce a value between -1 and 1. Using Θ as the abbreviation for the entire set of weights and biases, the NN representation yields $\phi(\mathbf{r}; \Theta)$, where $\mathbf{r} = (x, y, z)$ is the input spatial location.

4.2.2 Selection of the Number of Parameters and Hidden Layers

It is known that a neural network (NN) is an efficient way to represent a continuous function with arbitrary accuracy, provided that a sufficient number of neurons is placed in the hidden layer [57, 58, 59]. More specifically, it has been shown that a feedforward NN with a single two-neuron hidden layer and sigmoidal activation can approximate any continuous univariate function on a compact subset of real numbers to arbitrary accuracy [159]. This concept has been extended to multivariate functions, where at least two hidden layers are required [166]. Furthermore, Ref. [160] shows that by including at least $3d + 2$ hidden neurons (where d denotes the number of input dimensions/neurons) in a two-hidden-layer NN with sigmoidal activation, any multivariate continuous function can be approximated to arbitrary accuracy. In the present case, an NN with 30 hidden neurons and sigmoidal activation functions is sufficiently complex to approximate phase fields that represent a variety of shapes, including non-axisymmetric configurations.

4.2.3 Numerical Minimization of the Cost Function

In numerical implementation, all integrals needed for calculating (4.1), (4.3), and (4.4) are expressed as

$$G(\Theta) = \int \mathrm{d}\mathbf{r} g[\phi(\mathbf{r};\Theta)] = \frac{V_D}{S}\sum_{k=1}^{S} g[\phi(\mathbf{r}_k;\Theta)], \tag{4.5}$$

where S uniformly spaced sampling points are adopted in the sampling space of volume V_D. This allows for a simple algebraic average, although more sophisticated sampling techniques aimed at improving integration precision can also be used. The original minimization problem is then converted into the consideration of a cost function [167]

$$J = E_b(\Theta) + \lambda_A[A(\Theta) - A_0] + \lambda_V[V(\Theta) - V_0] + P(\Theta), \tag{4.6}$$

where λ_A and λ_V are Lagrange multipliers used to enforce the surface area and volume constraints, and $P(\Theta)$ denotes other types of constraints to be specified below. Both ∇-operators in (4.1) and (4.3) are handled using the analytic differentiation capability (also

known as automatic differentiation) of the software package designed for NN implementation, which in this study is the PyTorch library [163]. No finite-difference or finite element approximations are used to compute the derivatives.

The goal is to minimize J with respect to all NN parameters Θ and maximize J with respect to λ_A and λ_V. These computational tasks can be efficiently tackled by streamlined machine learning methods. The principal method for minimizing the cost function J with respect to the network parameters Θ is the steepest descent,

$$\Theta \leftarrow \Theta - \eta \nabla_\Theta J, \tag{4.7}$$

where the step size η, also known as the learning rate, is used. The derivatives $\nabla_\Theta J$ are computed using the backpropagation algorithm [162]. In Adam optimization, parameter updates involve the first and second moments of $\nabla_\Theta J$, with exponential moving averages of these moments calculated at each epoch. The learning rate η is adjusted by hyperparameters that control the exponential decay rates [62].

The Lagrange multipliers are updated by the steepest ascent, which in the case of the volume and surface area constraints read

$$\lambda_V \leftarrow \lambda_V + \gamma[V(\Theta) - V_0], \quad \lambda_A \leftarrow \lambda_A + \gamma[A(\Theta) - A_0], \tag{4.8}$$

with the step size γ. These update rules for the network parameters and Lagrange multipliers effectively search for a saddle point in the multidimensional space that defines the cost function J.

For the network parameter updates, the learning rate is set to $\eta = 0.001$, which is the initial rate in the Adam algorithm. Moreover, the Lagrange multipliers are updated with a step size of $\gamma = 0.01$. Both η and γ were determined through a few trial runs of NN training (optimization).

4.3 Results

We first demonstrate that the free-vesicle shapes calculated here agree with known results for both axisymmetric and non-axisymmetric shapes. Later we present results for the confinement of the vesicles in different types of hard-wall confinements.

To keep the vesicle near the center of the calculation box, a constraint function $P(\Theta) = B|\mathbf{R}(\Theta)|$ is used, where

$$\mathbf{R}(\Theta) = \frac{1}{2}\int \mathrm{d}\mathbf{r}[1 + \phi(\mathbf{r};\Theta)]\mathbf{r}, \tag{4.9}$$

is the center-of-mass coordinate, and B is a numerical coefficient initialized to a positive value, e.g., one. Instead of initializing the NN with a random vector Θ, a set of Θ known to roughly produce the correct morphology is used as the initial condition for the network parameters. These initial Θ are adopted from an existing solution (though different physical conditions) or adjusted to force the production of a desired morphology type.

More precisely, our proposed NN solver requires a rough estimate of the initial shape as a starting point for optimization (training). This places the minimization trajectory in the basin of attraction for a specific minimum-energy morphology within the entire energy landscape. By changing the value of the reduced volume $\bar{u}$ (achieved by adjusting constraints on volume or surface area) and/or the area difference Δa (see the area difference model in 2.5.2), other shapes related to the specific morphology can be obtained sequentially. In other words, with a single initial guess for a specific shape, the entire branch of similar shapes can be calculated, unless the NN follows a different branch of shapes due to a phase transition. We observed this latter behavior in the form of a jump (phase transition) from a stomatocyte to an oblate when $\bar{u} \geq 0.7$, and also when the vesicles are placed inside hard-wall confinements.

In the results presented below, all length dimensions in the physical quantities are implicitly scaled by the basic unit $R_0 = (A_0/4\pi)^{1/2}$. Under this assumption, two dimensionless measures are the reduced volume $\bar{u} = 3V/4\pi R_0^3$ and interface width $\bar{\epsilon} = \epsilon/R_0$. The 3D calculation box is centered around the origin, with its sides covering ranges as small as $[-0.7, 0.7]$ to as large as $[-3.0, 3.0]$, determined by a few trial runs to estimate the spatial size and orientation of the converged shape.

4.3.1 Convergence Criteria

The convergence of the NN representation of $\phi(\mathbf{r})$ can be measured by J in (4.6) as a function of the minimization epoch. This is typically achieved within 10^5 epochs. More

specifically, the convergence of the machine learning minimization depends on the initial guess for the set Θ. To illustrate the process, an example is provided below for calculating a prolate shape at $\bar{u} = 0.70$, by giving the NN an initial set of Θ that was already calculated for the case $\bar{u} = 0.95$. The number of training epochs required to achieve convergence is estimated by examining the plots for the cost J and/or bending energy E_b as a function of epoch number. Figure 4.2 demonstrates the convergence curve for these quantities (reduced by $8\pi\kappa$) as the calculation proceeds. Around 5×10^4 epochs, a good level of convergence is reached, with the variation in the reduced values of J and E_b being approximately 10^{-4} between consecutive epochs.

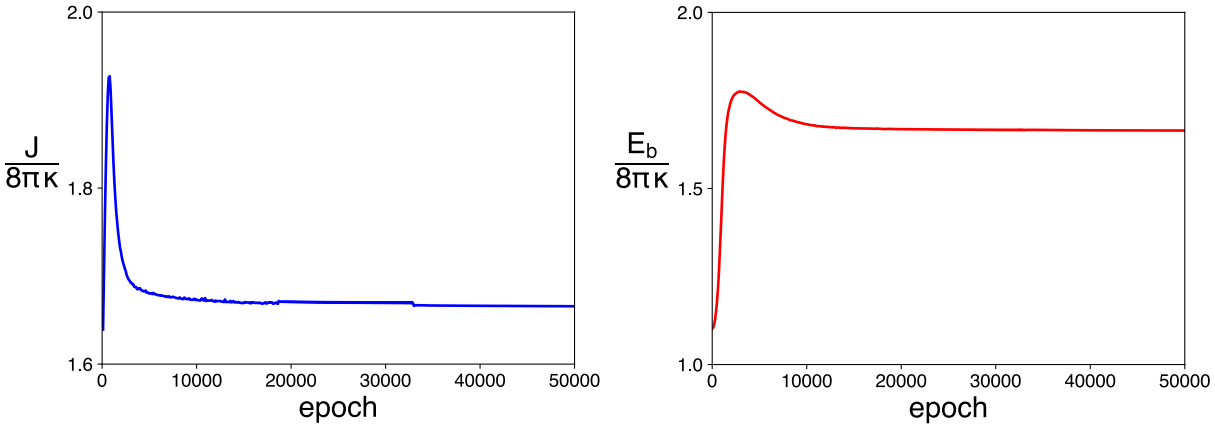


Figure 4.2: Cost function J and bending energy E_b as functions of calculation steps (epochs) for a prolate with $\bar{u} = 0.70$. In each epoch, the network parameters are optimized by the Adam algorithm.

4.3.2 Initial Θ for Axisymmetric Shapes

The following methods were used to obtain the NN parameters Θ for the initial guesses of the shapes. For prolate configurations, we began the optimization from a sphere. To this end, we fit the NN, with a randomly generated set of Θ, to the sphere equation using the mean squared error cost function. As the value of $\bar{u}$ is reduced, the shape becomes more elongated. The mean squared error function is given by

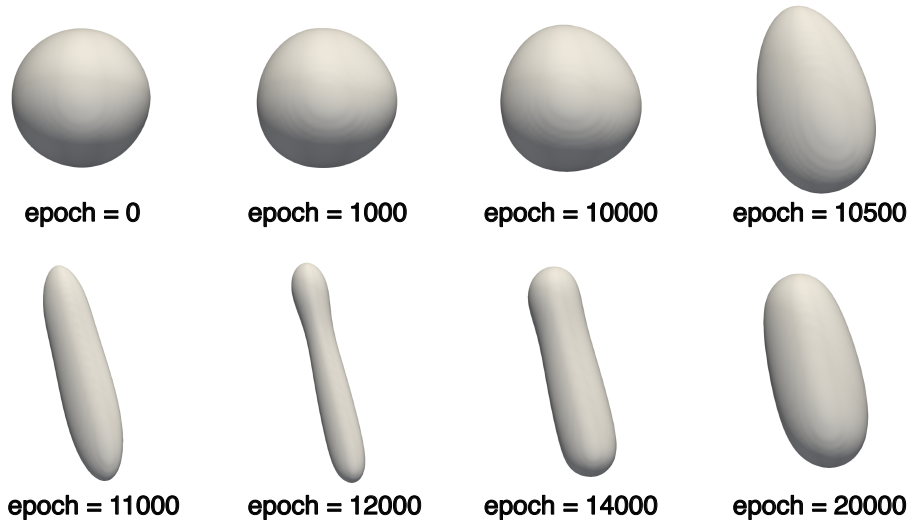


Figure 4.3: Snapshots starting from a sphere as initial guess to obtain prolate $\bar{u} = 0.9$. Epoch numbers for each snapshot are shown under each shape. Eq. (4.10) with (4.11) as target phase field are used to obtain the sphere at epoch=0.

$$MSE(\Theta) = \frac{1}{S}\sum_{k=1}^{S}[\phi(\mathbf{r}_k;\Theta) - \phi_{\text{target}}(\mathbf{r}_k)]^2, \tag{4.10}$$

where $\phi_{\text{target}}(\mathbf{r}_k)$ represents the target values of the phase field for the sphere, namely,

$$\begin{cases} \phi_{\text{target}}(\mathbf{r}_k) = 1, & \text{if } |\mathbf{r}_k|^2 \leq 1, \\ \phi_{\text{target}}(\mathbf{r}_k) = -1, & \text{if } |\mathbf{r}_k|^2 > 1, \end{cases} \tag{4.11}$$

with $|\mathbf{r}_k|^2 = x_k^2 + y_k^2 + z_k^2$. Here, x_k^2, y_k^2, and z_k^2 are the coordinates of S uniformly spaced sampling points. Figure 4.3 shows the progression of the shapes from spherical initial guess to the final conformation with $\bar{u} = 0.9$, which are obtained by minimizing the cost function (4.6). The initial sphere at epoch $= 0$ is the result of a fit using (4.10) and (4.11), which itself takes around 5000 epochs to obtain.

In Fig. 4.4, we decrease the volume of the shape to achieve $\bar{u} = 0.8$. The initial guess is the prolate with $\bar{u} = 0.9$ that is shown at epoch $= 20000$ in Fig. 4.3. After ten thousand epochs, the NN solver converges to a prolate shape with $\bar{u} = 0.8$.

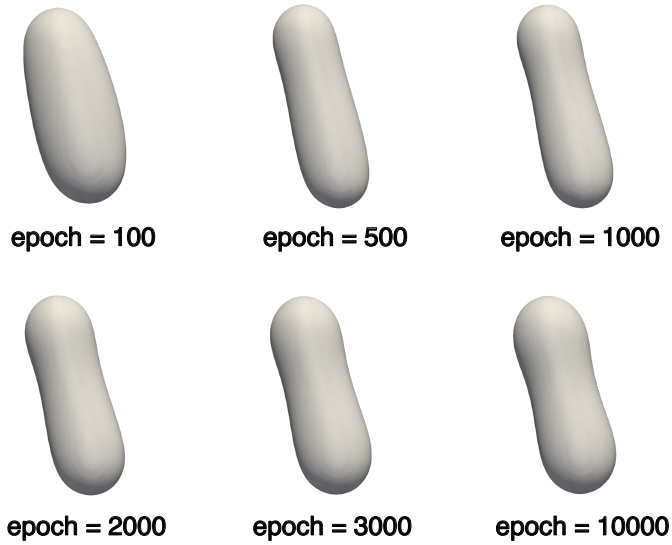


Figure 4.4: Snapshots of evolution of shapes starting from a prolate $\bar{u} = 0.9$ to obtain a prolate $\bar{u} = 0.8$.

If we use the $\bar{u} = 0.8$ prolate from epoch $= 10000$ of Fig. 4.4, and reduce the volume to achieve a reduced volume of $\bar{u} = 0.7$, we obtain the series of shapes in Fig. 4.5, where the last shape is the converged prolate $\bar{u} = 0.7$.

For oblate shapes, the sphere is squeezed at the poles by including an auxiliary penalty term that is removed when the actual optimization is performed. This term penalizes dispersion along the z-axis, i.e.,

$$P_z(\Theta) = \frac{1}{2} \int \mathrm{d}\mathbf{r}[1 + \phi(\mathbf{r})]z^2, \tag{4.12}$$

multiplied by a sufficiently large penalty coefficient (~ 100), producing the desired, approximate shape within a few thousand epochs. The first row of shapes in Fig. 4.6 demonstrate the result of including (4.12) in the cost (4.6). After 5000 epochs this term is removed from (4.6) and the training (minimization) is continued with setting $\bar{u} = 0.55$. At around a total of 45000 epochs the oblate vesicle converges with the progression of shapes shown in the bottom row of Fig. 4.6.

For stomatocytes, a hole is introduced on the side of the sphere, reaching toward and

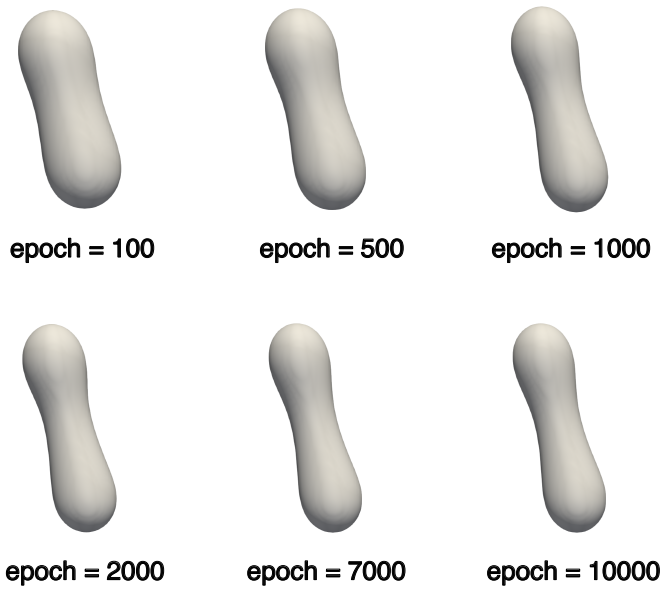


Figure 4.5: Snapshots of evolution of shapes starting from a prolate $\bar{u} = 0.8$ to obtain a prolate $\bar{u} = 0.7$.

beyond the center. This is accomplished by a mean squared error fit that is governed by (4.10), where the value of the phase field is driven to -1 inside the hole. The hole can be spherical or even rectangular, but must be large enough so that the cross section of the starting shape resembles the letter **C**, albeit with a narrower opening and a thicker outline. Similarly to the case of prolate and oblate shapes, this fitting process takes about 5000 epochs. After the initial data are obtained, the stomatocyte shape is resolved using the original cost (4.6) for a certain value of $\bar{u}$. In Fig. 4.7, the convergence of a stomatocyte shape from the initial data at the zeroth epoch to the final shape with $\bar{u} = 0.55$ is illustrated. By epoch 50000 the shape is mostly resolved and there is not much change in its general morphology after this point.

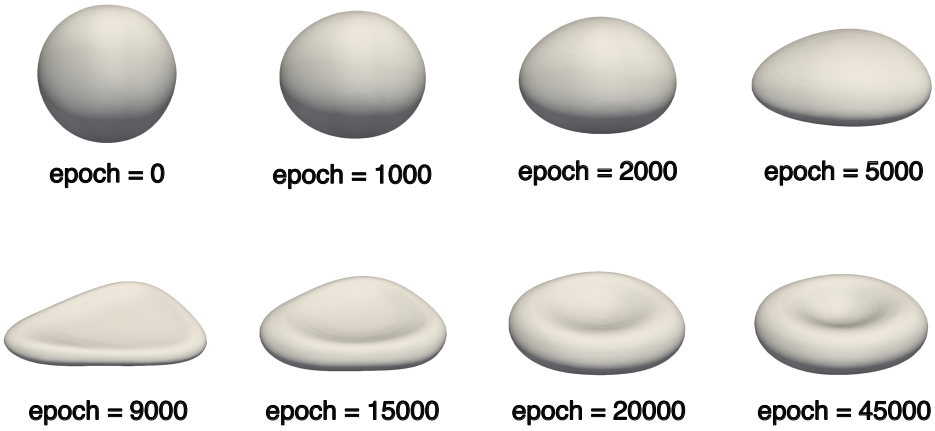


Figure 4.6: Snapshots of obtaining an initial guess for an oblate shape. After 5000 epochs, the penalty term (4.12) is removed and the minimization process is implemented by (4.6) (shapes in the bottom row).

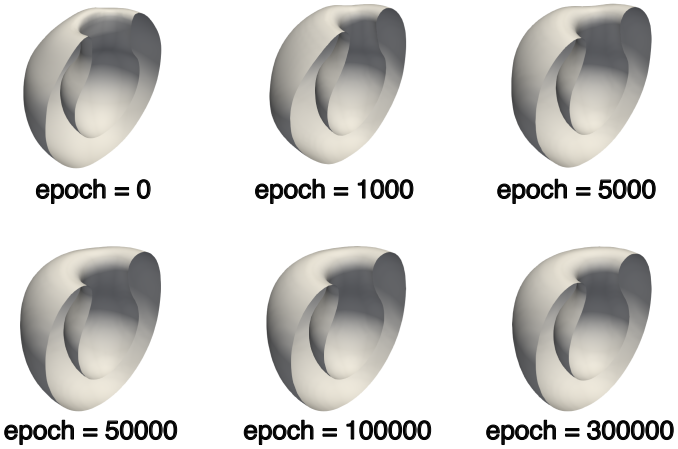


Figure 4.7: Snapshots of the evolution of shapes starting from and initial guess for a stomatocyte $\bar{u} = 0.55$. The shapes are cut through the center mirror.

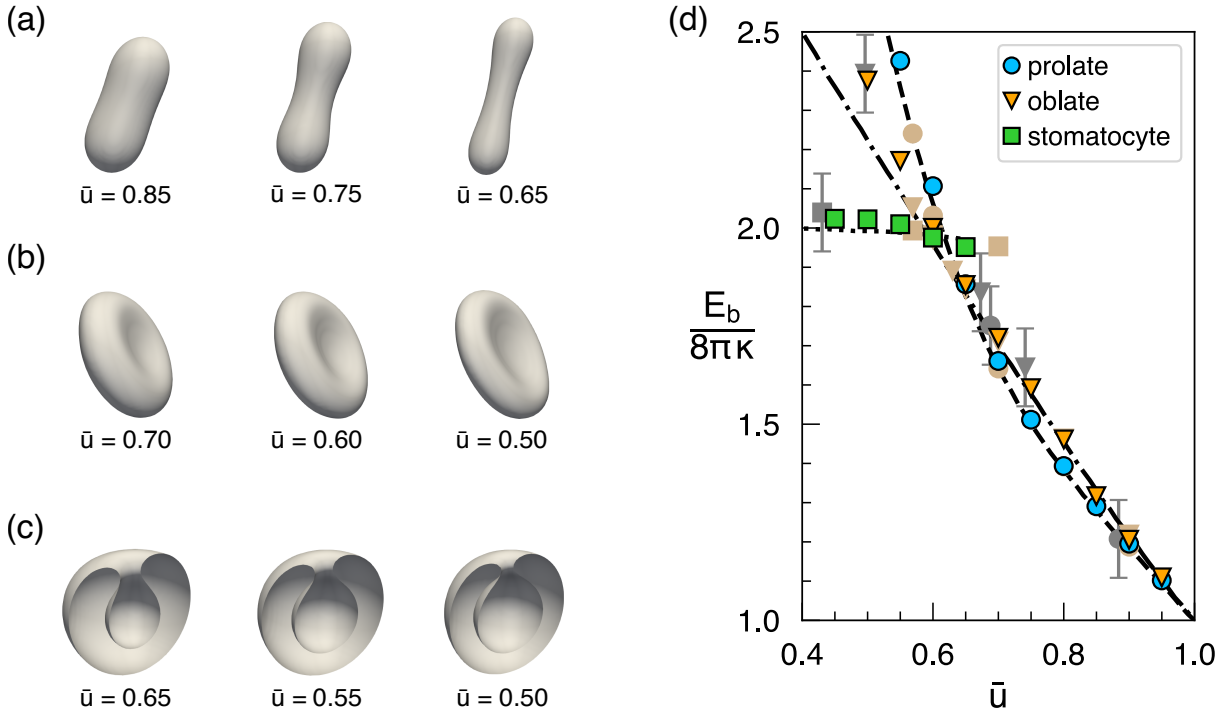


Figure 4.8: Vesicle shapes and energies. Plots (a)-(c) show side views of free-space vesicle shapes: (a) prolate, (b) oblate, and (c) stomatocyte (cut through the center mirror), produced by the current approach. Upon machine-learning convergence, the bending energies (minimum bending energy for each branch of shapes), shown in (d) with colored symbols, agree with those previously determined by a shooting method (dotted, dash-dotted, and dashed lines) [31]. For comparison, the gray symbols represent data extracted from Ref. [48], based on a finite-difference scheme calculation, and the light brown symbols are the data extracted from Ref. [49], calculated by a Fourier spectral method. In our calculations, $\bar{\epsilon} = 0.033$ and $S = 184^3$ are used for (a)-(d).

4.3.3 Axisymmetric Shapes in Free Space

The three branches of the minimizer, corresponding to the free-vesicle shapes produced by the NN approach, are displayed in Figs. 4.8(a)-(c), for various $\bar{u}$. Here, we have set the width scale of the interface $\bar{\epsilon} = 0.033$ and the number of spatial points $S = 184^3$.

The conformations are completely in agreement with those determined in the seminal paper by Seifert et al. [31], who have simplified the problem by adopting an axisymmetric coordinate system [96, 73, 32]. The solutions presented in Fig. 4.8 were produced in a 3D space, without explicitly assuming axisymmetry. This property naturally emerged upon the final convergence of the machine-learning optimization process, even if the initial guess was perturbed to have a non-axisymmetric shape.

The close match of the colored symbols in Fig. 4.8(d) with the E_b curves (minimum bending energy for each branch of shapes) calculated in Ref. [31] signifies the success of the NN approach proposed here. This is particularly noteworthy, given that a relatively small NN (two hidden layers with 20 and 10 nodes) is able to achieve good precision. Deviations along the oblate branch at $\bar{u} = 0.55$ and $\bar{u} = 0.5$ can be attributed to the concave central region of the oblates that come into contact from the top and bottom faces and eventually self-intersect. For comparison, the energy values calculated in Ref. [48], which also used a phase-field theory but employed a traditional finite-difference method, are shown as gray symbols with error bars. The light brown symbols correspond to the minimum bending energy data reported in Ref. [49], obtained using a penalty-based phase-field formulation of the bending energy together with a Fourier spectral method. A notable feature of their results is the data point at $\bar{u} = 0.70$ on the stomatocyte branch. According to Ref. [49], a stable stomatocyte exists at this value of the reduced volume. In contrast, within our NN solver, a stomatocyte at $\bar{u} = 0.70$ relaxes to an oblate shape by lowering its bending energy. This behavior emerges naturally from the NN-based minimization, without imposing any symmetry constraints.

4.3.4 Non-axisymmetric Shapes in Free Space

One of the major advantages of the NN representation of the phase-field model is its built-in capability to handle 3D non-axisymmetric conformations. We have demonstrated this capability for vesicles in both free and confined spaces, reflecting the flexibility and adaptability of our numerical framework.

To explore non-axisymmetry in free space, we first need to derive the phase-field-formulated area difference model, which is described in more detail in Chapter 2 (see

2.5.2). Here, we also provide a brief description of this model.

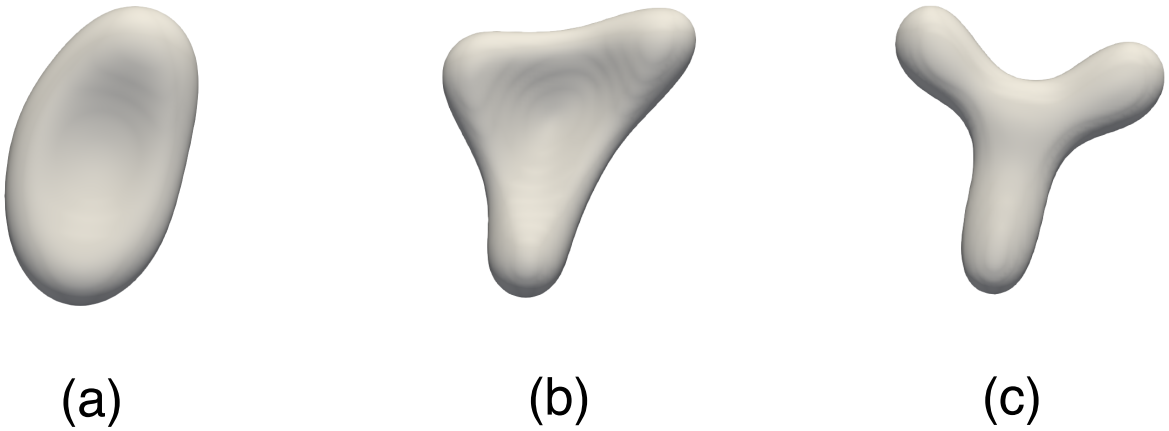


Figure 4.9: Non-axisymmetric vesicle shapes (a)-(c) obtained in free space with a constraint on the reduced area difference, Δa. (b) and (c) are starfish vesicles and are shown from a top view. The parameters used are (a) $\bar{\epsilon} = 0.0375$, $S = 134^3$, $\bar{u} = 0.60$ and $\Delta a = 1.10$, (b) $\bar{\epsilon} = 0.0289$, $S = 184^3$, $\bar{u} = 0.45$ and $\Delta a = 1.35$, as well as (c) $\bar{\epsilon} = 0.025$, $S = 184^3$, $\bar{u} = 0.50$ and $\Delta a = 1.50$.

In the area difference model described in [73], and further investigated for axisymmetric [31] and non-axisymmetric shapes [35], as well as for budding and vesiculation [155], it is assumed that each layer of the lipid bilayer has a fixed surface area. Consequently, there is an area difference between the external layer and the internal one. This area difference (ΔA) is proportional to the integrated local mean curvature M, i.e., $\Delta A \approx 2sM$, where s is the separation between the layers, and

$$M = \int_S H \mathrm{dS}. \tag{4.13}$$

with H as the local mean curvature of the surface element dS. The area difference ΔA can be expressed in a dimensionless form as $\Delta a = M/4\pi R_0$, using the basic unit $R_0 = (A_0/4\pi)^{1/2}$. In the phase-field model, the surface integral expression for M can be rewritten

as a volume integral [45]. Using the NN representation of the phase field $\phi(\mathbf{r};\Theta)$, we have

$$M(\Theta) = -\frac{3}{8}\int \mathrm{d}\mathbf{r}[1-\phi(\mathbf{r};\Theta)^2] \times \left[\nabla^2\phi(\mathbf{r};\Theta)+\frac{1}{\epsilon^2}\phi(\mathbf{r};\Theta)[1-\phi(\mathbf{r};\Theta)^2]\right], \tag{4.14}$$

where ϵ denotes the interface width. To derive this expression, we used the phase-field definition of H and converted the surface integral into a volume integral using the method outlined in Appendix A. This quantity can be included in the cost function J as a constraint on the area difference, expressed as $\lambda_M[M(\Theta) - 4\pi R_0\Delta a]$, where λ_M is the Lagrange multiplier for this constraint, and Δa is fixed to a specific value. The update rule for λ_M follows from (4.8):

$$\lambda_M \leftarrow \lambda_M + \gamma[M(\Theta) - 4\pi R_0\Delta a], \tag{4.15}$$

with the same step size γ.

Examples of non-axisymmetric shapes in free space, obtained from the current NN-based approach with a fixed reduced area difference Δa, are shown in Fig. 4.9(a), (b), and

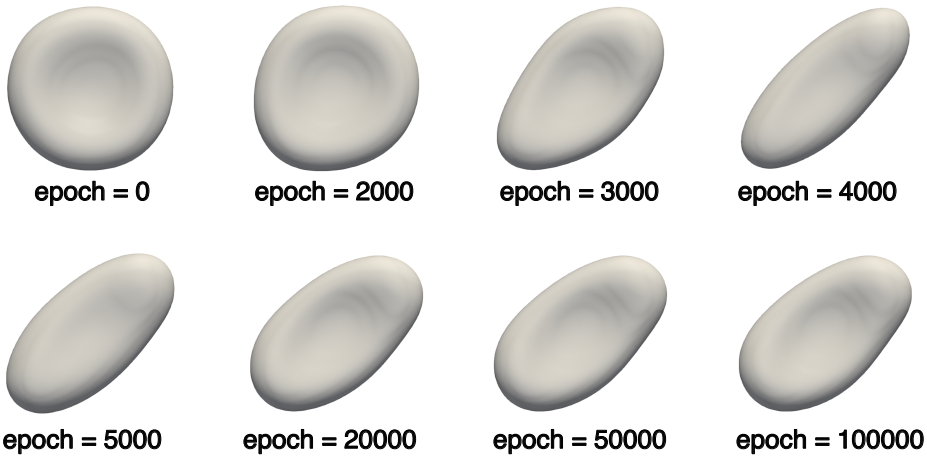


Figure 4.10: Snapshots of the evolution of an oblate shape as the initial guess toward an elongated racket-shaped morphology with $\bar{u} = 0.6$ and $\Delta a = 1.10$.

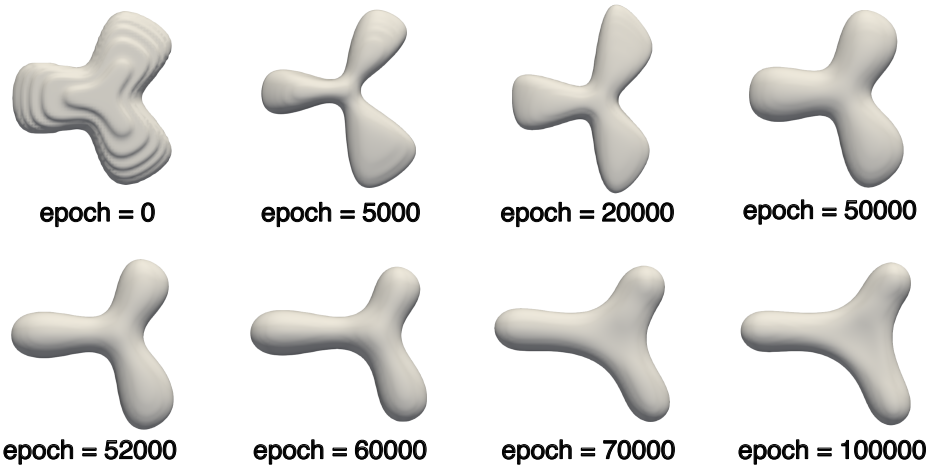


Figure 4.11: Snapshots of the evolution of a starfish from its initial guess to the desired conformation with $\bar{u} = 0.50$ and $\Delta a = 1.50$.

(c) (the last two are the so-called starfish vesicles). These conformations were calculated with an additional constraint according to the area difference model, which fixes Δa [73, 31, 35, 155].

For Fig. 4.9 (a) and (b), the initial Θ is an oblate shape with a particular $\bar{u}$. We then change the value of Δa to induce symmetry breaking in free space. In Fig. 4.10 we show how an oblate shape $\bar{u} = 0.60$ evolves into an elongated racket-shaped conformation when the reduced area difference is set to $\Delta a = 1.10$.

The initial shape for Fig. 4.9 (c) is an oblate spheroid with three equally spaced arms, which is readily constructed from another mean squared error fit to an oblate spheroid equation with sinusoidal variation (using the azimuthal angle) in the radial direction. A simple expression that can be used for this purpose is:

$$\frac{(x_k^2 + y_k^2)\left[\left(\cos\dfrac{3\arctan(y_k/x_k)}{2}\right)^6 + c_1\right]}{c_2^2} + \frac{z_k^2}{c_3^2} \leq 1, \tag{4.16}$$

where c_1, c_2, and c_3 are arbitrary constants. The phase field at the spatial points that satisfy this condition is driven to 1 using (4.10). Figure 4.11 shows the evolution of this

initial guess for a starfish and its convergence to the desired starfish with $\bar{u}$ and $\Delta a = 1.50$.

4.3.5 Vesicles in Hard-wall Confinements

Here, we present another path for producing non-axisymmetric shapes. A detailed exploration of the vesicles in confined spaces is provided in Chapter 5 where we study the effect of different types of hard-wall confinements on different types of shapes with various reduced volumes.

For confined spaces that break axisymmetry, a few examples of hard-wall confinement are presented below (see Fig. 4.12 for schematics). The algorithm described above can be straightforwardly adapted for this purpose by introducing an external potential function

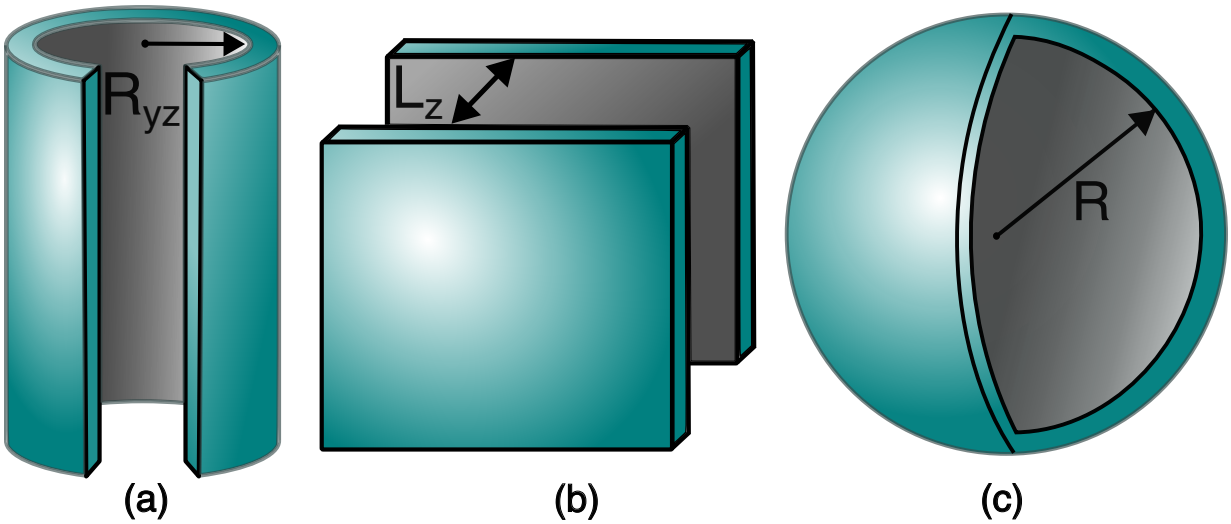


Figure 4.12: Schematics of the three types of hard-wall confinements: (a) cylindrical, (b) slit, and (c) spherical. A segment of the cylindrical and spherical confinements is cut out to reveal the interior of the cavity. The designated dimensions of these confinements are scaled by R_0, resulting in the dimensionless forms $h = R_{yz}/R_0$, $h = L_z/R_0$, and $h = R/R_0$ for the three cases, respectively.

acting on the density profile $1+\phi$,

$$P(\Theta) = \int \mathrm{d}\mathbf{r}[1+\phi(\mathbf{r};\Theta)]\frac{\sigma(\zeta)}{2}, \tag{4.17}$$

where $\sigma(\zeta)$ is the sigmoid function. The argument is taken as $\zeta = c(\alpha_1 x^2+\alpha_2 y^2+\alpha_3 z^2-h^2)$, where h is the confinement dimension scaled by R_0. For slit ($h = (L_z/2)/R_0$), cylindrical ($h = R_{yz}/R_0$), and spherical ($h = R/R_0$) confinements, the values of $[\alpha_1, \alpha_2, \alpha_3]$ are $[0,0,1]$, $[0,1,1]$, and $[1,1,1]$, respectively. Here, $c = 20.0$ to emulate hard-wall confinement. For spherical confinement, the center-of-mass constraint must be removed since the confinement restricts the spatial position of the vesicle. Cylindrical confinement allows the vesicle to

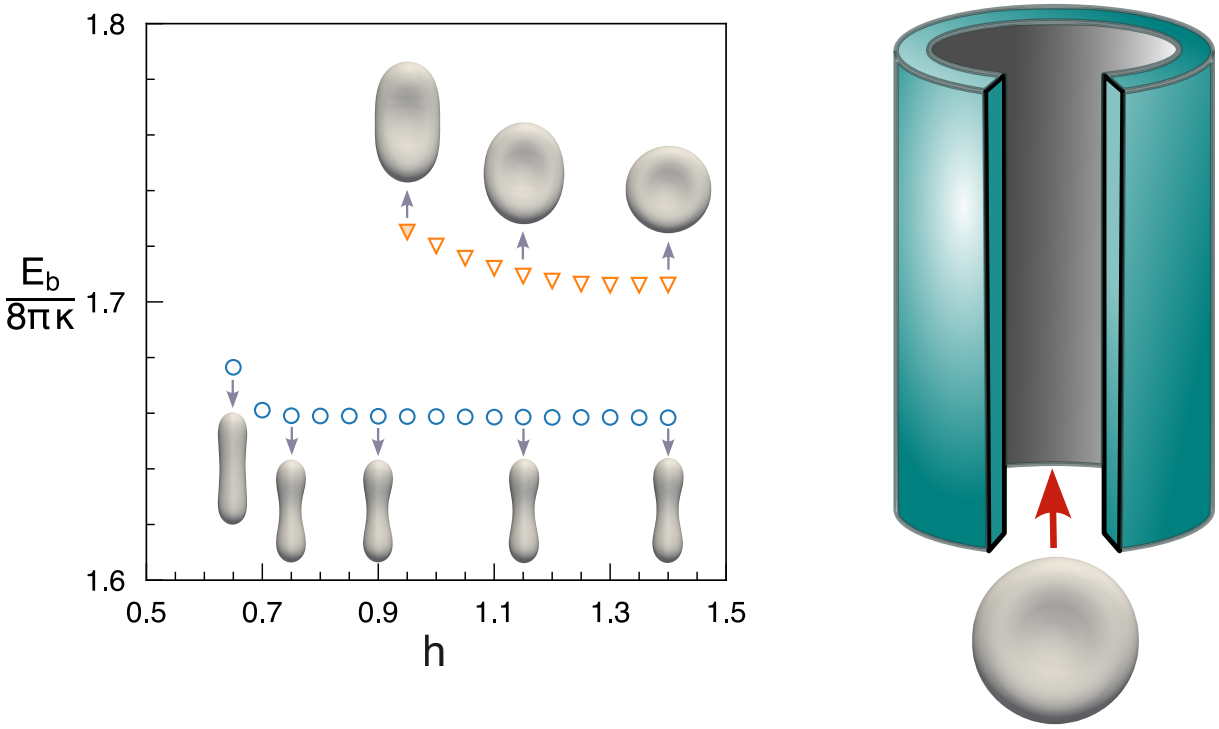


Figure 4.13: Bending energy as a function of confinement dimension h (the converged minimum bending energy for each value of confinement size), for cylindrical type. $\bar{u} = 0.70$, $\bar{\epsilon} = 0.033$, and $S = 184^3$ are taken for all the shapes. The filled point marker indicates the limit of stability for the particular shape, where a jump to a stable (lower bending energy) conformation occurs.

move along the x-axis, while in slit confinement, the vesicle is free to move along the xy-plane. Thus, the center-of-mass constraint must be imposed on one component in the former case and two components in the latter.

By adjusting the confinement dimensions, such as decreasing its radius or width, the vesicle comes into contact with the walls, leading to conformation changes. During this process, the initial conformation undergoes shape transitions, and the corresponding bending energy evolves in tandem. These transitions can capture the intermediate states where vesicle axisymmetry is broken. The Θ values for the initial shapes in the hard-wall confinement simulations are simply borrowed from the converged axisymmetric shapes with a particular $\bar{u}$.

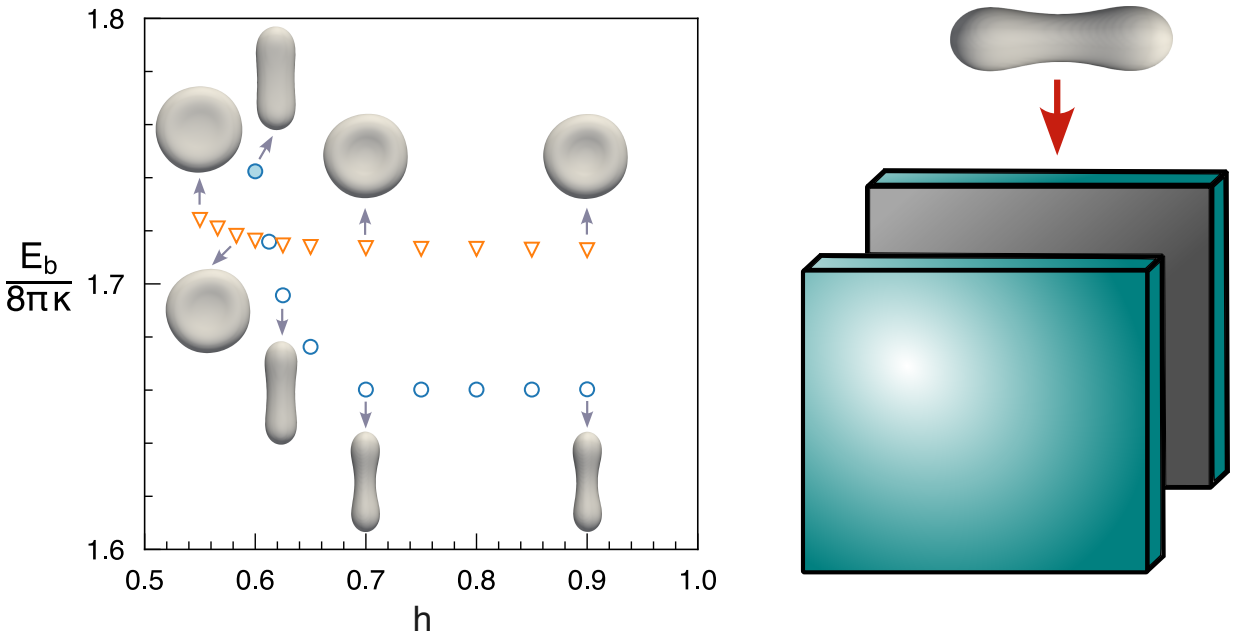


Figure 4.14: Bending energy as a function of confinement dimension h (the converged minimum bending energy for each value of confinement size), for slit type. $\bar{u} = 0.70$, $\bar{\epsilon} = 0.033$, and $S = 184^3$ are taken for all the shapes. The filled point marker indicates the limit of stability for the particular shape, where a jump to a stable (lower bending energy) conformation occurs.

Within a cylindrical confinement, an oblate vesicle ($\bar{u} = 0.70$ and parallel to the x-axis along the long oblate axis) assumes a series of conformations through transition between shapes, with their energies shown by the orange triangles in Fig. 4.13. Evidently, axisymmetry is broken for the intermediate states and the bending energy rises as a result with the confinement dimension being gradually reduced. Below $h = 0.95$ (stability limit) a jump to a more stable conformation, namely prolate, takes place, and the vesicle recovers its axisymmetric state. The prolate shape remains stable at smaller confinement dimensions but becomes more elongated and cylindrical. If h is reversibly increased after the phase transition or the shape is initially a prolate in alignment with the x-axis, the conformation is unchanged since it is the stable shape with the lowest energy in all cases.

Figure 4.14 demonstrates the introduction of a prolate vesicle of $\bar{u} = 0.70$ inside a slit confinement; the long axis of which is parallel to the xy-plane. When the confinement walls press on the sides of the prolate, its axisymmetry is broken, which results into higher energy conformations, shown by the blue circles. A compressed prolate runs into a stability limit at $h \sim 0.60$. Originally metastable, a $\bar{u} = 0.70$ oblate has a higher E_b at large h. As the slit confinement narrows on an oblate vesicle with its long axis in parallel to the walls, due to the thin thickness, it experiences much weaker deformation than its prolate counterpart and maintains the axisymmetry, which gives rise to a weak increase of E_b. The crossing point of the two E_b branches corresponds to a first-order phase transition, between prolate and oblate, both deformed from their ideal shapes.

Under spherical confinement, multiple stages of transitions can occur, shown in Fig. 4.15. Due to its elongated shape, a $\bar{u} = 0.70$ prolate, though preferred as the stable shape in free space, starts to buckle as the confinement radius reduces. This gives rise to a drastic increase in its bending energy. At $h \sim 1.1$, an stability limit is reached. In comparison, a $\bar{u} = 0.70$ oblate can tolerate weak compression on the outer periphery and hence makes a gentler rise in E_b, at much later stage when h is lowered. The crossing point of triangles and circles at $h \sim 1.7$ represents a first-order phase transition between these two states. At an even lower h, approximately at $h \sim 1.2$, a weakly deformed oblate starts to approach an stability limit, and transits into a compressed stomatocyte, taking a different energy branch (squares). The transition is typical of second-order phase transition with continuity in energies. Pressing the confinement walls on the stomatocyte further closes the opening

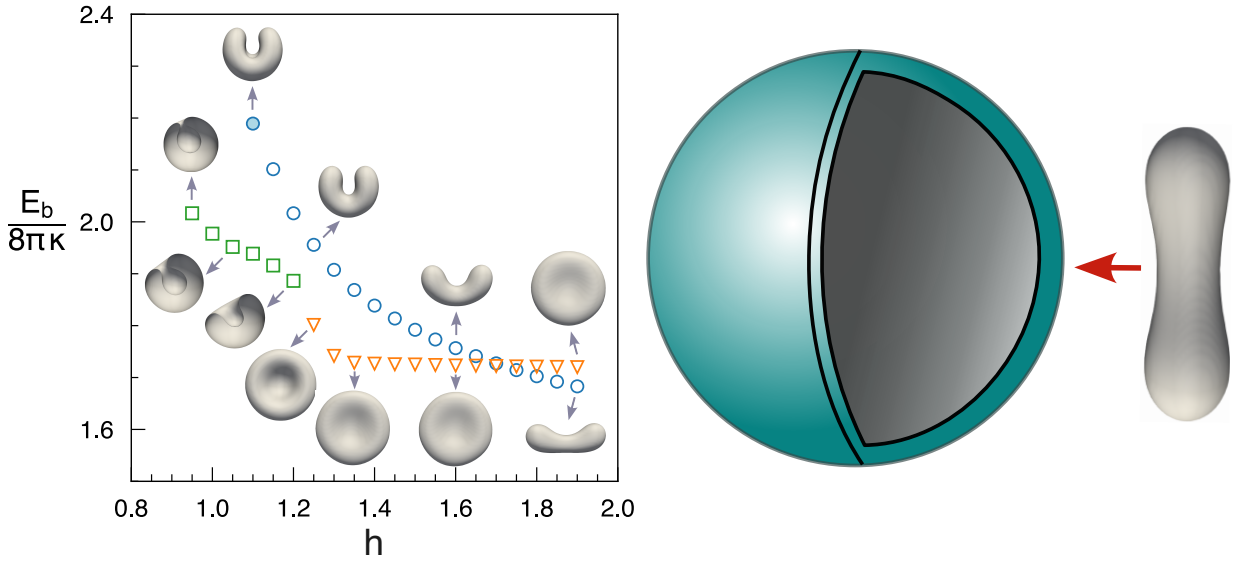


Figure 4.15: Bending energy as a function of confinement dimension h (the converged minimum bending energy for each value of confinement size), for spherical type. $\bar{u} = 0.70$, $\bar{\epsilon} = 0.033$, and $S = 184^3$ are taken for all the shapes. The filled point marker indicates the limit of stability for the particular shape, where a jump to a stable (lower bending energy) conformation occurs. The stomatocytes are cut through the mirror center to reveal the cross-section interior.

and isolates the hollow interior.

4.4 Conclusions

In essence, calculating the vesicle shape based on the Helfrich bending energy model, or its alternative phase-field form, is a minimization problem of a functional. The blueprint for developing a novel computational tool for this purpose, with an artificial neural network (NN) at its core, is laid out here. The algorithm treats both axisymmetric and non-axisymmetric shapes on equal footing and can be used to study shape transformations when symmetry is broken.

In computational physics, the Surface Evolver package [38] is one of the existing tools for generating 3D shapes and has been used for various purposes, including analyzing and calculating vesicle shapes when the shape profile is roughly known [33, 34, 35]. Other finite-element-based and triangulation methods have also been developed for calculating non-axisymmetric vesicle conformations in confinement [36, 76, 37, 77, 78]. Additionally, there have been attempts to compute non-axisymmetric shapes in free space using traditional numerical methods in the context of phase-field formalism [47] and the level-set method [44].

In comparison, our NN-based method has a few characteristics that set it apart. Firstly, it provides a versatile, universal, and flexible framework, opening the door to determining the full range of 3D shapes that might occur due to various physical or chemical conditions [109, 80, 168]. The set of optimal network parameters obtained for a specific shape can be easily stored using minimal storage space and deployed as input for a variety of simulations. Secondly, it avoids the numerical errors often introduced by finite-difference-based methods. For demonstration purposes, a simple feedforward NN is used in this work. It can be expected that more sophisticated NNs and advanced machine learning techniques would yield more accurate solutions and improve computational efficiency.

As a final note, the current solver inherits the main features of the underlying mathematical model, the phase-field theory. Achieving highly accurate shapes with the phase-field model requires smaller ϵ values, which in turn necessitate a more refined spatial grid, significantly increasing the computational cost of optimization. There are several approaches that could potentially address this issue, such as mini-batch training, importance sampling, and Monte Carlo integration—topics worthy of further exploration.

Chapter 5

Vesicles in Confinements

In the previous chapter, we examined specific examples of vesicles with fixed reduced volume ($\bar{u} = 0.70$) confined within three types of hard-wall cavities: cylindrical, slit, and spherical. We demonstrated that these confinement conditions can induce non-axisymmetric shapes. We also observed that vesicle shapes may approach a stability limit, beyond which a transition to a configuration with lower bending energy can occur.

In this chapter, we investigate the physics of confined vesicles in greater depth. We extend the range of the volume constraint to allow for a broader set of vesicle configurations, enabling us to expand the energy diagrams and construct phase diagrams, for instance, in terms of reduced volume and confinement size. Furthermore, we introduce an additional type of hard-wall confinement, namely cubic confinement, to emphasize the versatility of our neural network solver in handling various external potentials.

5.1 Introduction

Several research studies have investigated vesicle confinement, both theoretically and experimentally. Here, we focus on theoretical and numerical approaches to this topic. Interest in vesicle confinement has grown in recent years due to its implications for the equilibrium shapes of vesicles subject to external constraints—for example, when confined inside other

vesicles [37]. The presence of an external potential can significantly alter the vesicle's shape, often leading to non-axisymmetric equilibrium shapes.

Such scenarios arise naturally in biological systems. For instance, mitochondria possess double membranes, where the inner membrane has a larger surface area than the outer membrane, leading to folding and deformation of the inner membrane [169, 170, 171]. In engineered systems, such as drug delivery platforms, therapeutic agents are often encapsulated within vesicles (e.g., extracellular vesicles) for improved stability and targeted delivery [172, 173, 174, 175]. In such cases, understanding the equilibrium shape of a vesicle, and how it deforms during uptake, transport and confinement in narrow capillaries, or passage through pores, is essential for optimizing delivery mechanisms and improving therapeutic efficacy.

As mentioned in the previous chapter, both axisymmetric and non-axisymmetric vesicle shapes can emerge when vesicles are placed inside hard-wall confining cavities. Theoretical studies have examined several types of confinement geometries, including cylindrical (tube), slit (parallel plates), and spherical confinements. Among these, spherical confinement has received the most attention in the literature [36, 37, 111, 77, 78]. Nevertheless, other geometries such as cylindrical (tube), slit, and ellipsoidal confinements have also been investigated in a number of studies [110, 76, 79].

The placement of phospholipid vesicles in cylindrical and slit confinements was theoretically investigated in [110]. Using the Helfrich model along with considerations of entropy reduction due to spatial restriction, the authors examined vesicles confined within narrow cylindrical tubes and slit-like geometries. The study explicitly addressed how the reduction of accessible free volume affects equilibrium vesicle shapes. By varying a confinement parameter that quantifies the degree of spatial restriction, the authors identified significant shifts in the transition points between stable prolate and oblate shapes. Their analysis, which focused on axisymmetric configurations, showed that slit confinement tends to stabilize oblate shapes due to their intrinsically flatter geometry, which leads to smaller entropy losses under confinement. In contrast, cylindrical confinement produced more complex behavior: while oblate shapes were initially stabilized, increasing confinement eventually favored prolate configurations.

The goal of [110] was to elucidate the mechanical behavior of vesicles in confinement, with potential implications for biophysical processes such as the passage of red blood cells through narrow capillaries. As discussed earlier in Section 2.2.1, accurate modeling of red blood cells requires the inclusion of membrane skeleton contributions. Nonetheless, the study of confined phospholipid vesicles can still offer valuable qualitative insights into shape transitions and morphological responses to confinement.

Several research works have investigated the equilibrium shapes of vesicles in spherical confinement. For example, in [36], the morphological transformations of fluid membrane vesicles confined within spherical cavities were explored using finite element simulations based on the Helfrich model. The authors examined scenarios in which the membrane surface area exceeded that of the enclosing spherical container, leading to the emergence of characteristic invaginations (empty space within the vesicle connected to exterior via a small opening). Their results showed that moderate surface growth initially produces a single, axisymmetric invagination with a bulb-like morphology connected to the outer membrane via a narrow neck. As the surface area further increases, symmetry-breaking transitions occur, giving rise to ellipsoidal invaginations joined by slit-like openings. For even larger excess surface areas, secondary invaginations appear within the primary one, forming complex stomatocyte-like structures. A comprehensive morphological phase diagram was constructed, categorizing these membrane shapes as functions of scaled area and volume constraints. The study demonstrated that spherical confinement plays a critical role in shaping membrane morphology, producing distinct transitions that closely align with theoretical predictions and differ from those of unconfined vesicles.

In follow-up research, Kahraman et al. investigated vesicles confined within ellipsoidal cavities [76]. They found that ellipsoidal confinement led to distinct morphological transitions, starting with smooth, axisymmetric invaginations and progressing toward more complex, symmetry-broken configurations as membrane area increased. Notably, the resulting shapes included elongated, ellipsoidal invaginations connected to the outer membrane by narrow, slit-like necks aligned along the major axis of the ellipsoidal container. These morphologies were markedly different from those observed under spherical confinement, underscoring the influence of container geometry on vesicle mechanics. The authors also investigated the role of spontaneous curvature in shaping these structures, showing that

variations in spontaneous curvature can shift the critical points of morphological transitions and alter neck geometries. Their simulations further revealed that these vesicle configurations remained stable under moderate deformations of the ellipsoidal container, highlighting the robustness of the equilibrium shapes.

A few rigorous theoretical studies on the spherical confinement of lipid membrane vesicles have validated their predictions against experimental observations obtained using techniques such as confocal microscopy. We reviewed these studies in Section 2.2.2 [37, 77].

The spherical confinement of vesicles has also received attention in a variety of other interesting settings. For instance, in [111], the equilibrium shapes of toroidal membrane vesicles confined within spherical cavities were explored. These are topologically a different genus of shapes and differ from the spherical genus, which we have investigated throughout this thesis. Employing the Helfrich model, the authors constructed a comprehensive geometrical phase diagram characterizing stable vesicle morphologies as functions of scaled membrane area and reduced volume. In another study, a detailed numerical investigation was carried out on membrane vesicles exhibiting flexoelectric behavior under spherical confinement in the presence of an external uniform electric field [78]. Using finite element simulations and a shooting method tailored for axisymmetric configurations, the authors examined how flexoelectric coupling influences equilibrium vesicle shapes by varying the scaled area, reduced volume, and electric field strength. The study demonstrated the significant role played by flexoelectric effects in shaping vesicle morphology, notably inducing elongation and symmetry-breaking transitions that depend on the magnitude and orientation of the applied electric field.

In another study, adhesion to the confinement walls was introduced and its effects were examined using a rigorous mechanical framework that investigated the collapse and invagination of phospholipid vesicles [79]. Using Helfrich model coupled with membrane-membrane and membrane-container contact interactions, the authors analyzed equilibrium morphologies within cylindrical and spherical confinements, incorporating both analytical and finite element methods. Adhesion between the vesicle and the confining boundary was introduced as a key control parameter, allowing systematic exploration of its interplay with the Helfrich model.

The authors drew explicit parallels between their theoretical predictions and biological systems. For instance, the spherical invaginations observed in their model closely resemble mitochondrial cristae, while the layered, onion-like morphologies mimic the stacked and folded structures of the endoplasmic reticulum. These comparisons demonstrate how purely mechanical confinement and bending elasticity can reproduce morphologies that are central to cellular architecture.

We emphasize that the confinement studies reviewed above, as well as the one presented and elaborated here, are inherently static or quasi-static in nature. Specifically, in our numerical calculations, we begin with an initial shape that minimizes the bending energy for a given set of surface area and volume constraints. An external potential is then introduced to represent the hard-wall confinement with a specified geometry. To explore the effect of confinement, we incrementally increase or decrease the size of the cavity along a relevant dimension. At each step, the equilibrium configuration is determined by applying our NN solver with the updated confinement size imposed as a constraint.

There are studies in the literature—beyond the scope of the confinement experiments presented here—that investigate vesicles confined in capillaries, narrow tubes, and porous media with various pore types and sizes. In these scenarios, in addition to the external potential from confinement, the vesicles are also subjected to forces exerted by fluid flow (e.g., shear flow or Poiseuille flow) [176, 177, 178, 179, 180, 181]. These dynamic settings necessitate the inclusion of flow-induced forces in both the theoretical formulation and numerical implementation to capture the resulting dynamic equilibrium shapes. Such simulations can also be extended to model red blood cells in capillaries, provided that the energetic contributions of the membrane skeleton are incorporated into the model [182].

5.2 Modeling Methods

Following our approach from the previous chapter, we use the phase-field-formulated Helfrich model to calculate the three-dimensional morphology of vesicles. The phase field is represented by a feedforward neural network, illustrated in Fig. 4.1. The cost function (4.6) is again employed to obtain the 3D shape solution to the constrained Helfrich model.

As discussed in Section 4.3.5, the additional constraint $P(\Theta)$—that is, the constraint invoking a specific type of confinement as an external potential acting on the density profile $1+\phi$—is incorporated into $J(\Theta)$ using the definition (4.17).

The shape of a particular hard-wall confinement with an interior cavity is modeled by $\sigma(\zeta)$, the sigmoid function (3.1). The argument is defined as

$$\zeta = c(\alpha_1 x^2 + \alpha_2 y^2 + \alpha_3 z^2 - h^2), \tag{5.1}$$

where h is the confinement dimension scaled by $R_0 = (A_0/4\pi)^{1/2}$, with A_0 denoting the surface area of a sphere. The schematics of slit ($h = (L_z/2)/R_0$), cylindrical (tube) ($h = R_{yz}/R_0$), and spherical ($h = R/R_0$) confinements are shown in Fig. 4.12. For each type of confinement, the corresponding values of $[\alpha_1, \alpha_2, \alpha_3]$ are $[0, 0, 1]$, $[0, 1, 1]$, and $[1, 1, 1]$, respectively. To emulate the hard-wall characteristic of the confinement, we set $c = 20.0$.

The cubic confinement can be modeled by summing the contributions from three slit confinements oriented along the xy-, yz-, and xz-planes, as follows

$$\text{cube}(\sigma(\zeta)) = \sigma(c(x^2 - h^2)) + \sigma(c(y^2 - h^2)) + \sigma(c(z^2 - h^2)). \tag{5.2}$$

Figure 5.1 shows a schematic of a cubic confinement, with the confinement dimension given by $h = (L/2)/R_0$.

To maintain the position of the center of mass of the confined vesicle near the center of the simulation box, we employ a constraint of the form $\lambda_{\text{CM}}\mathbf{R}(\Theta)^2$, where $\mathbf{R}(\Theta)$ is defined in (4.9). This constraint must be treated differently for each type of confinement. For spherical and cubic confinements, it is omitted from the cost function because these geometries fully enclose and restrict the vesicle within their internal space. By contrast, in cylindrical and slit confinements, additional treatment is necessary. The cylindrical (tube) confinement is open at its ends, which allows a vesicle to move along the cylinder's longitudinal axis; therefore, the center of mass must be constrained along this axis (a one-component term if the cylinder is aligned with the x-, y-, or z-axis). In a slit confinement, a vesicle can translate parallel to the slit walls, and thus the center of mass must be constrained within the plane parallel to the walls (a two-component term if the slit lies along the xy-, yz-, or xz-plane).

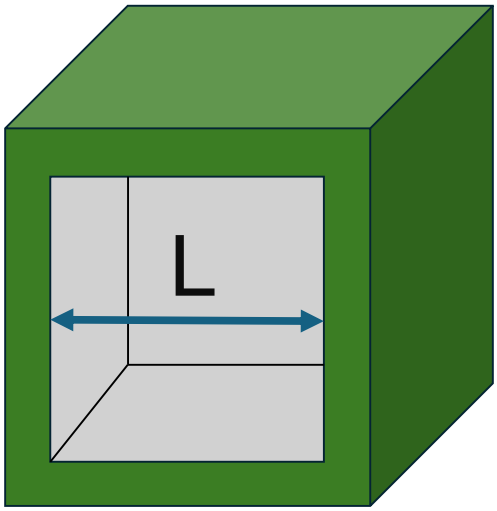


Figure 5.1: Schematic representation of a hard-wall cubic confinement. A portion of the cube is removed to expose the interior cavity. The confinement dimension is normalized by the characteristic length scale R_0, yielding the dimensionless size $h = L/R_0$.

5.3 Results

The numerical results of our confinement calculations are described in the following. For each confinement, a vesicle with a particular reduced volume $\bar{u} = 3V/4\pi R_0^3$ is placed inside the cavity of the hard-wall confinement (we examine $\bar{u}$ values that are 0.05 apart). We start with a cavity size h that is larger than the spatial extent of the vesicle. For this h and a fixed $\bar{u}$, the NN solver is run for 5×10^4 to 10×10^4 epochs to ensure that the shape has converged to an approximate solution, such that if a transition to a lower-energy configuration is expected, it is achieved during this phase of NN training. The value of h is then decremented by 0.05, and the NN solver is run again with the new setting. This procedure is repeated until a reasonable lower limit for h is reached. The same numerical process is carried out for each reduced-volume value of a given vesicle. For each $(h, \bar{u})$, we obtain a set of Θ representing the shape of the corresponding vesicle. We limit the number of epochs to the 5–10×10^4 range in this serial format, since the computational cost can become large when several values of h must be examined. To achieve an acceptable level of convergence, we continue the learning process for the Θ corresponding to each $(h, \bar{u})$ in

parallel format, where up to 5×10^5 training epochs are run simultaneously.

While decrementing h, the shapes may reach their stability limit and transform into another configuration with a lower bending energy. To test whether these lower-energy conformations are stable, the value of h is incremented by 0.05 until the cavity size exceeds the spatial size of the vesicle. In this way, we accumulate simulation data for both the bending energy as a function of h and the vesicle configurations for each reduced volume $\bar{u}$ versus h. We use these data to construct stability, energy, and phase diagrams for the slit, tube, and spherical confinements. For the cubic confinement, we provide only energy diagrams, with the observed shapes illustrated within the diagrams as well.

We note that for these numerical calculations, the non-dimensionalized interface length scale is set to $\bar{\epsilon} = 0.033$ ($\bar{\epsilon} = \epsilon/R_0$). The number of spatial points is $S = 150^3$, corresponding to a discretization of the domain $[-3, 3]^3$ using a uniform finite grid.

For all the shapes that are either stomatocytes or related to the stomatocyte branch of shapes, namely squeezed shapes and squeezed stomatocytes, we have cut the shapes into halves at the mirror center to reveal their interior for a better overall view and clear classification.

5.3.1 Cylindrical or Tube Confinement

We examine the morphology of the three main axisymmetric shapes—prolates, oblates, and stomatocytes—within the cylindrical or tube confinement (see Fig. 4.12). We begin with oblates in the range $\bar{u} \in [0.55, 0.75]$, placing them inside the confinement such that their long axis aligns with the tube's longitudinal axis. As the confinement size h is reduced, the oblate shapes deform and elongate along the tube axis. Gradually, these shapes lose their axial symmetry and become biaxial. Figure 5.2 presents the stability diagram for the oblates, organized by their $(h, \bar{u})$ coordinates. Two distinct regions are identified: (i) a light red region, where oblates of different $\bar{u}$ retain their axisymmetric conformation, and (ii) a dark red region, labeled "squeezed shapes", where vesicles in contact with the tube walls lose their axial symmetry. At certain stability limits, marked by the boundaries of the left side of the dark red region, the squeezed biaxial shapes reach a maximum bending energy

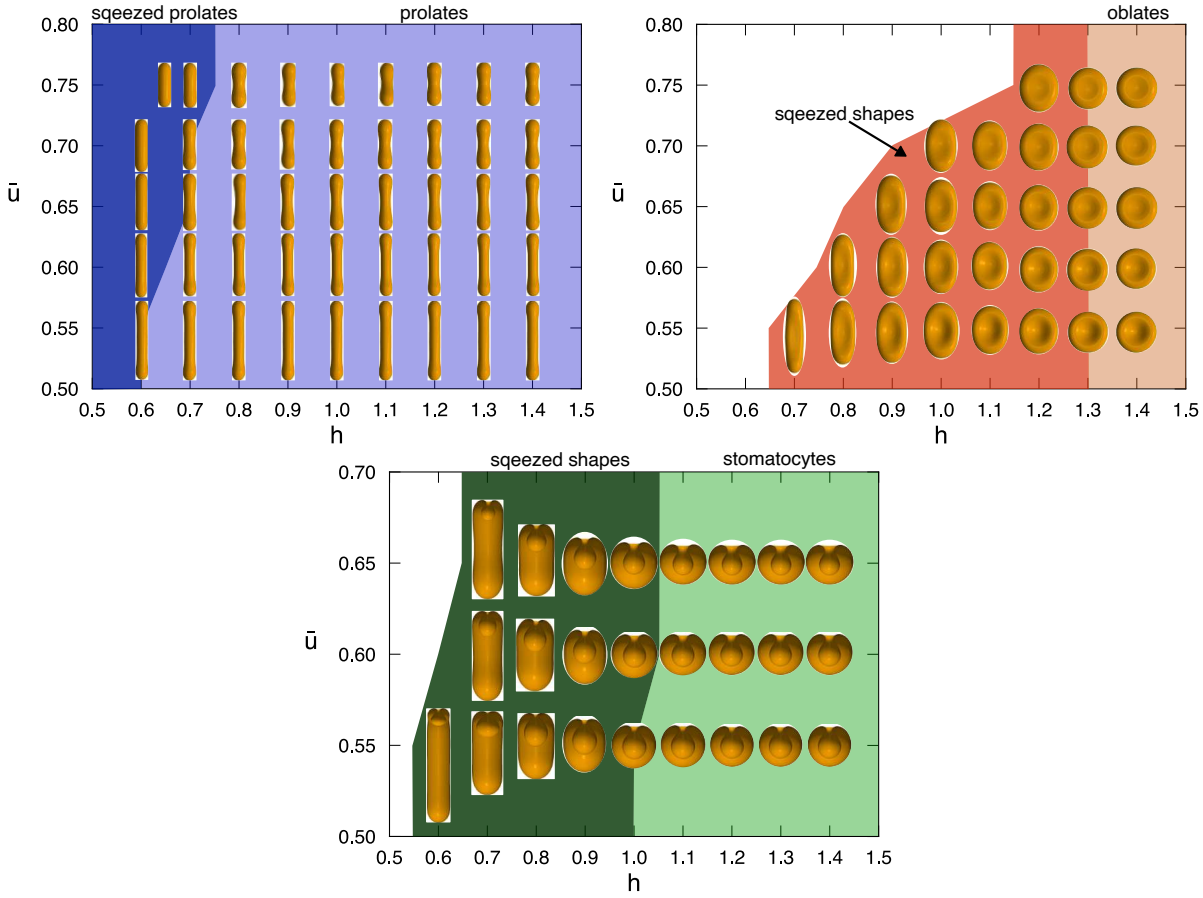


Figure 5.2: Stability diagrams of prolates, oblates, and stomatocytes inside a cylindrical (tube) confinement. Shapes are organized on a $(h, \bar{u})$-grid. Highlighted regions correspond to distinct shape categories: light blue for prolates, dark blue for squeezed prolates, light red for oblates, dark red for squeezed (biaxial) shapes originating from oblates, light green for stomatocytes, and dark green for squeezed shapes originating from stomatocytes. Shapes are converged to their minimum bending energy for all $(h, \bar{u})$.

and undergo a transformation to lower-energy conformations, specifically axisymmetric prolates.

The prolate stability diagram in Fig. 5.2 illustrates the conformations of prolate shapes with $\bar{u} \in [0.55, 0.75]$. These prolates are obtained by squeezing and deforming oblates, as

described earlier (light blue region in the stability diagram). As the confinement size h decreases, the tube walls compress the prolates, deforming their characteristic dumbbell shape into a more uniform cylindrical configuration, which exhibits higher bending energy than the corresponding free-space prolate. This region is highlighted in dark blue in the diagram and is labeled "squeezed prolates". When h is increased, these prolate shapes preserve their conformation and remain either metastable or stable, depending on their $\bar{u}$ value.

The stomatocytes with $\bar{u} \in [0.55, 0.65]$ are placed inside the tube confinement such that the mouth of the vesicle is aligned with the long axis of the tube. Reducing h results in the stomatocytes being squeezed and deformed along the confinement. For $h \sim 0.7$ (see lower panel in Fig. 5.2), the deformed shapes exhibit both prolate-like and stomatocyte-like characteristics with relatively high bending energies. At their stability limits, these shapes transition to a lower-energy conformation, namely prolates. In the stability diagram, the region highlighted in light green corresponds to stomatocytes at their lowest bending energy, while the region containing deformed shapes is shaded dark green and labeled "squeezed shapes".

The energy diagrams of the tube (cylindrical) confinement in Fig. 5.3(a)–(e) present the calculated bending energy values for $\bar{u} \in [0.55, 0.75]$. Prolates are represented by blue circles, oblates by orange triangles, and stomatocytes by green squares. No stomatocyte data appear in Fig. 5.3(d) and (e) because these shapes are not stable at the corresponding $\bar{u}$ values (unless stabilized by an external potential such as spherical confinement, which we discuss later).

In Fig. 5.3(a)–(c), the points where the bending energy curves intersect correspond to discontinuous first-order phase transitions. For $\bar{u} = 0.55$, prolates exhibit higher bending energies, with one oblate–prolate transition at $h \sim 0.8$ and one stomatocyte–prolate transition at $h \sim 0.7$. At $\bar{u} = 0.60$, the higher bending energy of prolates is still evident, and the oblate–prolate and stomatocyte–prolate transitions occur close to each other at $h \sim 0.85$. It is also notable that the oblate and stomatocyte branches have similar bending energy values, particularly in the free-space region of the diagram (leftmost side).

For $\bar{u} = 0.65$, the stomatocyte–prolate transition is absent, leaving only one identifi-

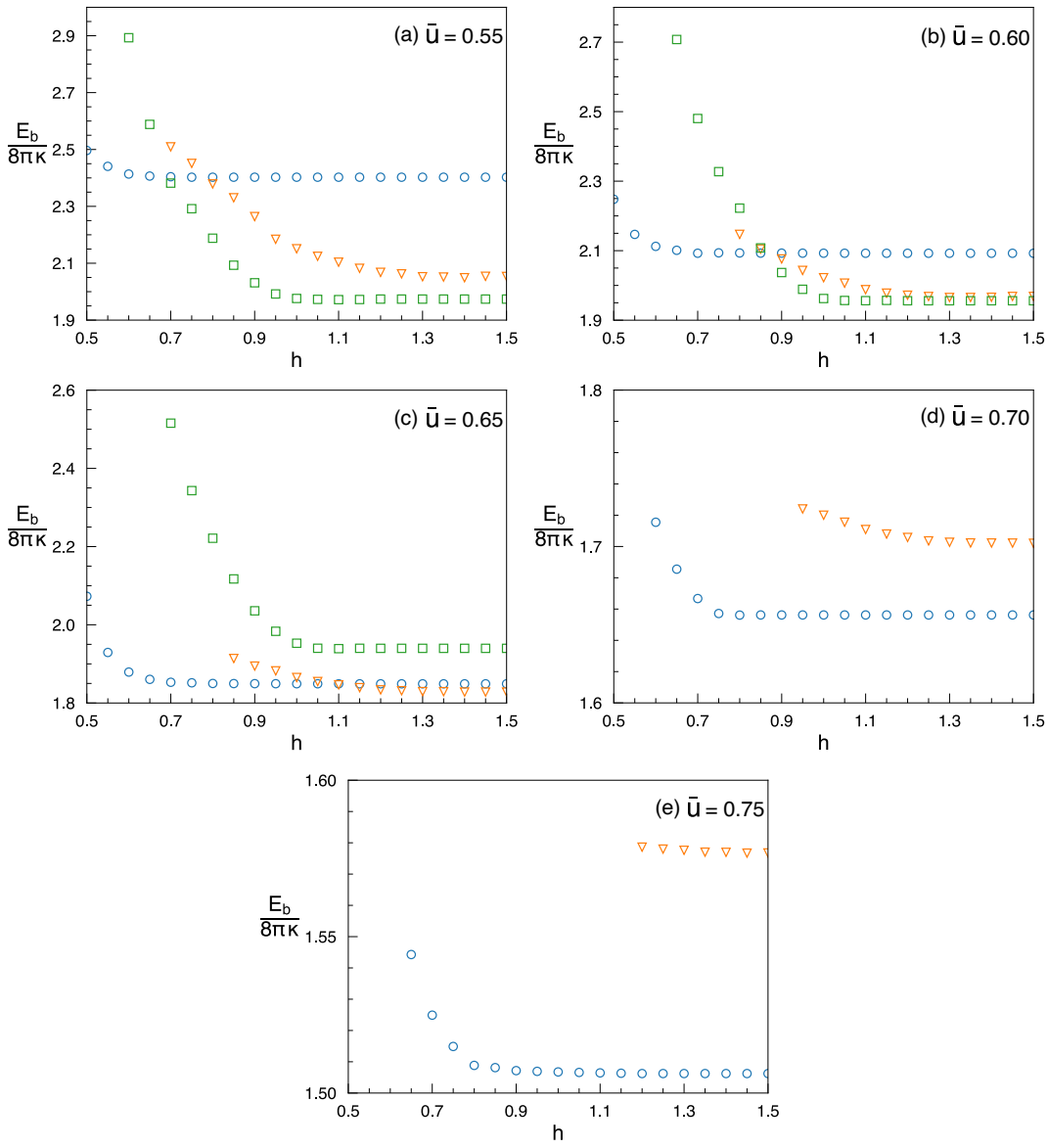


Figure 5.3: Bending energy (in units of $8\pi\kappa$) as a function of tube confinement size h for different values of the reduced volume $\bar{u}$, panels (a)–(e). The prolate branch is represented by blue circles, the oblate branch by inverted orange triangles, and the stomatocyte branch by green squares. Bending energies are the converged minimum value for each h.

able oblate–prolate transition at $h \sim 1.1$. Nevertheless, the stomatocyte branch remains metastable, and as deformation increases at lower h, the squeezed stomatocyte shapes reach their stability limit and transform into pure prolates, thereby losing their high bending energies. For higher values, $\bar{u} = 0.70$ and $\bar{u} = 0.75$, no phase transitions occur: the oblate branch is metastable, whereas the prolate branch is the stable ground state with lower bending energy.

Overall, in all the bending energy diagrams, we observe that the deformed shapes—particularly the squeezed shapes of the stomatocyte branch—reach relatively high bending energies before hitting their stability limit. However, for $\bar{u} = 0.70$ and $\bar{u} = 0.75$, where a stable stomatocyte branch does not exist, the squeezed prolate shapes attain higher bending energies. Since squeezed prolates in a tube cannot transform into any other lower-energy shape, we conclude that they will continue to acquire higher bending energies as h is decremented until the shape diverges numerically. In an actual physical setting, this elevated bending energy may lead to rupturing of the lipid bilayer.

The phase diagram for the tube (cylindrical) confinement is illustrated in Fig. 5.4, where abbreviated labels denote the different regions of the diagram. Here, "spr" represents squeezed prolates, "pr" represents prolates, "ob" denotes oblates, "sto" denotes stomatocytes, and "ss" corresponds to squeezed shapes, which include both deformed oblates (non-axisymmetric or biaxial) and deformed stomatocytes that retain axial symmetry. The color code in the phase diagram follows that of the stability diagrams in Fig. 5.2.

The large black dots at three distinct $(h, \bar{u})$ coordinates on the diagram are read from the bending energy plots in Fig. 5.3. They represent first-order (discontinuous) phase transitions, where the bending energies of different shape branches intersect. The dot at $(h \sim 1.1, \bar{u} = 0.65)$ corresponds to the transition from deformed oblates (dark red "ss") to prolates; the one at $(h \sim 0.85, \bar{u} = 0.60)$ marks the transition from deformed stomatocytes (dark green "ss") to prolates; and the dot at $(h \sim 0.7, \bar{u} = 0.55)$ denotes the transition from deformed stomatocytes (dark green "ss") to prolates. The dots are connected by linear interpolation, depicted with thick dashed lines, to delineate approximate phase boundaries. This interpolation is extended below $\bar{u} = 0.55$ with a thick dotted line, serving as an informed extrapolation that follows the trajectory of the existing interpolants. We speculate that the shape transition in this region is also first-order. Finally, the two horizontal

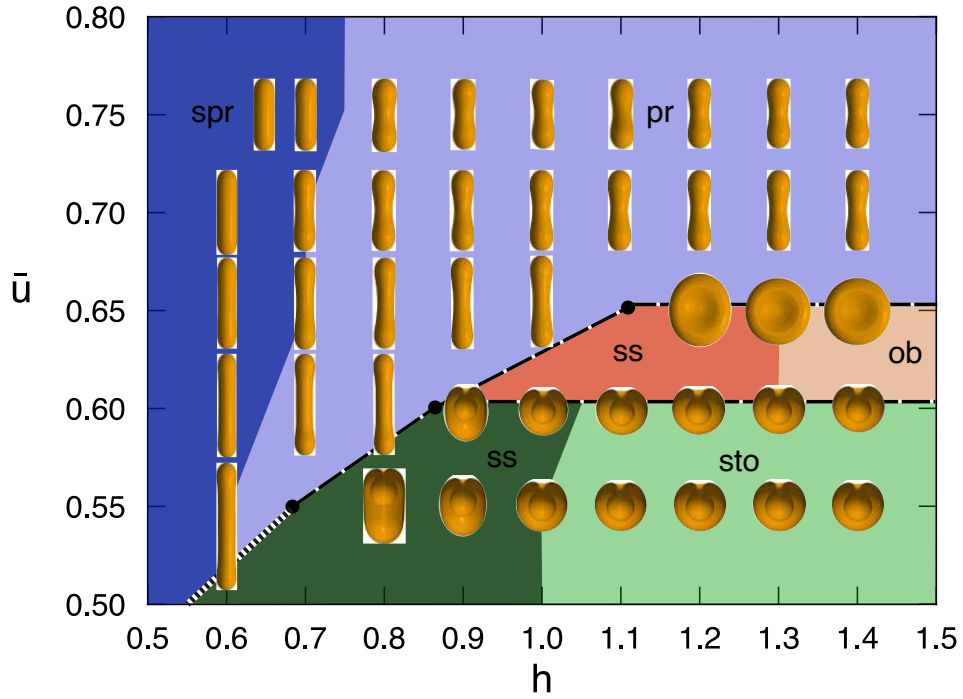


Figure 5.4: Phase diagram of vesicles in a cylindrical (tube) confinement on a $(h, \bar{u})$-grid. Abbreviations denote regions: "spr" (squeezed prolates), "pr" (prolates), "ob" (oblates), "sto" (stomatocytes), and "ss" (squeezed shapes from oblates and stomatocytes). Large black dots and the dashed lines mark discontinuous first-order phase transitions, while the thick dotted line extrapolates the phase boundary to lower $\bar{u}$. Shapes are converged to their minimum bending energy for all $(h, \bar{u})$.

thick dashed lines at $\bar{u} \sim 0.60$ and $\bar{u} \sim 0.65$ indicate the discontinuous prolate–oblate and oblate–stomatocyte transitions reported by Seifert et al. [31].

5.3.2 Slit Confinement

For the case of slit confinement (see Fig. 4.12), the morphological changes of the three main axisymmetric shapes, i.e., prolates, oblates, and stomatocytes, are examined. We begin with prolates having $\bar{u} \in [0.55, 0.90]$, positioning them inside the confinement such that

their long axis is parallel to the walls of the slit. As the confinement size h is reduced, the slit walls come into contact with the vesicle, deforming and squeezing it so that its axisymmetry is broken, giving rise to biaxial shapes. In Fig. 5.5, the stability diagram of prolates is illustrated in terms of $(h, \bar{u})$ coordinates, along with snapshots of the converged 3D solutions (outputs of the NN solver for each $(h, \bar{u})$). Two distinct regions are evident. The first is highlighted in light blue, where prolates with different $\bar{u}$ retain their unperturbed conformations. As the slit narrows further, the walls begin to press and deform the prolate shapes; this region, where the squeezed shapes appear, is highlighted in dark blue and labeled "squeezed shapes". At certain stability limits, delineated by the border on the left side of the dark blue region, the squeezed biaxial shapes reach a maximum bending energy and transform to either a higher- or lower-energy branch of conformations, depending on the value of the reduced volume $\bar{u}$.

The oblate stability diagram in Fig. 5.5 illustrates the conformations of oblate shapes with $\bar{u} \in [0.55, 0.90]$. These oblates are obtained by squeezing and deforming prolates between the slit walls (light red region in the stability diagram). As the confinement size decreases, the narrowing slit presses against the broad sides of the oblates, smoothing out the central depressions on both faces, especially for low-$\bar{u}$ oblates, and producing higher bending energies than their free-space counterparts. This region is highlighted in dark red in the diagram and labeled "squeezed oblates". When h is gradually increased, the oblates maintain their conformations and remain either metastable or stable, depending on their $\bar{u}$ value. The oblate stability diagram also contains a region where our numerical calculations indicate that certain oblate shapes cannot be squeezed below specific h values, resulting in numerical divergence. This region is designated by hatching in the diagram.

The stomatocytes with $\bar{u} \in [0.55, 0.65]$ are placed between the slit walls such that the central axis of the shapes (aligned with their mouth) is perpendicular to the walls. Reducing h results in squeezing and deforming the stomatocytes. For $h < 0.85$ (see lower panel in Fig. 5.5), the shapes begin to deform, although this deformation is weak and does not lead to a noticeably large increase in bending energy. We have used a dark green color to highlight this region and labeled it "squeezed stomatocytes". At their stability limits, these deformed stomatocytes transform into oblates. The region of the stability diagram highlighted in light green corresponds to stomatocytes at their lowest bending energy.

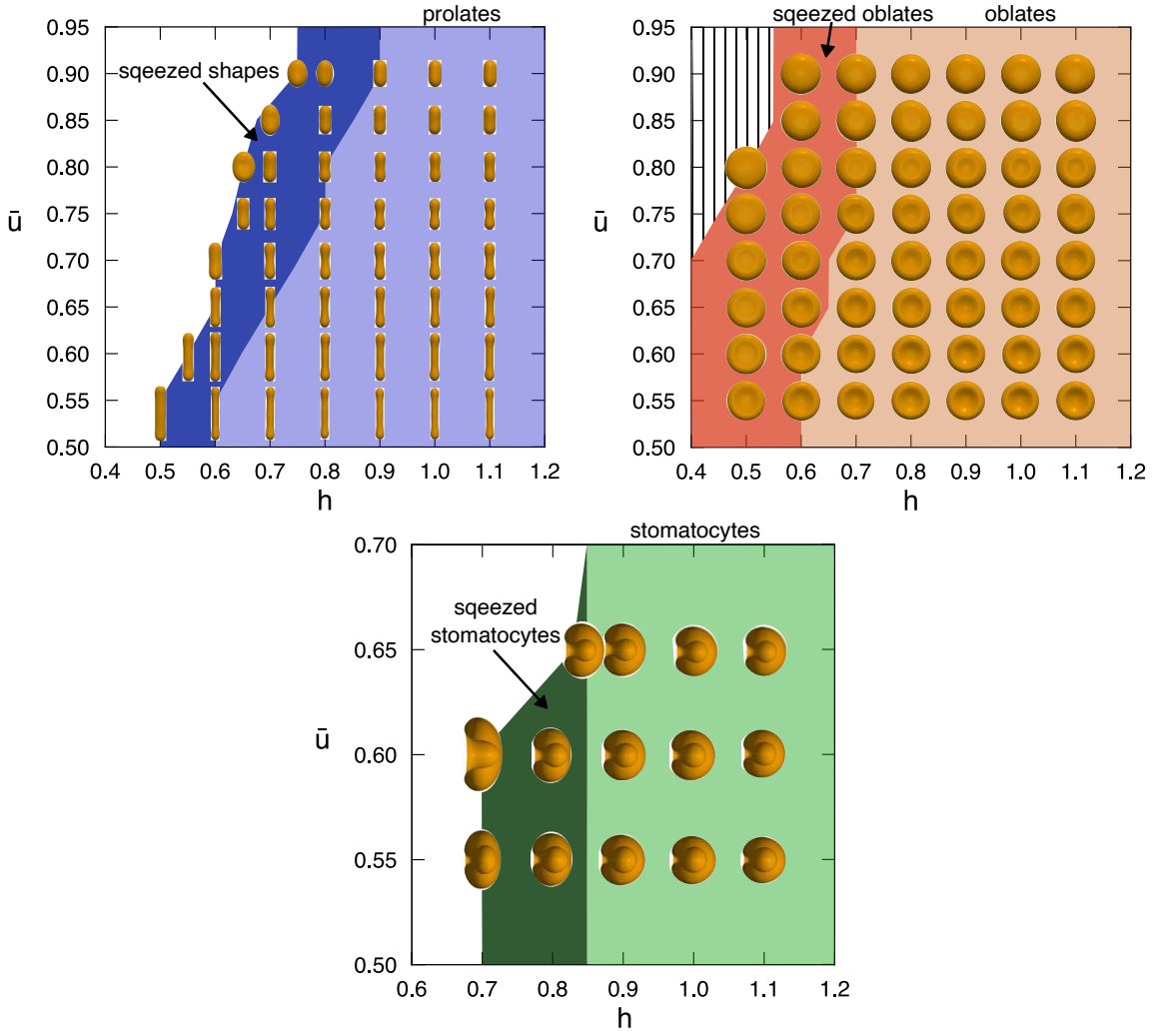


Figure 5.5: Stability diagrams of prolates, oblates, and stomatocytes inside a slit confinement. Shapes are organized on a $(h, \bar{u})$-grid. Highlighted regions represent distinct categories of shapes: light blue for prolates, dark blue for squeezed shapes (biaxial shapes) derived from prolates, light red for oblates, dark red for squeezed oblates, light green for stomatocytes, and dark green for squeezed stomatocytes. The hatched area in the oblate diagram designates where shapes diverge numerically and cannot exist. Shapes are converged to their minimum bending energy for all $(h, \bar{u})$.

We have plotted the bending energy versus slit confinement size h for $\bar{u} \in [0.55, 0.90]$ in Fig. 5.6(a)–(h). The prolate branch is represented by blue circles, the oblate branch by orange inverted triangles, and the stomatocyte branch by green squares. There are no stomatocyte data in Fig. 5.6(d)–(h), since for these $\bar{u}$ values the stomatocyte shapes are not stable (unless stabilized by an external potential). The points in Fig. 5.6(a), (b), and (d)–(f), where the bending energy curves of different branches intersect, represent discontinuous first-order phase transitions.

For $\bar{u} = 0.55$, prolates have higher bending energies, and a phase transition occurs at $h \sim 0.65$ where the stomatocyte and oblate branches intersect. The higher bending energy of prolates is still evident for $\bar{u} = 0.60$, but here the bending energies of the oblate and stomatocyte branches are closer, with a first-order phase transition around $h \sim 0.7$. For $\bar{u} = 0.65$, there are no intersections between the three main branches, but both stomatocytes and prolates reach their stability limits as they become more squeezed and deformed, transforming into oblates and squeezed oblates, respectively.

In the case of $\bar{u} = 0.70$, deformation of prolates results in biaxial shapes that possess higher bending energies until their stability limit is reached, at which point the shapes transform into squeezed oblates. The phase transition here is first-order, occurring at $h \sim 0.6$, where the prolate and oblate branches cross. For higher values of reduced volume, namely $\bar{u} = 0.75$ and $\bar{u} = 0.80$, the phase transition remains discontinuous (first-order), with the branch crossings positioned close to $h \sim 0.6$. To confirm the discontinuous nature, we performed numerical calculations with smaller increments of h, as shown in Fig. 5.6(e) and (f).

For $\bar{u} = 0.85$, the prolate and oblate branches transition more smoothly into each other (with additional data points at smaller increments of h provided to illustrate this), and the phase transition becomes continuous (second-order). This behavior is also observed when numerically calculating the two branches of shapes for $\bar{u} = 0.90$.

The phase diagram for the slit confinement is illustrated in Fig. 5.7, where abbreviated labels are used to denote different regions of the diagram. Here, "sob" stands for squeezed oblates, "ob" for oblates, "pr" for prolates, "sto" for stomatocytes, "ss" for squeezed shapes that result from deformed prolates (non-axisymmetric or biaxial), and "ssto" for squeezed

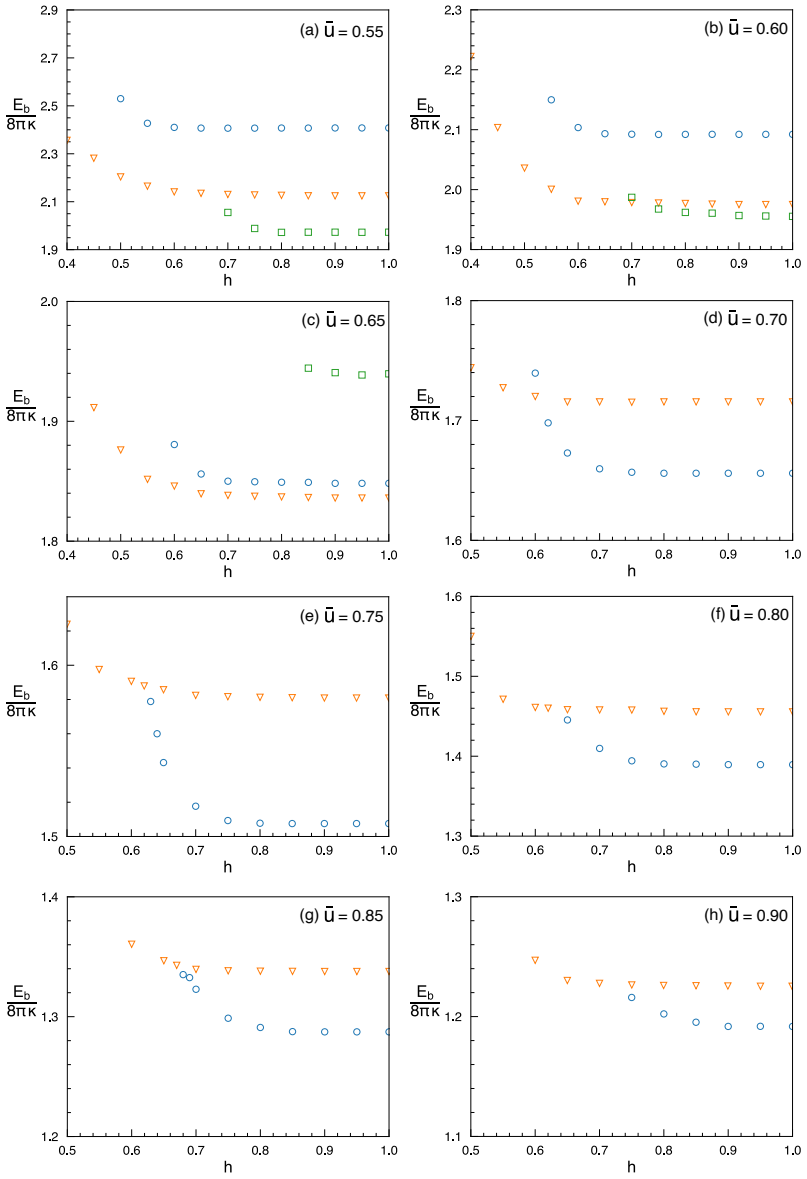


Figure 5.6: Bending energy (in units of $8\pi\kappa$) as a function of slit confinement size h for different values of the reduced volume $\bar{u}$ (a)–(h). The prolate branch is shown by blue circles, the oblate branch by inverted orange triangles, and the stomatocyte branch by green squares. Bending energies are the converged minimum value for each h.

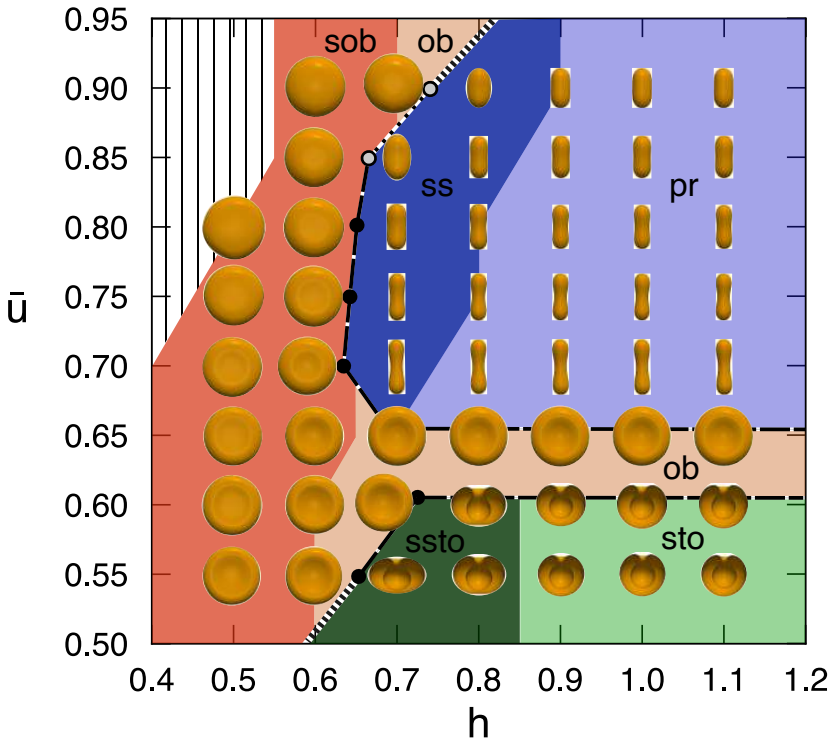


Figure 5.7: Phase diagram for vesicles in a slit confinement. Shapes are organized on a $(h, \bar{u})$-grid. Abbreviations denote different regions: "sob" for squeezed oblates, "ob" for oblates, "pr" for prolates, "sto" for stomatocytes, "ss" for squeezed shapes (resulting from deformed prolates), and "ssto" for squeezed stomatocytes. Large black dots and the dashed lines indicate discontinuous first-order phase transitions. Large gray dots and the dotted lines represent second-order phase transitions. Thick dotted lines extrapolate the phase boundaries into both lower and higher values of the reduced volume, at the bottom and top of the diagram. Shapes are converged to their minimum bending energy for all $(h, \bar{u})$.

stomatocytes, obtained from stomatocytes with their axial symmetry maintained through deformation. The color coding in the phase diagram follows that of the stability diagrams in Fig. 5.5.

The large black dots at five distinct $(h, \bar{u})$ coordinates in the diagram are extracted from Fig. 5.6(a), (b), and (d)–(f), which display the bending energy branches. These points mark

the loci of first-order (discontinuous) phase transitions, identified by intersections of the bending energy branches corresponding to different vesicle morphologies. Our numerical results indicate that such discontinuous transitions occur systematically for reduced volume values $\bar{u} < 0.85$ down to $\bar{u} \sim 0.65$. To delineate the corresponding phase boundaries, the discrete transition points are interpolated linearly, shown by thick dashed lines. The interpolant is further extended to connect with the horizontal dashed line reported by Seifert et al. [31], which represents the discontinuous prolate–oblate transition, behind the oblate shape at $(h = 0.70, \bar{u} = 0.65)$. This point of attachment is introduced as a reasoned extrapolation, consistent with the bending energy diagrams.

The large gray dots at $(h \sim 0.65, \bar{u} = 0.85)$ and $(h \sim 0.75, \bar{u} = 0.90)$ denote continuous second-order phase transitions, which are connected by a dotted line. The interpolation of this line is extended into the region above $\bar{u} = 0.90$ by a thick dotted line, representing a reasoned extrapolation based on the trajectory of the interpolants between the gray dots. The lower horizontal thick dashed line at $\bar{u} \sim 0.60$ marks the location of the discontinuous stomatocyte–oblate phase transition [31]. It connects to a black dot corresponding to the first-order transition from a "ssto" shape (dark green region) to an "ob" shape (light red region). A similar first-order transition is identified at $(h \sim 0.65, \bar{u} = 0.55)$. These black dots are interpolated and extended into the region below $\bar{u} = 0.55$ to delineate phase boundaries. The hatched area indicates the domain where our numerical results diverge and the squeezed or deformed shapes cease to exist.

5.3.3 Spherical Confinement

For the case of spherical confinement (see Fig. 4.12), we again examine the morphological changes of the three principal axisymmetric shapes: prolates, oblates, and stomatocytes. We also investigate the effect of imposing the bilayer area-difference constraint in our numerical calculations, as elaborated in Section 4.3.4, for a family of shapes with reduced area difference $\Delta a = 1.30$ and reduced volume within the range $[0.50, 0.75]$. However, at this stage we provide only preliminary bending energy diagrams, leaving more complete diagrams, along with stability and phase diagrams, to future work.

We start with prolates having a reduced volume range of $\bar{u} \in [0.55, 0.90]$ and place them

inside the spherical confinement cavity without constraining the center of mass. As the confinement size h is gradually reduced, the walls of the spherical cavity come into contact with the vesicle, deforming and squeezing it such that the prolate axial symmetry is broken. In Fig. 5.8, the stability diagram of prolates is illustrated by snapshots of shapes at specific $(h, \bar{u})$ coordinates. Two distinct regions are evident: the first, highlighted in light blue, corresponds to prolates with different $\bar{u}$ values that retain their unperturbed conformations; the second, highlighted in dark blue and labeled "squeezed shapes", contains the deformed configurations. We identify two distinct classes of squeezed shapes: (1) for $\bar{u} \leq 0.75$, deformation leads to bent shapes, and (2) for $\bar{u} \geq 0.80$, deformation produces biaxial squeezed shapes. At certain stability limits, designated by the border of the left side of dark blue region, these squeezed shapes, whether bent or biaxial, reach maximum bending energy and transition to a branch of higher- or lower-energy conformations depending on the value of $\bar{u}$. Two exceptions to this general behavior are observed at $\bar{u} = 0.60$ and $\bar{u} = 0.65$, where our numerical calculations indicate no transformation. Instead, the bent shapes adopt clam-like configurations for small h.

The stability diagram of oblates in Fig. 5.8 illustrates conformations with $\bar{u} \in [0.55, 0.90]$. The oblate shapes are obtained by squeezing and deforming prolates until they transform either into oblates ($\bar{u} = 0.90$) or into stomatocyte-like shapes ($\bar{u} = 0.70$, $\bar{u} = 0.75$, $\bar{u} = 0.80$ and $\bar{u} = 0.85$), after which the cavity size is increased to induce a transformation back to oblates. For $\bar{u} = 0.55$, $\bar{u} = 0.60$, and $\bar{u} = 0.65$, we directly place the corresponding free-space oblates inside the confinement cavity. The light red region with $h > 1.3$ contains oblate shapes that are not deformed by confinement. As the confinement size decreases, the cavity presses against the sides of the oblates, causing them to adopt a more cup-shaped morphology, where one depression becomes convex and the other more concave, accompanied by an increase in bending energy. This region is highlighted by dark red in the diagram and labeled "squeezed shapes". In addition, there is a region with $h < 1.25$ and $\bar{u} > 0.65$ where our numerical calculations reveal large fluctuations in both the bending energies and the conformations of the squeezed shapes. We highlight this area with light yellow and label it "unstable shapes".

The stomatocytes with $\bar{u} \in [0.55, 0.65]$ are placed directly inside the cavity. Reducing h compresses the stomatocytes. For $h < 1.0$ (see lower panel in Fig. 5.8), the shapes

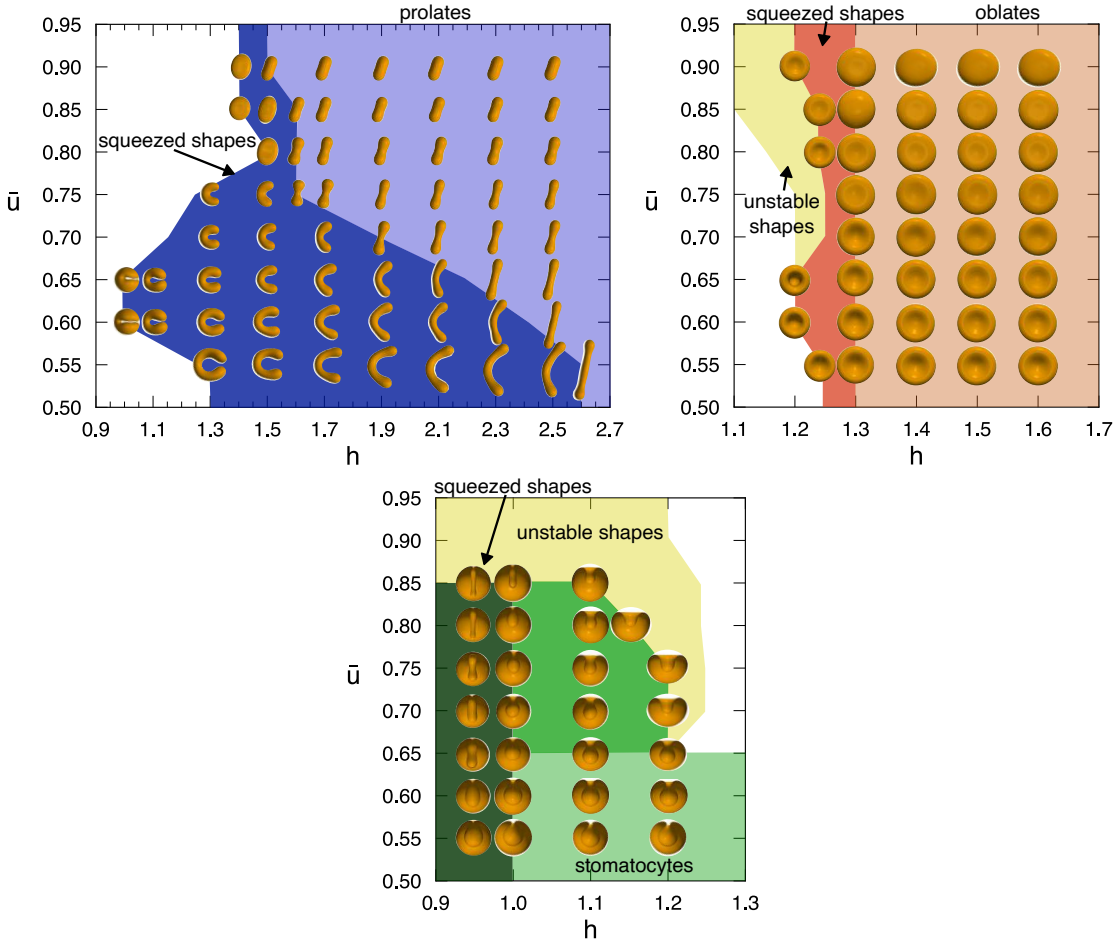


Figure 5.8: Stability diagrams of prolates, oblates, and stomatocytes inside a spherical confinement. Shapes are organized on a $(h, \bar{u})$-grid. Highlighted regions correspond to a distinct category of shapes: light blue for prolates, dark blue for squeezed shapes (biaxial and bent) originated from prolates, light red for oblates, dark red for squeezed cup-like shapes originated from oblates, light green for stomatocytes, green for confined stomatocyte-like shapes, and dark green for squeezed shapes originated from stomatocytes. The yellow areas in the oblate and stomatocyte diagrams designate regions where the shapes are unstable and fluctuate widely. Stable shapes are converged to their minimum bending energy for all $(h, \bar{u})$.

become strongly compressed, with their mouths narrowing and their interiors deforming. We highlight this region in dark green and label it "squeezed shapes". The light green region ($h > 1.0, \bar{u} < 0.65$) corresponds to free-space conformations of stomatocytes. The green-highlighted region denotes stomatocyte-like shapes that are stable only when the external potential of the confinement is present. Without confinement, these shapes are unstable in free space and lower their bending energy by transforming into oblates; we therefore refer to them as "confined stomatocytes". The light yellow region of the diagram contains shapes that, during numerical calculations, exhibit large fluctuations in both bending energy and conformation. When the cavity size is gradually increased, shapes with $\bar{u} > 0.65$ pass through this region before the fluctuations diminish and the conformations stabilize into oblates.

We have plotted the bending energy as a function of spherical confinement size h for $\bar{u} \in [0.55, 0.90]$ in Fig. 5.9(a)–(h). The prolate branch is represented by blue circles, the oblate branch by orange inverted triangles, and the stomatocyte branch by green squares. The points in Fig. 5.9 where the bending energy curves from different branches intersect correspond to discontinuous first-order phase transitions. In addition to these discontinuous transitions, several continuous (second-order) phase transitions are observed for $\bar{u} \leq 0.70$. For $\bar{u} = 0.55$, prolates exhibit the highest bending energies and remain metastable. As the confinement size decreases, the bent prolates reach their stability limit and transform into stomatocytes, which possess the lowest bending energy for this reduced volume. The same transformation occurs when an oblate with $\bar{u} = 0.55$ is sufficiently squeezed and deformed. The higher bending energy of prolates remains evident for $\bar{u} = 0.60$, but here the bending energies of the oblate and stomatocyte branches are closer, although no distinct crossing between these branches can be identified from the data. As noted earlier, the squeezed prolates for this reduced volume exhibit no stability limit; instead, a smaller confinement size merely produces a clam-like configuration. By contrast, deformation of the $\bar{u} = 0.60$ oblate branch under compression by the cavity walls drives the squeezed shapes to their stability limit, leading to a transformation into stomatocytes.

A notable feature of $\bar{u} = 0.60$, shown in Fig. 5.9(b), is the branch of shapes represented by red triangles. These shapes were obtained by increasing the cavity size to track the progression of configurations from the clam-like state. We interpret this as a locally stable

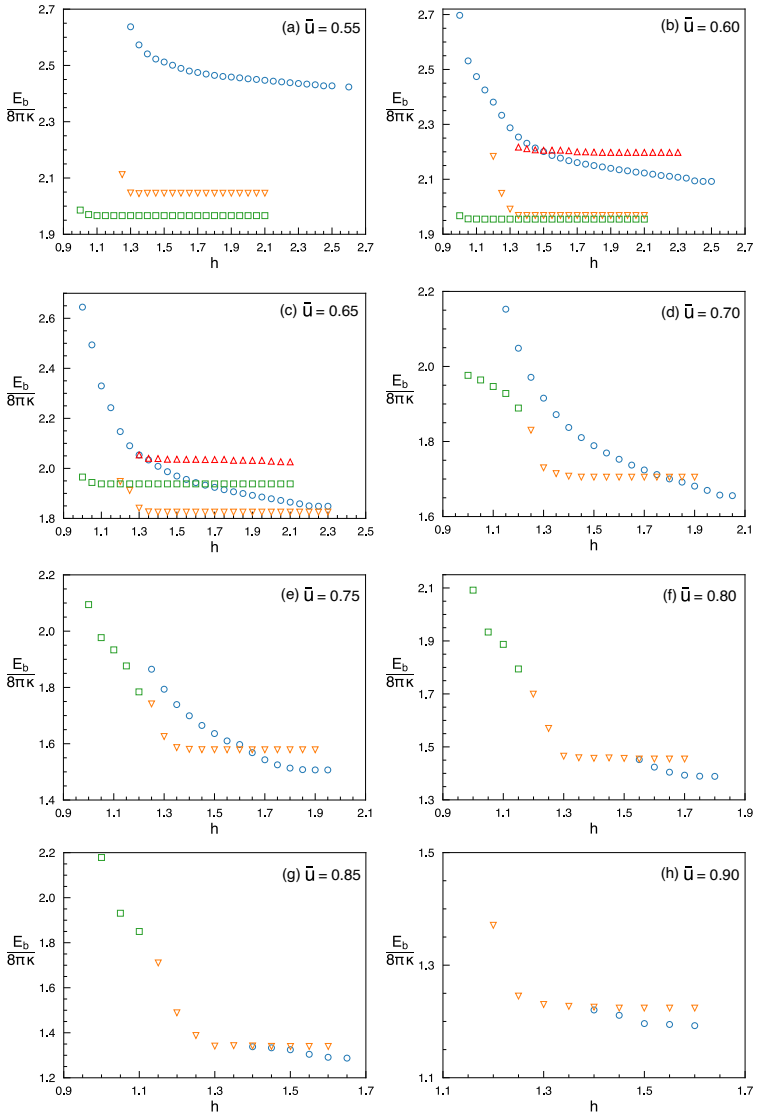


Figure 5.9: Bending energy (in units of $8\pi\kappa$) as a function of spherical confinement size h for different values of the reduced volume $\bar{u}$ (a)–(h). The prolate branch is denoted by blue circles, the oblate branch by inverted orange triangles, and the stomatocyte branch by green squares. Stable bent shapes are indicated by red triangles. Bending energies are the converged minimum value for each h.

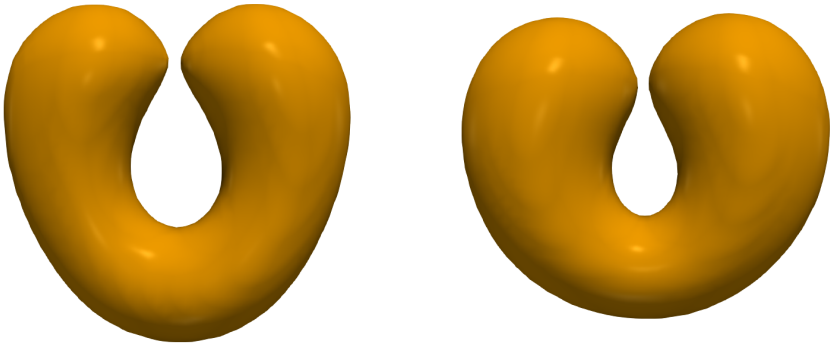


Figure 5.10: Metastable shapes with (a) $\bar{u} = 0.60$ and (b) $\bar{u} = 0.65$ obtained as the confinement size is increased to the free-space limit. The bending energies of these shapes are indicated by red triangles in the bending energy versus h diagrams.

branch of shapes (see Fig. 5.10(a) for a free-space snapshot), which intersects the prolate branch at $h \sim 1.5$, indicating a discontinuous first-order phase transition. A similar branch of shapes (see Fig. 5.10(b) for a free-space snapshot) was obtained for $\bar{u} = 0.65$ using the same procedure of increasing the cavity size from the clam-like configuration. These are also represented by red triangles in Fig. 5.9(c). In this case, the red-triangle branch merges more smoothly with the blue-circle prolate branch, suggesting a more continuous, second-order phase transition.

The other branches of shapes with $\bar{u} = 0.65$ cross each other at two separate points. The prolate branch crosses the stomatocyte branch at $h \sim 1.6$, and the oblate branch crosses the stomatocyte branch close to its stability limit at $h \sim 1.2$; both of these correspond to discontinuous (first-order) phase transitions. In the case of $\bar{u} = 0.70$, deformation of prolates results in bent shapes that exhibit higher bending energies until the stability limit is reached, where the highly bent shape at $h \sim 1.5$ transforms into a stomatocyte-like shape (confined stomatocyte). By subsequently increasing the cavity size, these unstable stomatocytes continuously transform into oblates.

There exists a narrow region of unstable and fluctuating shapes for confinement sizes $h \in (1.2, 1.25)$ where the bending energy vacillates widely. Nevertheless, we have selected

a representative bending energy value to include in the diagrams for $\bar{u} \leq 0.70$; even though the bending energy fluctuates, the confined stomatocyte–oblate transition remains continuous, as the two branches do not cross. A first-order phase transition is evident at $h \sim 1.8$, where the prolate and oblate branches intersect.

For higher values of the reduced volume, namely $\bar{u} = 0.75$ and $\bar{u} = 0.80$, both types of phase transitions are present: (1) prolate–oblate first-order transitions with branch crossings at $h \sim 1.6$ and $h \sim 1.5$, respectively; and (2) confined stomatocyte–oblate second-order transitions at $h \sim 1.2$ and $h \sim 1.15$, respectively (see Fig. 5.9(e) and (f)). For $\bar{u} = 0.85$, both the confined stomatocyte–oblate and the prolate–oblate transitions exhibit continuous characteristics, indicating that the phase transitions are of second-order nature. This behavior persists for $\bar{u} = 0.90$, based on our numerical calculations. However, the confined stomatocyte branch is unstable and displays large fluctuations; therefore, we have only included data for oblates and prolates in Fig. 5.9(h).

The phase diagram for the spherical confinement is depicted in Fig. 5.11, where we use abbreviated labels to denote different regions of the diagram. Here, "consto" stands for confined stomatocytes, "ob" for oblates, "pr" for prolates, "sto" for stomatocytes, and "ss" for squeezed shapes, which subsumes squeezed shapes resulting from deformed prolates, oblates, and both free-space and confined stomatocytes. The color code in the phase diagram follows that of the stability diagrams in Fig. 5.8. We also retain the label "unstable" from the stability diagrams to designate the region where the numerical calculations indicate unstable and fluctuating shapes.

The large black dots at four distinct $(h, \bar{u})$ coordinates on the diagram represent points where first-order transitions occur in the bending energy vs. confinement size diagrams shown in Fig. 5.9(c)–(f). From our numerical calculations, these first-order phase transitions occur between prolates and oblates for reduced volume values $\bar{u} < 0.85$ down to $\bar{u} \sim 0.65$. The dots are connected by linear interpolation, depicted by thick dashed lines, to delineate the approximate boundaries of different phases separated by a discontinuous (first-order) transition. The interpolation is further connected to the horizontal dashed line [31]—representing the discontinuous prolate–oblate transition—behind the oblate shape at $(h = 2.1, \bar{u} = 0.65)$, where we make an educated guess of the point of connection.

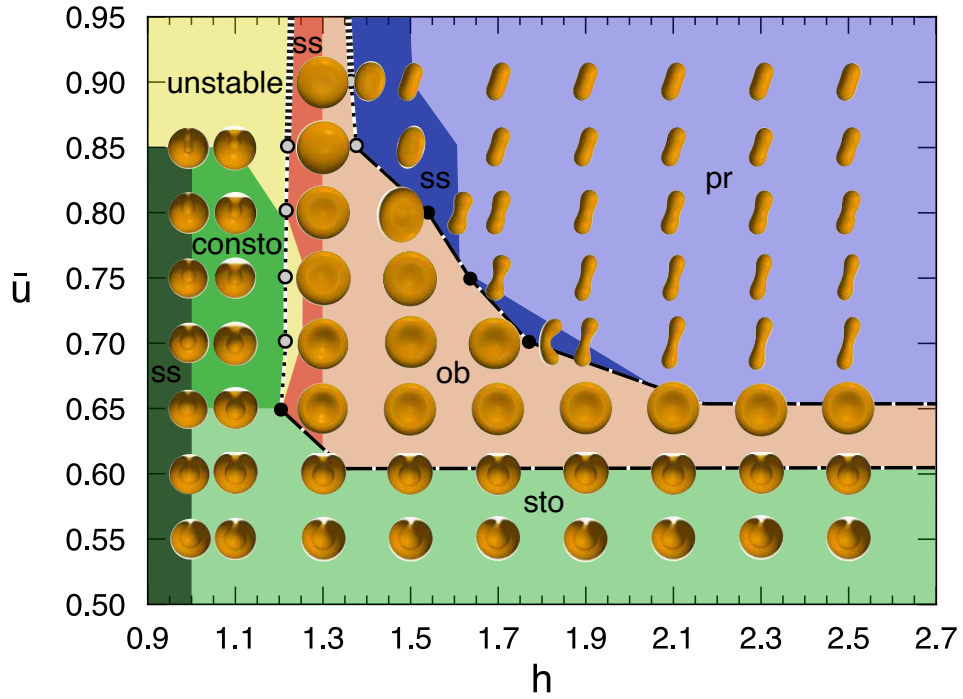


Figure 5.11: Phase diagram for vesicles in a spherical confinement. Shapes are organized on a $(h, \bar{u})$-grid. Abbreviations denote distinct regions: "consto" for confined stomatocytes, "ob" for oblates, "pr" for prolates, "sto" for stomatocytes, and "ss" for squeezed shapes, which include deformed prolates, oblates, and both free-space and confined stomatocytes. Large black dots and dashed lines indicate discontinuous first-order phase transitions. Large gray dots and dotted lines represent continuous second-order phase transitions. Thick dotted lines extrapolate phase boundaries into higher values of the reduced volume at the top of the diagram. Stable shapes are converged to their minimum bending energy for all $(h, \bar{u})$.

The four large gray dots located in the region where the squeezed shapes of the oblate branch, the unstable shapes, and the confined stomatocytes appear represent continuous shape transitions, characteristic of second-order phase transitions. Two additional gray dots, at $(h \sim 1.4, \bar{u} = 0.85)$ and $(h \sim 1.4, \bar{u} = 0.90)$, likewise denote continuous second-order transitions, but between the squeezed shapes of the prolate branch and the oblates.

All gray dots are connected by linear interpolations, shown as dotted lines in the phase diagram. The interpolated boundary delineating the oblate and deformed-oblate phases is further extended into the region above $\bar{u} = 0.90$ with thick dotted lines, serving as an educated extrapolation that follows the trajectory of the interpolants. The lower horizontal thick dashed line at $\bar{u} \sim 0.60$ corresponds to the discontinuous stomatocyte–oblate transition [31]. This line joins the dashed line representing the first-order transition from an "ss" shape of the oblate branch (dark red region) to the "sto" phase (light green region). The position of this connection has been determined by an educated guess, based on inspection of the bending energy diagrams and evaluation of the h values at which confinement-induced compression raises the bending energy at $\bar{u} = 0.65$, followed by extrapolation to lower $\bar{u}$ values.

As mentioned at the beginning of this section, we examined the effect of imposing the bilayer area-difference constraint in our numerical calculations for vesicle morphology inside spherical confinement. Owing to the sheer number of possible configurations, we restricted our analysis to a single value of the reduced area difference, namely $\Delta a = 1.30$, while still considering a range of reduced volumes within $[0.50, 0.75]$.

The primary objective here is to investigate the three-dimensional morphologies of vesicles that must simultaneously satisfy the area-difference constraint throughout the confinement process. Accordingly, we have limited the results to bending energy versus confinement size diagrams (see Fig. 5.12), leaving more comprehensive stability and phase diagrams, as well as a broader exploration of parameter space, to future work.

We have illustrated snapshots of three-dimensional shapes within the bending energy diagrams, positioned close to the markers that represent their corresponding numerical bending energy values. The initial configurations for these simulations are the so-called starfish ($\bar{u} = 0.50$ and $\bar{u} = 0.55$), racket ($\bar{u} = 0.60$), dumbbell prolates ($\bar{u} = 0.65$ and $\bar{u} = 0.70$), and pear (lopsided dumbbell) ($\bar{u} = 0.75$) [31, 74, 35]. The energy diagrams in Fig. 5.12(a) and (b) show the bending energy variations of starfish shapes. In both cases, decreasing h causes two arms of the vesicles to deform and merge. At $h \sim 1.5$, the resulting shapes exhibit a single arm and a large head, resembling a hammer-like morphology. With further reduction in confinement size, the arm shortens while the overall structure bends, and a connecting membrane forms between the two sides ($h \sim 1.3$). At

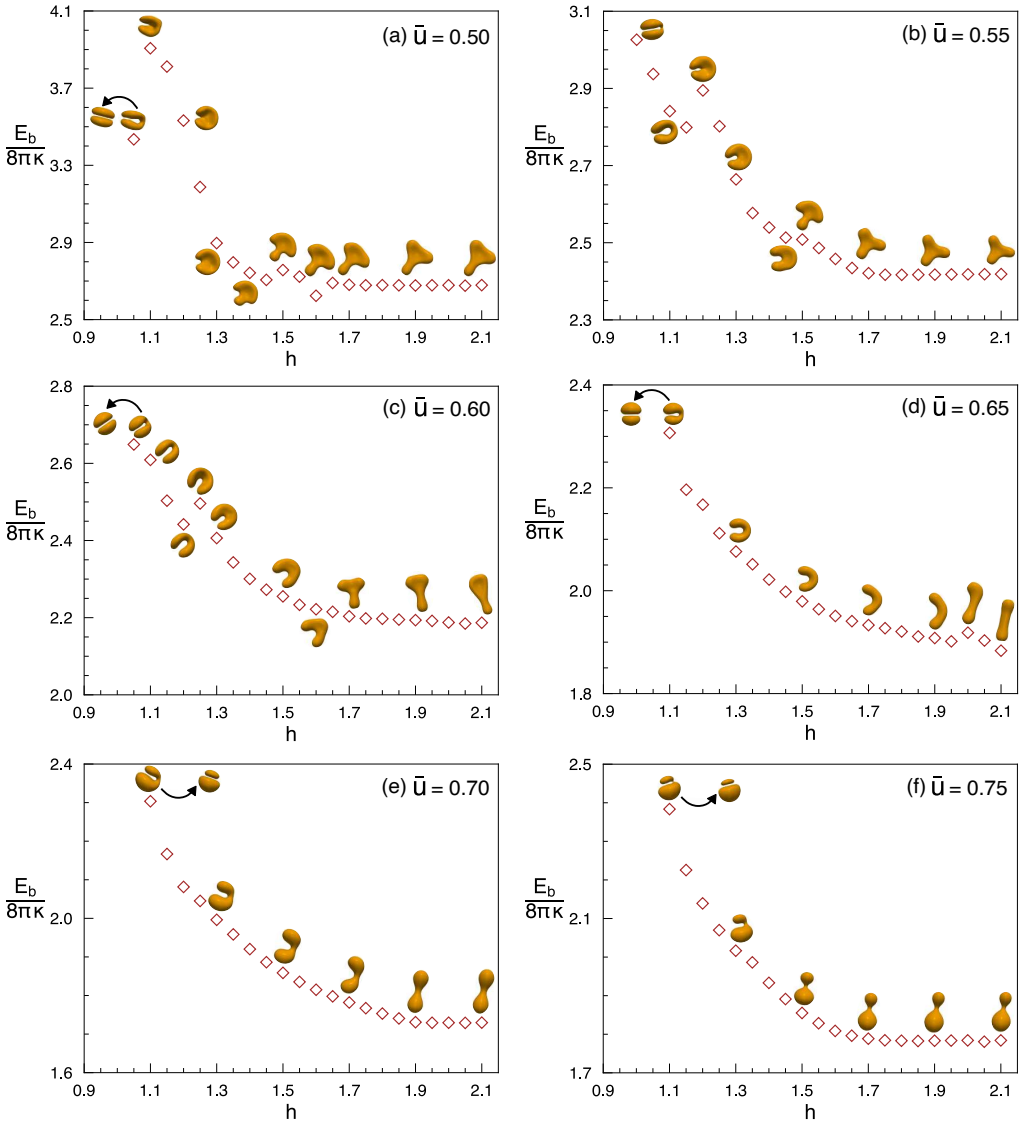


Figure 5.12: Bending energy (in units of $8\pi\kappa$) vs. spherical confinement size h for reduced area difference $\Delta a = 1.30$ and different values of the reduced volume $\bar{u}$ (a)–(f). The vesicle shapes are illustrated adjacent to the markers representing their bending energy values. Curved arrows indicate shape division events, where a single vesicle splits into separate shapes. Bending energies are the converged minimum value for each h.

$h \sim 1.1$ for $\bar{u} = 0.50$ and $h \sim 1.2$ for $\bar{u} = 0.55$, a stability limit is reached, accompanied by a noticeable drop in bending energy. At this point, the connecting membrane in the center disappears, and the shapes transform into clam-like conformations, with two similarly sized valves connected by a narrow neck. Reducing h below 1.0 causes the neck to become very thin and eventually rupture, leading to the formation of two disjoint vesicles. These transformations are indicated in the diagrams by curved arrows. However, the bending energy of these divided shapes is not plotted, since their Euler characteristic differs from that of the initial configurations and the Gaussian curvature contribution to the Helfrich bending energy must therefore be included.

For the case of $\bar{u} = 0.60$ in Fig. 5.12(c), the initial configuration, resembling a racket, develops two additional arms and transforms into a starfish at $h \sim 1.7$. Further reduction of h causes one of the arms to disappear while the other two bend, and a small connecting membrane forms between them. A stability limit at $h \sim 1.25$ can be identified in the diagram, where a slight drop in bending energy occurs for smaller values of h. The vesicle then adopts a clam-like morphology with a thin neck connecting the valves. For $h < 1.0$, the neck eventually ruptures, leading to the formation of disjoint shapes.

At $\bar{u} = 0.65$, the initial shape assumes a prolate configuration. Compression under smaller confinement sizes causes the prolate to bend and deform, but no clear stability limit is apparent in the diagram, and the transition to the clam-like conformation appears smoother. As before, further reduction of h results in the formation of separate shapes, although in this case one of the disjoint vesicles is slightly smaller than the other. Similar transformations are observed for $\bar{u} = 0.70$ and $\bar{u} = 0.75$, although the size symmetry between the valves of the clam-like shapes and their final disjoint forms becomes more pronounced as the reduced volume increases.

5.3.4 Cubic Confinement

The cubic confinement can be regarded as an arrangement of three slit confinements, oriented mutually perpendicular in 3D space, thereby forming a cubic cavity between them. Unlike the spherical confinement, which possesses complete rotational symmetry, a cubic confinement only exhibits rotational symmetry along certain directions and for

specific angular rotations. Moreover, similar to the spherical confinement, this type of hard-wall confinement fully encloses the vesicle within its interior, in contrast to the tube and slit confinements. In this section, we examine the behavior of prolate shapes with $\bar{u} \in [0.55, 0.90]$ in a cubic confinement. As the confinement size h decreases in small increments, we calculate the 3D shapes and bending energies of the prolates using the NN solver. When $h = 0.8$ (the side length of the confinement in units of R_0), we reverse the procedure and gradually increase the confinement size in small increments; during this process the calculated shapes may converge to a different class of configuration compared to those obtained during confinement size reduction. Both the shapes and their bending energies are shown in Fig. 5.13(a)–(h).

Figure 5.13(a) illustrates the shape transformations of a prolate with $\bar{u} = 0.55$. As h decreases, the vesicle first orients itself along the 45° direction and, with further reductions in h, reorients along the diagonal of the cavity. This behavior, where the vesicle reorients toward free space, is observed for all higher values of the reduced volume as well. The vesicle avoids deformation and a rise in bending energy by reorienting until no additional free space remains available. At $h \sim 1.7$, the prolate shape begins to deform and bend. This deformation continues, and at $h \sim 1.0$, the vesicle bends at three points: its center and two additional points on either side of the center. At lower h, the thicker ends of the vesicle deform into cuboidal valves of a clam-like shape, connected by a thin neck. Increasing h back to its initial value yields the same shapes observed during the forward trajectory. Thus, no stability limit or shape transformation to a different branch of configurations is observed.

At $\bar{u} = 0.60$, a similar trajectory of shape conformations is observed for prolates (see Fig. 5.13(b)). After reorientation along the diagonal of the cubic cavity, bending deformations begin at $h \sim 1.5$ and lead to a clam-like shape with cuboidal valves at $h \sim 0.8$. Increasing the cavity size, however, produces a different branch of shapes: this can be attributed to the reorientation of the vesicle along the 45° direction at $h \sim 1.0$, where a small arrow connects the data point to the corresponding shape. These shapes are represented by orange inverted triangles, as they are a continuation of oblates. As shown, the vesicle morphs into a cuboidal oblate at $h \sim 1.1$, which becomes progressively more circular as the confinement size increases. Eventually, the vesicles settle into free-space oblates, which

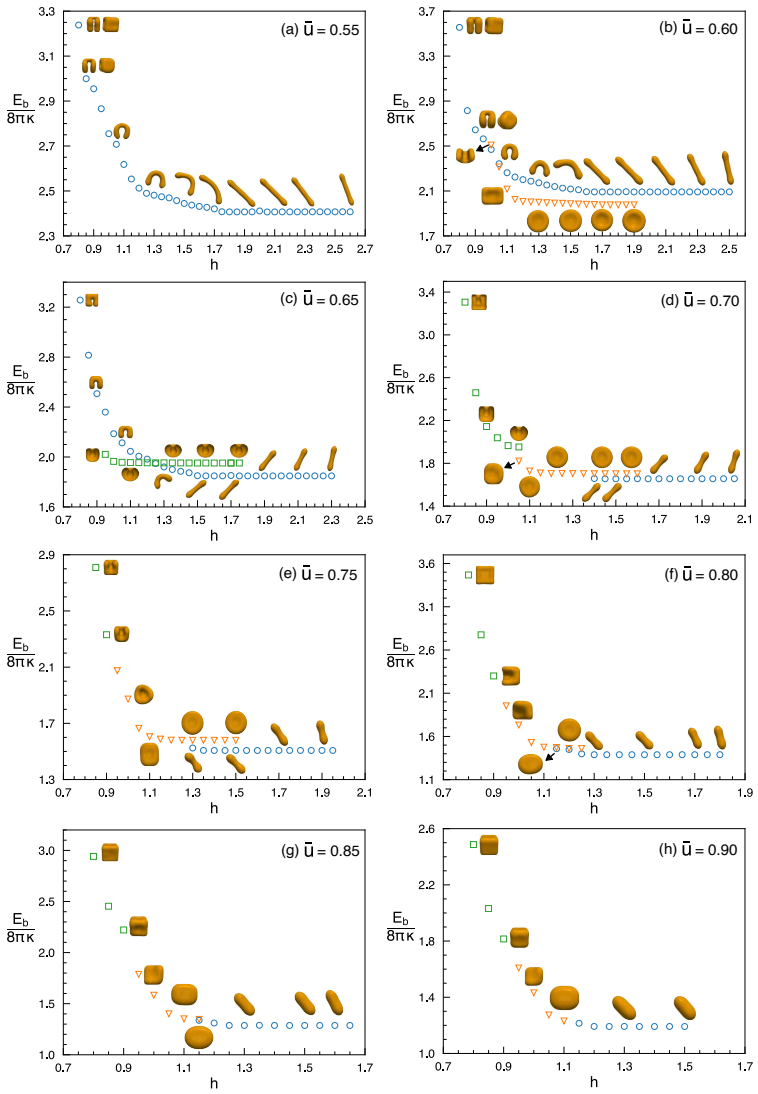


Figure 5.13: Bending energy (in units of $8\pi\kappa$) vs. cubic confinement size h for different values of the reduced volume $\bar{u}$ (a)–(h). The prolate branch is indicated by blue circles, the oblate branch by inverted orange triangles, and the stomatocyte and cubic-shape branches by green squares. Snapshots of representative vesicle morphologies are shown adjacent to the markers corresponding to their bending energy values. Bending energies are the converged minimum value for each h.

exhibit lower bending energies than their prolate counterparts. The point at $h \sim 1.0$ where these branches of shapes cross one another exhibits the characteristics of a first-order phase transition.

Raising the reduced volume to $\bar{u} = 0.65$ changes the configuration of the shapes at lower h. In particular, for $h \sim 0.9$, the vesicle adopts a cubic configuration, with its sides conforming to the cavity and a gap running across the shape from one side to the other. When the confinement size is increased, this configuration undergoes a drop in bending energy at $h \sim 0.9$ and transforms into a deformed stomatocyte (cut through the mirror plane to reveal the interior), which we have indicated by green square markers in Fig. 5.13(c). Further increase in h leads to free-space stomatocytes, which exhibit higher bending energies than their prolate counterparts at this reduced volume. The point at $h \sim 1.3$, where the two branches of shapes intersect, can be characterized as a first-order phase transition.

Starting from $\bar{u} = 0.70$, the prolate shapes no longer exhibit bending as the confinement size is reduced. This differs from the behavior observed in the spherical confinement, where bending modes appear for both $\bar{u} = 0.70$ and $\bar{u} = 0.75$ but disappear for $\bar{u} \geq 0.80$. Here, at $h \sim 1.35$, the prolate branch reaches its stability limit and transforms into oblates with slightly higher bending energy; the crossing point of the two branches exhibits the characteristics of a first-order phase transition. Further reduction in confinement size leads to another stability limit for the oblate branch at $h \sim 1.0$, where a deformed cuboidal oblate jumps to the stomatocyte branch at a slightly higher bending energy. The cubic confinement strongly deforms stomatocytes in the lower-h region. Increasing the confinement size from this regime leads to the formation of confined stomatocyte-like shapes (around $h \sim 1.05$), similar to those discussed in the spherical confinement case. However, these shapes are unstable without the external confinement potential and, once the confinement size exceeds $h \sim 1.1$, they transform into lower-energy oblates and remain within this branch. The branches of stomatocyte-like shapes and oblates appear to intersect near $h \sim 1.0$, where the discontinuous behavior again suggests a first-order phase transition.

For $\bar{u} = 0.75$, the transition from prolates to oblates occurs at $h \sim 1.25$, also consistent with a discontinuous first-order transition. Further squeezing of oblates produces a deformed cuboidal oblate at $h \sim 1.1$ with a square outer contour. At $h \sim 1.0$, this shape

becomes cup-like but, owing to the cubic cavity, develops three prominent corners. Below $h \leq 0.9$, the shapes continuously transform into cubic-like vesicles with a small gap and a hole oriented along the 45° direction (see the leftmost region of Fig. 5.13, where these shapes are depicted and their bending energies are marked with green squares). Increasing the confinement size again retraces the oblate branch into the large-h region, where the shapes remain within the oblate family.

The energy diagrams in Fig. 5.13(f)–(h) ($\bar{u} = 0.80$, $\bar{u} = 0.85$, and $\bar{u} = 0.90$) exhibit consistent features in the sequence of morphological transformations. The transition from prolates to oblates proceeds continuously and is thus characterized as a second-order transition. A similar continuous behavior is observed for the transition from oblates to cubic morphologies. At sufficiently small confinement sizes (h), the vesicle adopts a fully cubic configuration devoid of gaps or perforations. This cubic morphology has been reported previously in theoretical studies, where it was described as a quadriconcave conformation resembling Knizocytes observed experimentally [34].

When the confinement size is gradually increased from these low-h states, the vesicle retraces the morphological sequence in reverse, reaffirming the stability of the transformation pathway. Notably, for $\bar{u} = 0.85$ and $\bar{u} = 0.90$, the oblate configurations at $h \sim 1.1$ exhibit slight elongation due to confinement-induced deformation, which energetically biases them toward relaxation into the prolate branch. This behavior corresponds to a continuous, second-order transition, underscoring the role of confinement geometry in influencing the stability of competing morphologies.

5.4 Discussion

The confinement studies of phospholipid vesicles modeled with the phase-field formulation of the Helfrich model offer a systematic route toward constructing detailed energy, stability, and phase diagrams. Our NN solver provides a robust, scalable, and versatile computational framework, capable of generating both symmetric and asymmetric shapes. Within this setting, the boundaries between shape categories and phase regions can be delineated, and the nature of the associated phase transitions can be systematically classified.

Different types of confinement can give rise to non-axisymmetric morphologies, one of the most notable being biaxial conformations. This category of shapes can emerge in all four types of confinement; however, a broader range of biaxial shapes across different reduced volumes is produced in cylindrical (tube) and slit confinements. In the case of tube confinement, symmetry breaking that leads to biaxial conformations originates from oblate initial shapes, which, upon decreasing the confinement size, are squeezed and deformed into biaxial shapes. By contrast, when the initial shape is prolate, biaxial conformations arise more readily under slit confinement.

It is also worth noting that biaxial shapes obtained by squeezing oblates in a tube transform into prolates at smaller confinement sizes for lower values of $\bar{u}$. Examination of the stability diagram in Fig. 5.2 reveals that, before this transition, the shapes are elongated along one axis at low $\bar{u}$. In contrast, for slit confinement, the transition from deformed prolates to oblates exhibits a more discontinuous character at low $\bar{u}$ and becomes smoother (continuous) at higher $\bar{u}$, consistent with a second-order phase transition (see Fig. 5.5). Thus, to obtain a wider range of biaxial shapes with smoother prolate–oblate or oblate–prolate transitions, vesicles should have $\bar{u} < 0.65$ in the case of tube confinement and $\bar{u} > 0.80$ for slit confinement.

Another category of shapes arises when prolates are compressed at their ends and bent within spherical and cubic confinements. In spherical confinement, these bent shapes appear for higher values of the reduced volume, $\bar{u} \leq 0.75$, whereas in cubic confinement they occur for $\bar{u} \leq 0.65$. This difference can be attributed to the geometry of the confinement: in a cubic cavity, the ends of the prolate vesicle become trapped in two opposite corners along the diagonal, which facilitates bending. For larger reduced volumes, such as $\bar{u} = 0.70$ and $\bar{u} = 0.75$, the bending energy of free-space prolates is slightly lower than that of oblates; however, due to small deformations as the confinement size decreases, prolates preferentially transform into oblates. In spherical confinement, by contrast, the ends of prolates are free to move and slide along the inner surface of the cavity, making the prolate–oblate transformation energetically favorable at larger $\bar{u}$.

Additionally, in spherical confinement, when the cavity size is increased from small h, we observe bent shapes at $\bar{u} = 0.60$ and $\bar{u} = 0.65$ that remain stable in free space. These configurations likely correspond to states where the bending energy is trapped in local

minima and are therefore metastable.

For spherical confinement, the vesicle shapes obtained at small confinement sizes ($h \leq 1.0$, also referred to as the strong confinement limit) are consistent with those reported in earlier numerical studies [36, 76, 37, 77] and experimentally observed morphologies [37]. The same agreement holds for the shapes we obtained in the small-h regime when the bilayer area difference constraint was incorporated into the bending energy minimization. In particular, the emergence of clam-like conformations, their subsequent division, and the formation of two distinct daughter vesicles (see Fig. 5.12) have all been observed in previous numerical and experimental works [37, 77]. Our numerical results and three-dimensional shape solutions, obtained using the proposed NN solver, not only corroborate these findings but also extend them by providing a framework for generating such confined morphologies directly from free-space axisymmetric conformations. This approach further reveals intermediate shapes that exist between the free-space and strongly confined regimes.

We observed that when sufficient free space is available inside the confinement, vesicle shapes tend to reorient themselves along directions that preserve their bending energy. This property emerges intrinsically from the NN solver and is not imposed or externally controlled. A prime example is the reorientation of prolates along the diagonal of the cubic confinement before undergoing any deformation, as discussed earlier. Similar reorientation behavior has also been observed in other confinement geometries, although we have not provided detailed numerical results here. For instance, when oblates with different reduced volume values are initially placed inside a cylindrical confinement such that their long axis is perpendicular to the tube's axis (i.e., blocking the tube), they reorient along the tube's axis as the confinement size is reduced, before being compressed and deformed into biaxial shapes.

A salient feature observed in the bending energy diagrams presented in Figs. 5.3, 5.6, 5.9, and 5.13 is the presence of hysteresis effects: starting from a particular shape and decreasing the confinement size, followed by reversing the process and increasing the size, often results in final conformations that differ from the initial ones.

The phase diagrams in Figs. 5.4, 5.7, and 5.11 describe the different shape phases obtained from our numerical calculations. We have delineated the phase boundaries by linear

interpolation and classified the types of phase transitions by examining the corresponding bending energy diagrams. The dominant type of phase transition identified in these diagrams is discontinuous and therefore of first-order character. For $\bar{u} \geq 0.85$, in both slit and spherical confinements, the prolate–oblate (or oblate–prolate) transition exhibits a more continuous behavior: the shapes evolve through a sequence of biaxial intermediates rather than undergoing abrupt discontinuous changes (the bending energies of the two family of shapes merge smoothly). A distinct series of continuous, or second-order, transitions is also observed between squeezed cup-shaped conformations and confined stomatocytes in spherical confinement, specifically for $\bar{u} > 0.65$. Notably, the region near the boundary between these phases contains unstable shapes, which according to our numerical results exhibit large fluctuations in both their bending energies and morphologies.

The results presented for spherical confinement with the area-difference constraint are based on the bilayer-coupling model [73, 31], which is a special limit of the more general area-difference-elasticity model [108, 155]. A more comprehensive picture of shape changes and transitions—sufficient to construct full phase diagrams—requires the implementation of the area-difference-elasticity model within our NN solver framework.

The cubic confinement studies can likewise be extended to include a broader range of shapes, thereby enabling the construction of stability and phase diagrams. We leave these directions to potential future work.

Chapter 6

Discussion and Conclusion

In this chapter, we reflect on the results obtained in this thesis, especially Chapters 4 and 5, where we introduced and implemented a neural network (NN) solver for the phase-field formulation of the Helfrich model and applied it to study phospholipid vesicles under various confinement conditions. We discuss the accomplishments and implications of this work, its relationship to the literature, its limitations, and prospects for future research. Throughout, we retain the notation established earlier: reduced volume $\bar{u} = 3V/4\pi R_0^3$, reduced area difference Δa, and interface parameter ϵ with $\bar{\epsilon} = \epsilon/R_0$.

6.1 Summary of Contributions

Phase-field reformulation of the Helfrich curvature model. We adopted a phase-field representation $\phi(\mathbf{r})$ for the vesicle morphology and rederived an expression for the mean curvature $H[\phi]$ and the Helfrich energy $E_b[\phi]$ (cf. Appendices A and B). This mapping avoids explicit surface tracking and thus circumvents mesh entanglement and remeshing, well-known challenges in triangulation and finite-element surface formulations.

Neural-network solver for constrained variational minimization. Instead of evolving ϕ via a PDE (e.g., Model A/B flows) or discretizing a surface, we parameterized $\phi(\mathbf{r}; \Theta)$

by a compact feedforward NN and minimized a *parametric* cost functional (4.6) with Lagrange multipliers updated by ascent. The spatial derivatives ($\nabla\phi$, $\nabla^2\phi$) are computed by automatic differentiation, eliminating the finite-difference truncation error. This preserves the diffuse-interface advantages of the phase-field framework while dramatically simplifying differentiation and constraint enforcement.

Validation against canonical free-space branches. We reproduced the classic bending energy vs. $\bar{u}$ diagram (see Fig. 4.8(d)) and the three principal free-space branches (prolate, oblate, stomatocyte), finding close agreement with the results of the axisymmetric shooting-method results [31] and previous phase field calculations [48, 49]. Minor deviations along the flattest oblate shapes were traced to the finite interface width $\bar{\epsilon}$.

Systematic confinement studies and phase maps. Across cylindrical (tube), slit, spherical, and cubic confinements we computed stability diagrams, bending-energy curves versus confinement size h, and consolidated phase diagrams. We identified both discontinuous (first-order) and continuous (second-order) transitions, non-axisymmetric intermediates (biaxial and bent states), and regions of numerical/physical instability (large energy fluctuations) near symmetry-breaking boundaries (as in the up-down symmetry of oblates and the lack of it in stomatocyte-like shapes). For spherical confinement, we additionally examined families with fixed reduced area difference Δa and documented the emergence of starfish-like, clam-like, and division-prone morphologies.

Compact representation and reusability. Once the NN solver converges, the optimized set of network parameters Θ provides a compact, self-contained representation of a vesicle shape. Because Θ uniquely determines the phase field $\phi(\mathbf{r};\Theta)$, and therefore the full three-dimensional morphology together with its bending energy and constraint values, it can be viewed as a *shape certificate*: a minimal numerical object that certifies the existence of a particular equilibrium solution of the constrained Helfrich problem.

This representation is significantly more economical than storing full surface meshes or volumetric fields, and it is directly reusable. In practice, solutions at nearby points

in parameter space—e.g., for slightly different reduced volume $\bar{u}$, confinement size h, and reduced area difference Δa—are obtained efficiently by initializing the solver with a previously converged Θ. This continuation strategy allows entire branches of shapes to be traversed systematically, which enables the construction of reproducible shape families, bending-energy curves, and phase diagrams with modest storage requirements and practical training times.

6.2 Interpretation of Key Findings

6.2.1 Biaxial and bent intermediates under confinement

Cylindrical and slit confinements. For tube confinement, symmetry breaking from oblate to biaxial shapes precedes prolate capture at lower h, with first-order jumps marked along the oblate→prolate boundary (see Fig. 5.4). In slit confinement, the squeezing of prolates induces biaxial intermediates whose energetic crossing with the oblate branch traces a prolate→oblate boundary that evolves from first order at lower $\bar{u}$ to more continuous at higher $\bar{u}$ (see Fig. 5.7). These results rationalize how confinement geometry selects principal axes and narrows the permissible curvature spectrum as h decreases.

Spherical confinement. The spherical cavity penalizes excursions orthogonal to the cavity wall, driving bent-prolate intermediates at moderate $\bar{u}$ and transitions toward stomatocyte-like states as h is reduced (see Fig. 5.8). The coexistence of first-order (prolate–oblate) and second-order (confined-stomatocyte–oblate) boundaries (see Fig. 5.11) reflects different curvature pathways: branch crossings signal energetic exchange between distinct basins, whereas smooth connections indicate the persistence of a single basin deformed by confinement.

Cubic confinement. In cubic cavities, vesicles exploit rotational degrees of freedom to minimize energy cost before deformation, reorienting to diagonals. At smaller h, shape families progress toward cuboidal oblates and fully cubic states without holes (Fig. 5.13).

The geometry pins local curvature at edges and corners, suppressing axisymmetry and favoring square-valve, clam-like intermediates. The observed hysteresis when cycling h reflects multistability across nearby basins with shallow barriers.

6.2.2 Area difference and division-prone morphologies

Imposing a fixed Δa (§4.3.4) in spherical confinement yields starfish→hammer→clam-like trajectories with neck thinning and eventual division into separate components at strong confinement (Fig. 5.12). This aligns qualitatively with previous experimental and numerical reports on invagination and multi-lobed morphologies under excess area and confinement [37, 77]. Our framework captures these transitions within the same parametric optimizer used for free-space and other confinements, underscoring the solver's flexibility.

6.2.3 Energetic trends and phase boundaries

Across all geometries, squeezed states typically incur rising $E_b/(8\pi\kappa)$ with decreasing h, reaching a stability limit where a discontinuou jump or a smooth connection occurs. The location and nature of these boundaries depend on $(\bar{u}, \Delta a, h)$ and on geometric pinning by the confinement. Our phase diagrams (Figs. 5.4, 5.7, 5.11) assemble these trends into interpretable maps, useful for experimental design (e.g., predicting which shapes arise upon narrowing channels or cavities).

6.3 Relation to Prior Work

Helfrich theory and axisymmetric shapes. Our free-space results reproduce the canonical prolate/oblate/stomatocyte branches and the E_b–$\bar{u}$ dependence originally obtained by a shooting method and ODE reductions for the two-dimensional contour of axisymmetric shapes [31]. The NN–phase-field framework matches these baselines without imposing axisymmetry *a priori*, showing that the learned $\phi(\mathbf{r};\Theta)$ naturally converges to axisymmetric shapes when those are energetic minimizers. This validates the functional expression (4.1) and the surface/volume expressions (4.3)–(4.4) used as constraints.

Surface-discretization and finite-element approaches. Triangulation-based tools (e.g., Surface Evolver [38]) and weak-form finite elements [50] have been productive for equilibrium shape prediction under constraints, but they require careful mesh quality control, curvature estimation on discrete surfaces, and frequent remeshing near necks and sharp features. Our approach avoids explicit meshes by optimizing over Θ and relying on automatic differentiation for curvature terms. Where Evolver excels in speed for static, well-resolved surfaces, the NN phase field trades a heavier per-epoch cost for robustness to topology/geometry changes, diffuse-interface regularization, and easy incorporation of external potentials via $P(\Theta)$.

Phase-field dynamics vs. parametric minimization. Prior phase-field studies often minimize energy via gradient flows (Model A/B), evolving ϕ by PDEs and discretizing space/time [45, 48]. We instead perform *direct parametric minimization* of $J(\Theta)$, with ϕ realized by a differentiable NN. This avoids tuning time-step stability and finite-difference stencils for $\nabla^2\phi$, while preserving mass/area constraints through Lagrange multipliers. Numerically, this leads to rapid exploration within parameter basins and efficient continuation along branches by warm-starting from converged Θ at nearby $(\bar{u}, h, \Delta a)$.

Area-difference models and non-axisymmetric shapes. The bilayer-coupling (BC) limit, in which actual and preferred area differences coincide, admits tractable incorporation into our cost via the $M(\Theta)$ functional and its multiplier. Our spherical-confinement results at fixed Δa recover non-axisymmetric families (starfish, hammer, clam-like) previously reported under excess area and confinement [37, 77]. While area-difference-elasticity (ADE) generalizations [155, 108] fall outside the present scope, the parametric framework is well suited to include the non-local contribution, offering a path to full ADE phase maps with the same solver.

Positioning among NN-based physics solvers. Physics-informed neural networks (PINNs) [63, 64] and functional-optimization NNs (e.g., FONN [142]) have shown promise for PDE-constrained learning and energy minimization on grids. Our solver is closer in spirit to functional minimization, but with *analytic* spatial derivatives through autodiff

and a compact, meshfree representation of ϕ. In contrast to grid message-passing or explicit PDE integration, our approach maintains high-order geometric fidelity without finite-difference artifacts, while remaining flexible enough to incorporate additional constraints and external fields ($P(\Theta)$).

6.4 Methodological Considerations

6.4.1 Initialization, continuation, and hysteresis

Because $J(\Theta)$ is non-convex, initialization matters. We use physically informed warm starts (e.g., a sphere fit for prolates; auxiliary penalties for oblates; carved cavities for stomatocytes) and then *continue* in small steps of $(\bar{u}, h, \Delta a)$. The observed hysteresis when cycling h reflects traversal of distinct basins separated by modest energy barriers. Mapping both forward and reverse trajectories, as done in our energy diagrams, helps delineate first-order boundaries and detect metastable branches (e.g., bent-prolate families in spherical confinement).

6.4.2 Resolution, interface width, and accuracy

Sharper interfaces (smaller $\bar{\epsilon}$) reduce diffuse-interface bias in $H[\phi]$ but require finer spatial sampling S to maintain numerical accuracy and stability. In our studies, we primarily used $\bar{\epsilon} = 0.033$ and uniform grids up to $S = 184^3$, which proved sufficient to reproduce axisymmetric baselines and resolve confined morphologies. Further reductions in $\bar{\epsilon}$ improve agreement for nearly flat oblate segments but come at increased computational cost; this can be mitigated through targeted importance sampling or adaptive domain refinement (e.g., adaptively constructing a multi-resolution scheme with a finer resolution at the interface where $\phi(\mathbf{r}; \Theta)$ varies rapidly).

A potential numerical improvement for addressing small $\bar{\epsilon}$ is to incorporate an importance sampling scheme alongside the Monte Carlo method used to evaluate the numerical

integrals required during optimization (training). The importance sampling should concentrate on the interface region, where $\phi(\mathbf{r};\Theta)$ varies rapidly, and on the interior of the vesicle, where $\phi(\mathbf{r};\Theta) \approx 1$, as these regions contribute most significantly to the numerical evaluation of the cost function $J(\Theta)$. By employing suitable Monte Carlo weights, such as densities associated with the surface area and volume functionals, the core of an effective importance sampling strategy can be constructed.

6.4.3 Scalability and portability

The solver's computational core is generic: any modern autodiff library can evaluate $E_b(\Theta)$, constraints, and their gradients. Because Θ is compact, shape libraries can be stored and reused across studies. GPU acceleration parallelizes sampling and automatic differentiation. Collectively, this makes the NN solver practical for large parameter sweeps and multi-confinement phase-diagram construction.

6.5 Limitations and Future Work

ADE model. Extending from BC to ADE entails adding a non-local quadratic penalty in the area difference. Implementing this in $J(\Theta)$ is straightforward. By this extension to the solver, systematic exploration of higher-dimensional phase diagrams that, for instance, combine reduced volume, confinement size, and area difference can be attempted, which also follows a more generalized modeling framework.

Importance sampling and multi-resolution. Accuracy at small $\bar{\epsilon}$ can be improved with importance sampling concentrated in the interfacial and interior regions, or using nested domains with local refinement, for which we discussed some details above.

Richer architectures and optimization methods. While a compact two-hidden-layer FNN sufficed here, deeper networks with more complex architectures, such as residual connections [65], could resolve highly deformed or more complicated morphologies. Conver-

gence can be sensitive to hyperparameters such as learning rate, batch size, and optimizer choice. The optimization method used to minimize the cost is Adam, which is an advanced form of the gradient descent method. However, using other types of optimization methods, namely quasi-Newton methods such as BFGS, Self-Scaled BFGS, and Self-Scaled Broyden, can enhance performance and accuracy by incorporating second-order curvature information of the cost function [68].

Dynamics and hydrodynamic coupling. The present work targets equilibrium shapes. For dynamics in flow and time-resolved transformations [176, 177, 178, 179, 180, 181], one can couple the NN phase field to viscous hydrodynamics, e.g., by embedding the NN in a PINN for the coupled PDEs.

Topology changes and Gaussian curvature. Neck thinning and shape division were observed under Δa and strong confinement. A comprehensive study of topology change requires explicit accounting of the Gaussian term and careful treatment of genus transitions within the phase-field approximation. Our framework can accommodate this by monitoring Euler characteristic and switching energy accounting when components nucleate.

Uncertainty quantification and reproducibility. Because $J(\Theta)$ is non-convex, reporting confidence level (quantifying uncertainty) across multiple random seeds and warm starts is considered good practice. Additionally, integration with experimental imaging data and machine-learning classifiers can help validate morphologies and refine predictions.

6.6 Concluding Remarks

We have introduced a neural-network solver for the phase-field-formulated Helfrich model that (i) reproduces canonical free-space branches without imposing axisymmetry, (ii) computes systematic stability, energy, and phase diagrams across four confinement geometries, (iii) accommodates additional global constraints such as reduced area difference Δa, and (iv) leverages automatic differentiation to avoid finite-difference artifacts in the numerical

evaluations. The solver is compact, reusable, and naturally suited to parameter continuation, enabling dense mapping of shape families and phase boundaries, including the identification of non-axisymmetric intermediates (biaxial, bent) and the classification of first- vs. second-order transitions.

Beyond corroborating prior axisymmetric, non-axisymmetric, and confined-shape literature, the present framework streamlines the generation of full three-dimensional morphologies directly in physical space, integrates external potentials through simple constraint definitions, and provides a clear path to richer physics (ADE, hydrodynamics) and numerical refinements (adaptive sampling, deeper architectures). We anticipate that this combination of geometric fidelity, algorithmic flexibility, and practical scalability will make NN–phase-field solvers a useful complement to traditional numerical approaches in the quantitative study of phospholipid vesicles and related soft-matter interfaces.

References

[1] Bruce Alberts, Rebecca Heald, Alexander Johnson, David Morgan, Martin Raff, Keith Roberts, and Peter Walter. *Molecular Biology of the Cell (Seventh Edition)*. W. W. Norton, Incorporated, New York, 2022.

[2] A E Walsby. Gas vesicles. *Microbiological Reviews*, 58(1):94–144, 1994.

[3] Natalia Gomez-Navarro and Elizabeth Miller. Protein sorting at the er–golgi interface. *Journal of Cell Biology*, 215(6):769–778, 11 2016.

[4] Raghu Kalluri and Valerie S. LeBleu. The biology, function, and biomedical applications of exosomes. *Science*, 367(6478):eaau6977, 2020.

[5] Tsvetomir Ivanov, Shoupeng Cao, Nitin Bohra, Marina de Souza Melchiors, Lucas Caire da Silva, and Katharina Landfester. Polymeric microreactors with ph-controlled spatial localization of cascade reactions. *ACS Applied Materials & Interfaces*, 15(44):50755–50764, 2023. PMID: 37903081.

[6] Mohammad Ashrafuzzaman and Jack A Tuszynski. *Membrane biophysics*. Springer Science & Business Media, Berlin, 2012.

[7] Sarah Zuraw-Weston, Derek A Wood, Ian K Torres, YiWei Lee, Li-Sheng Wang, Ziwen Jiang, Guillermo R Lázaro, ShiYu Wang, Avital A Rodal, Michael F Hagan, et al. Nanoparticles binding to lipid membranes: from vesicle-based gels to vesicle tubulation and destruction. *Nanoscale*, 11(39):18464–18474, 2019.

[8] Olivier G. de Jong, Sander A. A. Kooijmans, Daniel E. Murphy, Linglei Jiang, Martijn J. W. Evers, Joost P. G. Sluijter, Pieter Vader, and Raymond M. Schiffelers. Drug delivery with extracellular vesicles: From imagination to innovation. *Accounts of Chemical Research*, 52(7):1761–1770, 2019. PMID: 31181910.

[9] Luke van der Koog, Timea B Gandek, and Anika Nagelkerke. Liposomes and extracellular vesicles as drug delivery systems: A comparison of composition, pharmacokinetics, and functionalization. *Advanced healthcare materials*, 11(5):2100639, 2022.

[10] Peng Liu, Guiliang Chen, and Jingchen Zhang. A review of liposomes as a drug delivery system: Current status of approved products, regulatory environments, and future perspectives. *Molecules*, 27(4), 2022.

[11] Ramachandran Chelliah, Momna Rubab, Selvakumar Vijayalakshmi, Murugan Karuvelan, Kaliyan Barathikannan, and Deog-Hwan Oh. Liposomes for drug delivery: Classification, therapeutic applications, and limitations. *Next Nanotechnology*, 8:100209, 2025.

[12] Zaneta Sobol, Rafal Chiczewski, and Dorota Watrobska-Swietlikowska. Advances in liposomal drug delivery: Multidirectional perspectives on overcoming biological barriers. *Pharmaceutics*, 17(7), 2025.

[13] Reto A. Schwendener. Liposomes as vaccine delivery systems: a review of the recent advances. *Therapeutic Advances in Vaccines*, 2(6):159–182, 2014. PMID: 25364509.

[14] Rumiana Tenchov, Robert Bird, Allison E Curtze, and Qiongqiong Zhou. Lipid nanoparticles – from liposomes to mrna vaccine delivery, a landscape of research diversity and advancement. *ACS Nano*, 15(11):16982–17015, 2021.

[15] Xucheng Hou, Tal Zaks, Robert Langer, and Yizhou Dong. Lipid nanoparticles for mrna delivery. *Nature Reviews Materials*, 6(12):1078–1094, 2021.

[16] Barnabas Wilson and Kannoth Mukundan Geetha. Lipid nanoparticles in the development of mrna vaccines for covid-19. *Journal of Drug Delivery Science and Technology*, 74:103553, 2022.

[17] K. Swetha, Niranjan G. Kotla, Lakshmi Tunki, Arya Jayaraj, Suresh K. Bhargava, Haitao Hu, Srinivasa Reddy Bonam, and Rajendra Kurapati. Recent advances in the lipid nanoparticle-mediated delivery of mrna vaccines. *Vaccines*, 11(3), 2023.

[18] Myer Bloom, Evan Evans, and Ole G. Mouritsen. Physical properties of the fluid lipid-bilayer component of cell membranes: a perspective. *Quarterly Reviews of Biophysics*, 24(3):293–397, 1991.

[19] John F. Nagle and Stephanie Tristram-Nagle. Structure of lipid bilayers. *Biochimica et Biophysica Acta (BBA) - Reviews on Biomembranes*, 1469(3):159–195, 2000.

[20] David Boal. Biomembranes. In *Mechanics of the Cell*, chapter 10, pages 242–282. Cambridge University Press, Cambridge, 2 edition, 2012.

[21] U. Seifert and R. Lipowsky. Chapter 8 - morphology of vesicles. In R. Lipowsky and E. Sackmann, editors, *Structure and Dynamics of Membranes*, volume 1 of *Handbook of Biological Physics*, pages 403–463. North-Holland, 1995.

[22] Saša Svetina and Boštjan Žekš. Shape behavior of lipid vesicles as the basis of some cellular processes. *The Anatomical Record*, 268(3):215–225, 2002.

[23] J. Majhenc, B. Božič, S. Svetina, and B. Žekš. Phospholipid membrane bending as assessed by the shape sequence of giant oblate phospholipid vesicles. *Biochimica et Biophysica Acta (BBA) - Biomembranes*, 1664(2):257–266, 2004.

[24] Adnan Morshed, Buddini Iroshika Karawdeniya, Y.M. Nuwan D.Y. Bandara, Min Jun Kim, and Prashanta Dutta. Mechanical characterization of vesicles and cells: A review. *ELECTROPHORESIS*, 41(7-8):449–470, 2020.

[25] Håkan Wennerström, Emma Sparr, and Joakim Stenhammar. On the coupling between membrane bending and stretching in lipid vesicles. *Journal of Colloid and Interface Science*, 690:137279, 2025.

[26] Seymour J Singer and Garth L Nicolson. The fluid mosaic model of the structure of cell membranes. *Science*, 175(4023):720–731, 1972.

[27] Wolfgang Helfrich. Elastic properties of lipid bilayers: theory and possible experiments. *Zeitschrift für Naturforschung C*, 28(11-12):693–703, 1973.

[28] Markus Deserno. Fluid lipid membranes–a primer, 2006.

[29] Markus Deserno. Fluid lipid membranes: From differential geometry to curvature stresses. *Chemistry and Physics of Lipids*, 185:11–45, 2015.

[30] Zhong-Can Ou-Yang and Wolfgang Helfrich. Bending energy of vesicle membranes: General expressions for the first, second, and third variation of the shape energy and applications to spheres and cylinders. *Physical Review A*, 39(10):5280–5288, 1989.

[31] Udo Seifert, Karin Berndl, and Reinhard Lipowsky. Shape transformations of vesicles: Phase diagram for spontaneous-curvature and bilayer-coupling models. *Physical Review A*, 44(2):1182, 1991.

[32] Udo Seifert. Configurations of fluid membranes and vesicles. *Advances in Physics*, 46(1):13–137, 1997.

[33] Martin Kraus, Udo Seifert, and Reinhard Lipowsky. Gravity-induced shape transformations of vesicles. *Europhysics Letters*, 32(5):431, 1995.

[34] Jie Yan, Quanhui Liu, Jixing Liu, and Zhong-Can Ou-Yang. Numerical observation of nonaxisymmetric vesicles in fluid membranes. *Physical Review E*, 58(4):4730, 1998.

[35] Primož Ziherl and Saša Svetina. Nonaxisymmetric phospholipid vesicles: Rackets, boomerangs, and starfish. *Europhysics Letters*, 70(5):690, 2005.

[36] Osman Kahraman, Norbert Stoop, and Martin Michael Müller. Morphogenesis of membrane invaginations in spherical confinement. *Europhysics Letters*, 97(6):68008, 2012.

[37] Ai Sakashita, Masayuki Imai, and Hiroshi Noguchi. Morphological variation of a lipid vesicle confined in a spherical vesicle. *Physical Review E*, 89(4):040701, 2014.

[38] Kenneth A Brakke. The surface evolver. *Experimental Mathematics*, 1(2):141–165, 1992.

[39] Volkmar Heinrich, Saša Svetina, and Boštjan Žekš. Nonaxisymmetric vesicle shapes in a generalized bilayer-couple model and the transition between oblate and prolate axisymmetric shapes. *Phys. Rev. E*, 48:3112–3123, Oct 1993.

[40] Volkmar Heinrich, Bojan Božič, Saša Svetina, and Boštjan Žekš. Vesicle deformation by an axial load: From elongated shapes to tethered vesicles. *Biophysical Journal*, 76(4):2056–2071, 1999.

[41] Malcolm I. G. Bloor and Michael J. Wilson. Method for efficient shape parametrization of fluid membranes and vesicles. *Phys. Rev. E*, 61:4218–4229, Apr 2000.

[42] Emmanuel Maitre, Thomas Milcent, Georges-Henri Cottet, Annie Raoult, and Yves Usson. Applications of level set methods in computational biophysics. *Mathematical and Computer Modelling*, 49(11):2161–2169, 2009. Trends in Application of Mathematics to Medicine.

[43] Michael Bergdorf, Ivo F Sbalzarini, and Petros Koumoutsakos. A lagrangian particle method for reaction–diffusion systems on deforming surfaces. *Journal of mathematical biology*, 61:649–663, 2010.

[44] Tiankui Zhang and Charles W Wolgemuth. A general computational framework for the dynamics of single-and multi-phase vesicles and membranes. *Journal of Computational Physics*, 450:110815, 2022.

[45] Qiang Du, Chun Liu, and Xiaoqiang Wang. A phase field approach in the numerical study of the elastic bending energy for vesicle membranes. *Journal of Computational Physics*, 198(2):450–468, 2004.

[46] Thierry Biben, Klaus Kassner, and Chaouqi Misbah. Phase-field approach to three-dimensional vesicle dynamics. *Phys. Rev. E*, 72:041921, Oct 2005.

[47] Qiang Du, Chun Liu, and Xiaoqiang Wang. Simulating the deformation of vesicle membranes under elastic bending energy in three dimensions. *Journal of computational physics*, 212(2):757–777, 2006.

[48] Felix Campelo and Aurora Hernandez-Machado. Dynamic model and stationary shapes of fluid vesicles. *Eur. Phys. J. E*, 20:37–45, 2006.

[49] Timothy Banham, Bo Li, and Yanxiang Zhao. Pattern formation by phase-field relaxation of bending energy with fixed surface area and volume. *Phys. Rev. E*, 90:033308, Sep 2014.

[50] Achim Guckenberger and Stephan Gekle. Theory and algorithms to compute helfrich bending forces: a review. *Journal of Physics: Condensed Matter*, 29(20):203001, apr 2017.

[51] Xin Bian, Sergey Litvinov, and Petros Koumoutsakos. Bending models of lipid bilayer membranes: Spontaneous curvature and area-difference elasticity. *Computer Methods in Applied Mechanics and Engineering*, 359:112758, 2020.

[52] Qiang Du, Chun Liu, R. Ryham, and X. Wang. Modeling the spontaneous curvature effects in static cell membrane deformations by a phase field formulation. *Communications on Pure and Applied Analysis*, 4(3):537–548, 2005.

[53] Warren S McCulloch and Walter Pitts. A logical calculus of the ideas immanent in nervous activity. *The Bulletin of Mathematical Biophysics*, 5:115–133, 1943.

[54] F. Rosenblatt. *Principles of Neurodynamics: Perceptrons and the Theory of Brain Mechanisms*. Cornell Aeronautical Laboratory. Report no. VG-1196-G-8. Spartan Books, Washington DC, 1962.

[55] Michael A Nielsen. *Neural networks and deep learning*. Determination Press, San Francisco, 2015.

[56] Ian Goodfellow, Yoshua Bengio, and Aaron Courville. *Deep Learning*. MIT Press, 2016. http://www.deeplearningbook.org.

[57] Kurt Hornik, Maxwell Stinchcombe, and Halbert White. Multilayer feedforward networks are universal approximators. *Neural Networks*, 2(5):359–366, 1989.

[58] George Cybenko. Approximation by superpositions of a sigmoidal function. *Mathematics of Control, Signals and Systems*, 2(4):303–314, 1989.

[59] Kurt Hornik. Approximation capabilities of multilayer feedforward networks. *Neural Networks*, 4(2):251–257, 1991.

[60] Herbert Robbins and Sutton Monro. A Stochastic Approximation Method. *The Annals of Mathematical Statistics*, 22(3):400 – 407, 1951.

[61] Geoffrey Hinton. rmsprop: Divide the gradient by a running average of its recent magnitude. https://www.cs.toronto.edu/~tijmen/csc321/slides/lecture_slides_lec6.pdf. (accessed: 17.06.2025).

[62] Diederik P Kingma and Jimmy Ba. Adam: A method for stochastic optimization. *arXiv preprint arXiv:1412.6980*, 2017.

[63] Maziar Raissi. Deep hidden physics models: Deep learning of nonlinear partial differential equations. *Journal of Machine Learning Research*, 19(25):1–24, 2018.

[64] M. Raissi, P. Perdikaris, and G.E. Karniadakis. Physics-informed neural networks: A deep learning framework for solving forward and inverse problems involving nonlinear partial differential equations. *Journal of Computational Physics*, 378:686–707, 2019.

[65] Kaiming He, Xiangyu Zhang, Shaoqing Ren, and Jian Sun. Deep residual learning for image recognition. In *2016 IEEE Conference on Computer Vision and Pattern Recognition (CVPR)*, pages 770–778, 2016.

[66] Ashish Vaswani, Noam Shazeer, Niki Parmar, Jakob Uszkoreit, Llion Jones, Aidan N Gomez, Ł ukasz Kaiser, and Illia Polosukhin. Attention is all you need. In I. Guyon, U. Von Luxburg, S. Bengio, H. Wallach, R. Fergus, S. Vishwanathan, and R. Garnett, editors, *Advances in Neural Information Processing Systems*, volume 30. Curran Associates, Inc., 2017.

[67] Ziming Liu, Yixuan Wang, Sachin Vaidya, Fabian Ruehle, James Halverson, Marin Soljacic, Thomas Y. Hou, and Max Tegmark. Kan: Kolmogorov-arnold networks. *arXiv preprint arXiv:2404.19756v5 [cs.LG]*, 2024.

[68] Elham Kiyani, Khemraj Shukla, Jorge F. Urbán, Jérôme Darbon, and George Em Karniadakis. Optimizing the optimizer for physics-informed neural networks and kolmogorov-arnold networks. *Computer Methods in Applied Mechanics and Engineering*, 446:118308, 2025.

[69] Peter B Canham. The minimum energy of bending as a possible explanation of the biconcave shape of the human red blood cell. *Journal of Theoretical Biology*, 26(1):61–81, 1970.

[70] Evan A Evans. Bending resistance and chemically induced moments in membrane bilayers. *Biophysical Journal*, 14(12):923–931, 1974.

[71] G. Gompper and S. Zschocke. Elastic properties of interfaces in a ginzburg-landau theory of swollen micelles, droplet crystals and lamellar phases. *Europhysics Letters*, 16(8):731, Oct 1991.

[72] Michael P Sheetz and Seymour J Singer. Biological membranes as bilayer couples. a molecular mechanism of drug-erythrocyte interactions. *Proceedings of the National Academy of Sciences*, 71(11):4457–4461, 1974.

[73] Saša Svetina and Boštjan Žekš. Membrane bending energy and shape determination of phospholipid vesicles and red blood cells. *European Biophysics Journal*, 17:101–111, 1989.

[74] Wolfgang Wintz, Hans-Günther Döbereiner, and Udo Seifert. Starfish vesicles. *Europhysics Letters*, 33(5):403, Feb 1996.

[75] Xavier Michalet. Equilibrium shape degeneracy in starfish vesicles. *Phys. Rev. E*, 76:021914, Aug 2007.

[76] Osman Kahraman, Norbert Stoop, and Martin Michael Müller. Fluid membrane vesicles in confinement. *New Journal of Physics*, 14(9):095021, 2012.

[77] B Kavčič, A Sakashita, H Noguchi, and P Ziherl. Limiting shapes of confined lipid vesicles. *Soft Matter*, 15(4):602–614, 2019.

[78] Niloufar Abtahi, Lila Bouzar, Nadia Saidi-Amroun, and Martin Michael Müller. Flexoelectric fluid membrane vesicles in spherical confinement. *Europhysics Letters*, 131(1):18001, 2020.

[79] Jee E Rim, Prashant K Purohit, and William S Klug. Mechanical collapse of confined fluid membrane vesicles. *Biomechanics and Modeling in Mechanobiology*, 13:1277–1288, 2014.

[80] Ai Sakashita, Naohito Urakami, Primož Ziherl, and Masayuki Imai. Three-dimensional analysis of lipid vesicle transformations. *Soft Matter*, 8(33):8569–8581, 2012.

[81] Hamid R. Shojaei and Murugappan Muthukumar. Translocation of an incompressible vesicle through a pore. *The Journal of Physical Chemistry B*, 120(26):6102–6109, 2016.

[82] Sara Salehyar and Qiang Zhu. Deformation and internal stress in a red blood cell as it is driven through a slit by an incoming flow. *Soft Matter*, 12:3156–3164, 2016.

[83] Petch Khunpetch, Xingkun Man, Toshihiro Kawakatsu, and Masao Doi. Translocation of a vesicle through a narrow hole across a membrane. *The Journal of Chemical Physics*, 148(13):134901, Apr 2018.

[84] Bogdan Ranguelov and Andrey Milchev. Translocation kinetics of vesicles through narrow pores. *Europhysics Letters*, 138(4):42001, Jun 2022.

[85] Bin Zheng, Fangfu Ye, Shigeyuki Komura, and Masao Doi. Universality in the dynamics of vesicle translocation through a hole. *Langmuir*, 39(1):563–569, 2023.

[86] Nishant Baruah, Jiarul Midya, Gerhard Gompper, Anil Kumar Dasanna, and Thorsten Auth. Adhesion-driven vesicle translocation through membrane-covered pores. *bioRxiv*, 2024.

[87] Manit Klawtanong, Yuka Sakuma, Masayuki Imai, Toshihiro Kawakatsu, and Petch Khunpetch. Translocation of a daughter vesicle in a model system of self-reproducing vesicles. *Physics of Fluids*, 36(2):027112, Feb 2024.

[88] John F. Nagle. Introductory lecture: Basic quantities in model biomembranes. *Faraday Discuss.*, 161:11–29, 2013.

[89] David P Siegel and MM Kozlov. The gaussian curvature elastic modulus of n-monomethylated dioleoylphosphatidylethanolamine: relevance to membrane fusion and lipid phase behavior. *Biophysical journal*, 87(1):366–374, 2004.

[90] Joseph A. Szule, Nola L. Fuller, and R. Peter Rand. The effects of acyl chain length and saturation of diacylglycerols and phosphatidylcholines on membrane monolayer curvature. *Biophysical Journal*, 83(2):977–984, 2002.

[91] Bae-Yeun Ha. Effect of divalent counterions on asymmetrically charged lipid bilayers. *Phys. Rev. E*, 67:030901, Mar 2003.

[92] John M Lee. *Riemannian Manifolds: An Introduction to Curvature*. Graduate Texts in Mathematics. Springer-Verlag, New York, 1997.

[93] L.D. Landau, E.M. Lifshitz, A.M. Kosevich, and L.P. Pitaevskii. Chapter ii - the equilibrium of rods and plates. In *Theory of Elasticity (Third Edition)*, pages 38–86. Butterworth-Heinemann, Oxford, third edition edition, 1986.

[94] Gerald Lim H. W., Michael Wortis, and Ranjan Mukhopadhyay. Stomatocyte–discocyte–echinocyte sequence of the human red blood cell: Evidence for the bilayer– couple hypothesis from membrane mechanics. *Proceedings of the National Academy of Sciences*, 99(26):16766–16769, 2002.

[95] Khaled Khairy, JiJinn Foo, and Jonathon Howard. Shapes of red blood cells: comparison of 3d confocal images with the bilayer-couple model. *Cellular and Molecular Bioengineering*, 1:173–181, 2008.

[96] Heinz J Deuling and Wolfgang Helfrich. The curvature elasticity of fluid membranes: a catalogue of vesicle shapes. *Journal de Physique*, 37(11):1335–1345, 1976.

[97] EA Evans. Bending elastic modulus of red blood cell membrane derived from buckling instability in micropipet aspiration tests. *Biophysical Journal*, 43(1):27—30, July 1983.

[98] Lin Bo and Richard E. Waugh. Determination of bilayer membrane bending stiffness by tether formation from giant, thin-walled vesicles. *Biophysical Journal*, 55(3):509–517, 1989.

[99] E. Evans and W. Rawicz. Entropy-driven tension and bending elasticity in condensed-fluid membranes. *Phys. Rev. Lett.*, 64:2094–2097, Apr 1990.

[100] Lap Man Lee and Allen P. Liu. The application of micropipette aspiration in molecular mechanics of single cells. *Journal of Nanotechnology in Engineering and Medicine*, 5(4):040902, 11 2014.

[101] David Needham and Rashmi S Nunn. Elastic deformation and failure of lipid bilayer membranes containing cholesterol. *Biophysical Journal*, 58(4):997–1009, 1990.

[102] Doncho V Zhelev, David Needham, and Robert M Hochmuth. A novel micropipet method for measuring the bending modulus of vesicle membranes. *Biophysical journal*, 67(2):720–727, 1994.

[103] Jonas Rosager Henriksen and John Hjort Ipsen. Measurement of membrane elasticity by micro-pipette aspiration. *The European Physical Journal E*, 14:149–167, 2004.

[104] Marjorie L. Longo and Hung V. Ly. *Micropipet Aspiration for Measuring Elastic Properties of Lipid Bilayers*, pages 421–437. Humana Press, Totowa, NJ, 2007.

[105] Hirokazu Hotani. Transformation pathways of liposomes. *Journal of Molecular Biology*, 178(1):113–120, 1984.

[106] K. Berndl, J. Käs, R. Lipowsky, E. Sackmann, and U. Seifert. Shape transformations of giant vesicles: Extreme sensitivity to bilayer asymmetry. *Europhysics Letters*, 13(7):659, dec 1990.

[107] J Käs and E Sackmann. Shape transitions and shape stability of giant phospholipid vesicles in pure water induced by area-to-volume changes. *Biophysical Journal*, 60(4):825–844, 1991.

[108] H.-G. Döbereiner, E. Evans, M. Kraus, U. Seifert, and M. Wortis. Mapping vesicle shapes into the phase diagram: A comparison of experiment and theory. *Phys. Rev. E*, 55:4458–4474, Apr 1997.

[109] Miho Yanagisawa, Masayuki Imai, and Takashi Taniguchi. Shape deformation of ternary vesicles coupled with phase separation. *Physical Review Letters*, 100(14):148102, 2008.

[110] Karim Helal, Thierry Biben, and Jean-Pierre Hansen. Influence of capillary confinement on the equilibrium shape of vesicles. *Journal of Physics: Condensed Matter*, 11(6):L51, feb 1999.

[111] Lila Bouzar, Ferhat Menas, and Martin Michael Müller. Toroidal membrane vesicles in spherical confinement. *Phys. Rev. E*, 92:032721, Sep 2015.

[112] Siqin Cao, Guanghong Wei, and Jeff Z Y Chen. Transformation of an oblate-shaped vesicle induced by an adhering spherical particle. *Physical Review E*, 84(5):050901, 2011.

[113] Jeff Z Y Chen. Pulling or compressing a vesicle by force: Solution to the bending energy model. *Physical Review E*, 85(6):061910, 2012.

[114] Jeff Z Y Chen. Structure of a micropipette-aspirated vesicle determined from the bending-energy model. *Physical Review E*, 86(4):041904, 2012.

[115] Qiang Du and Jian Zhang. Adaptive finite element method for a phase field bending elasticity model of vesicle membrane deformations. *SIAM Journal on Scientific Computing*, 30(3):1634–1657, 2008.

[116] Badr Kaoui, Timm Krüger, and Jens Harting. How does confinement affect the dynamics of viscous vesicles and red blood cells? *Soft Matter*, 8:9246–9252, 2012.

[117] Constantine Pozrikidis. Finite deformation of liquid capsules enclosed by elastic membranes in simple shear flow. *Journal of Fluid Mechanics*, 297:123–152, 1995.

[118] Constantine Pozrikidis. Numerical simulation of cell motion in tube flow. *Annals of biomedical engineering*, 33:165–178, 2005.

[119] Paul G. Chen, J. M. Lyu, M. Jaeger, and M. Leonetti. Shape transition and hydrodynamics of vesicles in tube flow. *Phys. Rev. Fluids*, 5:043602, Apr 2020.

[120] Hiroshi Noguchi and Gerhard Gompper. Dynamics of fluid vesicles in shear flow: Effect of membrane viscosity and thermal fluctuations. *Phys. Rev. E*, 72:011901, Jul 2005.

[121] Hiroshi Noguchi and Gerhard Gompper. Shape transitions of fluid vesicles and red blood cells in capillary flows. *Proceedings of the National Academy of Sciences*, 102(40):14159–14164, 2005.

[122] Zhangli Peng, Xuejin Li, Igor V. Pivkin, Ming Dao, George E. Karniadakis, and Subra Suresh. Lipid bilayer and cytoskeletal interactions in a red blood cell. *Proceedings of the National Academy of Sciences*, 110(33):13356–13361, 2013.

[123] Sebastian Aland, Sabine Egerer, John Lowengrub, and Axel Voigt. Diffuse interface models of locally inextensible vesicles in a viscous fluid. *Journal of Computational Physics*, 277:32–47, 2014.

[124] Wieland Marth, Sebastian Aland, and Axel Voigt. Margination of white blood cells: a computational approach by a hydrodynamic phase field model. *Journal of Fluid Mechanics*, 790:389–406, 2016.

[125] Navid Valizadeh and Timon Rabczuk. Isogeometric analysis of hydrodynamics of vesicles using a monolithic phase-field approach. *Computer Methods in Applied Mechanics and Engineering*, 388:114191, 2022.

[126] Guillermo R. Lázaro, Ignacio Pagonabarraga, and Aurora Hernández-Machado. Phase-field theories for mathematical modeling of biological membranes. *Chemistry and Physics of Lipids*, 185:46–60, 2015. Membrane mechanochemistry: From the molecular to the cellular scale.

[127] A. Rosolen, C. Peco, and M. Arroyo. An adaptive meshfree method for phase-field models of biomembranes. part i: Approximation with maximum-entropy basis functions. *Journal of Computational Physics*, 249:303–319, 2013.

[128] John S. Lowengrub, Andreas Rätz, and Axel Voigt. Phase-field modeling of the dynamics of multicomponent vesicles: Spinodal decomposition, coarsening, budding, and fission. *Phys. Rev. E*, 79:031926, Mar 2009.

[129] F. Guillén-González and G. Tierra. Unconditionally energy stable numerical schemes for phase-field vesicle membrane model. *Journal of Computational Physics*, 354:67–85, 2018.

[130] A.J. Meade and A.A. Fernandez. Solution of nonlinear ordinary differential equations by feedforward neural networks. *Mathematical and Computer Modelling*, 20(9):19–44, 1994.

[131] B. Ph. van Milligen, V. Tribaldos, and J. A. Jiménez. Neural network differential equation and plasma equilibrium solver. *Phys. Rev. Lett.*, 75:3594–3597, Nov 1995.

[132] I.E. Lagaris, A. Likas, and D.I. Fotiadis. Artificial neural networks for solving ordinary and partial differential equations. *IEEE Transactions on Neural Networks*, 9(5):987–1000, 1998.

[133] I.E. Lagaris, A.C. Likas, and D.G. Papageorgiou. Neural-network methods for boundary value problems with irregular boundaries. *IEEE Transactions on Neural Networks*, 11(5):1041–1049, 2000.

[134] Marcelino Quito, Christopher Monterola, and Caesar Saloma. Solving N-body problems with neural networks. *Phys. Rev. Lett.*, 86:4741–4744, May 2001.

[135] Lucie P Aarts and Peter Van Der Veer. Neural network method for solving partial differential equations. *Neural Processing Letters*, 14:261–271, 2001.

[136] Richard Bellman. *Dynamic Programming*. Dover Publications, Mineoal, N.Y., 1957.

[137] Weinan E, Jiequn Han, and Arnulf Jentzen. Deep learning-based numerical methods for high-dimensional parabolic partial differential equations and backward stochastic differential equations. *Communications in Mathematics and Statistics*, 5(4):349–380, 2017.

[138] Jiequn Han, Arnulf Jentzen, and Weinan E. Solving high-dimensional partial differential equations using deep learning. *Proceedings of the National Academy of Sciences*, 115(34):8505–8510, 2018.

[139] Qianshi Wei, Ying Jiang, and Jeff Z. Y. Chen. Machine-learning solver for modified diffusion equations. *Phys. Rev. E*, 98:053304, Nov 2018.

[140] Jian Wang, Xue Pang, Faliang Yin, and Jun Yao. A deep neural network method for solving partial differential equations with complex boundary in groundwater seepage. *Journal of Petroleum Science and Engineering*, 209:109880, 2022.

[141] Zichao Jiang, Junyang Jiang, Qinghe Yao, and Gengchao Yang. A neural network-based pde solving algorithm with high precision. *Scientific Reports*, 13(1):4479, 2023.

[142] Sanjeeb Poudel, Xiaoqiang Wang, and Sanghyun Lee. A novel technique for minimizing energy functional using neural networks. *Engineering Applications of Artificial Intelligence*, 133:108313, 2024.

[143] Karan D Sharma, Milka Doktorova, M Neal Waxham, and Frederick A Heberle. Cryo-em images of phase-separated lipid bilayer vesicles analyzed with a machine-learning approach. *Biophysical Journal*, 123(17):2877–2891, 2024.

[144] Il-Hyung Lee, Sam Passaro, Selin Ozturk, Juan Ureña, and Weitian Wang. Intelligent fluorescence image analysis of giant unilamellar vesicles using convolutional neural network. *BMC Bioinformatics*, 23(1):48, 2022.

[145] Prantar Dutta, Deepak Jain, Rakesh Gupta, and Beena Rai. Deep learning models for the estimation of free energy of permeation of small molecules across lipid membranes. *Digital Discovery*, 2:189–201, 2023.

[146] L. D. Landau and E. M. Lifshitz. *Statistical Physics*. Pergamon Press, Oxford, 3rd edition, 1980.

[147] John W. Cahn and John E. Hilliard. Free Energy of a Nonuniform System. I. Interfacial Free Energy. *The Journal of Chemical Physics*, 28(2):258–267, Feb 1958.

[148] John W. Cahn and Samuel M. Allen. A microscopic theory for domain wall motion and its experimental verification in fe-al alloy domain growth kinetics. *Le Journal De Physique Colloques*, 38:369–372, 1977.

[149] Xiaofeng Yang and Lili Ju. Efficient linear schemes with unconditional energy stability for the phase field elastic bending energy model. *Computer Methods in Applied Mechanics and Engineering*, 315:691–712, 2017.

[150] Xiaoqiang Wang. *Phase field models and simulations of vesicle bio-membranes*. Phd thesis, The Pennsylvania State University, University Park, PA, August 2005. Available at https://etda.libraries.psu.edu/files/final_submissions/6651.

[151] Takashi Sakai. On Riemannian manifolds admitting a function whose gradient is of constant norm. *Kodai Mathematical Journal*, 19(1):39 – 51, 1996.

[152] Manfredo P. do Carmo. *Differential Geometry of Curves and Surfaces: Revised and Updated Second Edition*. Dover Books on Mathematics. Dover Publications, Mineola, New York, second edition, 2016.

[153] Barrett O'Neill. *Elementary Differential Geometry, Revised 2nd Edition*. Academic Press, Boston, second edition, 2006.

[154] Nikolas Provatas and Ken Elder. *Nonequilibrium Dynamics*, chapter 4, pages 33–56. John Wiley & Sons, Ltd, 2010.

[155] Ling Miao, Udo Seifert, Michael Wortis, and Hans-Günther Döbereiner. Budding transitions of fluid-bilayer vesicles: The effect of area-difference elasticity. *Physical Review E*, 49(6):5389, 1994.

[156] Zachary C. Lipton, John Berkowitz, and Charles Elkan. A critical review of recurrent neural networks for sequence learning. *arXiv preprint arXiv:1506.00019v4 [cs.LG]*, 2015.

[157] Alex Sherstinsky. Fundamentals of recurrent neural network (rnn) and long short-term memory (lstm) network. *Physica D: Nonlinear Phenomena*, 404:132306, 2020.

[158] Keiron O'Shea and Ryan Nash. An introduction to convolutional neural networks. *arXiv preprint arXiv:1511.08458v2 [cs.NE]*, 2015.

[159] Namig J Guliyev and Vugar E Ismailov. On the approximation by single hidden layer feedforward neural networks with fixed weights. *Neural Networks*, 98:296–304, 2018.

[160] Namig J Guliyev and Vugar E Ismailov. Approximation capability of two hidden layer feedforward neural networks with fixed weights. *Neurocomputing*, 316:262–269, 2018.

[161] Geoffrey E. Hinton, Nitish Srivastava, Alex Krizhevsky, Ilya Sutskever, and Ruslan R. Salakhutdinov. Improving neural networks by preventing co-adaptation of feature detectors. *arXiv preprint arXiv:1207.0580v1 [cs.NE]*, 2012.

[162] David E Rumelhart, Geoffrey E Hinton, and Ronald J Williams. Learning representations by back-propagating errors. *Nature*, 323(6088):533–536, 1986.

[163] PyTorch Library. https://pytorch.org/, 2024.

[164] Yousef Rohanizadegan, Hong Li, and Jeff Z. Y. Chen. Neural-network-based solver for vesicle shapes predicted by the helfrich model. *Soft Matter*, 20:5359–5366, 2024.

[165] Markus Deserno. Elastic deformation of a fluid membrane upon colloid binding. *Physical Review E*, 69(3):031903, 2004.

[166] Vitaly Maiorov and Allan Pinkus. Lower bounds for approximation by mlp neural networks. *Neurocomputing*, 25(1-3):81–91, 1999.

[167] Hong Li, Qilong Zhai, and Jeff Z Y Chen. Neural-network-based multistate solver for a static schrödinger equation. *Physical Review A*, 103(3):032405, 2021.

[168] Keita Ikari, Yuka Sakuma, Takehiro Jimbo, Atsuji Kodama, Masayuki Imai, Pierre-Alain Monnard, and Steen Rasmussen. Dynamics of fatty acid vesicles in response to ph stimuli. *Soft Matter*, 11(31):6327–6334, 2015.

[169] Terrence G Frey and Carmen A Mannella. The internal structure of mitochondria. *Trends in Biochemical Sciences*, 25(7):319–324, 2000.

[170] Carmen A. Mannella. Structure and dynamics of the mitochondrial inner membrane cristae. *Biochimica et Biophysica Acta (BBA) - Molecular Cell Research*, 1763(5):542–548, 2006. Mitochondrial Dynamics in Cell Life and Death.

[171] Martin van der Laan, Maria Bohnert, Nils Wiedemann, and Nikolaus Pfanner. Role of minos in mitochondrial membrane architecture and biogenesis. *Trends in Cell Biology*, 22(4):185–192, 2012.

[172] Gregor Fuhrmann, Inge K. Herrmann, and Molly M. Stevens. Cell-derived vesicles for drug therapy and diagnostics: Opportunities and challenges. *Nano Today*, 10(3):397–409, 2015.

[173] Omnia M. Elsharkasy, Joel Z. Nordin, Daniel W. Hagey, Olivier G. de Jong, Raymond M. Schiffelers, Samir EL Andaloussi, and Pieter Vader. Extracellular vesicles as drug delivery systems: Why and how? *Advanced Drug Delivery Reviews*, 159:332–343, 2020. Lipids in disease pathology, diagnosis & therapy.

[174] Wanrong Meng, Chuanshi He, Yaying Hao, Linlin Wang, Ling Li, and Guiquan Zhu. Prospects and challenges of extracellular vesicle-based drug delivery system: considering cell source. *Drug Delivery*, 27(1):585–598, 2020. PMID: 32264719.

[175] Ruotong Huang, Jiajun Zhu, Ru Fan, Yiting Tang, Lianlong Hu, HaeJu Lee, and Shuying Chen. Extracellular vesicle-based drug delivery systems in cancer. *Extracellular Vesicle*, 4:100053, 2024.

[176] Robijn Bruinsma. Rheology and shape transitions of vesicles under capillary flow. *Physica A: Statistical Mechanics and its Applications*, 234(1):249–270, 1996.

[177] V. Vitkova, M. Mader, and T. Podgorski. Deformation of vesicles flowing through capillaries. *Europhysics Letters*, 68(3):398, oct 2004.

[178] Badr Kaoui, Jens Harting, and Chaouqi Misbah. Two-dimensional vesicle dynamics under shear flow: Effect of confinement. *Phys. Rev. E*, 83:066319, Jun 2011.

[179] B. Kaoui, N. Tahiri, T. Biben, H. Ez-Zahraouy, A. Benyoussef, G. Biros, and C. Misbah. Complexity of vesicle microcirculation. *Phys. Rev. E*, 84:041906, Oct 2011.

[180] Eduard Benet and Franck J. Vernerey. Mechanics and stability of vesicles and droplets in confined spaces. *Phys. Rev. E*, 94:062613, Dec 2016.

[181] Dhwanit Agarwal and George Biros. Stable shapes of three-dimensional vesicles in unconfined and confined poiseuille flow. *Phys. Rev. Fluids*, 5:013603, Jan 2020.

[182] Caiqun Wang, Jianfeng Li, Liutao Zhao, and Ping Qian. Shape transformations of red blood cells in the capillary and their possible connections to oxygen transportation. *Journal of Biological Physics*, 48:79–92, 2022.

[183] Hao Wu. A review on the cahn–hilliard equation: classical results and recent advances in dynamic boundary conditions. *Electronic Research Archive*, 30(8):2788–2832, 2022.

[184] Junseok Kim, Seunggyu Lee, Yongho Choi, Seok-Min Lee, and Darae Jeong. Basic principles and practical applications of the cahn–hilliard equation. *Mathematical Problems in Engineering*, 2016(1):9532608, 2016.

APPENDICES

Appendix A

Phase-field Formulation of Helfrich Model

The content in this appendix overlaps with the text in [164] and complements the material developed in Chapters 2 and 4.

Here, we show that (4.1) can be readily cast into an equivalent phase-field form for the case of zero spontaneous curvature and invariant Euler characteristic. Its customary to assume the phase field ansatz, $\phi(\mathbf{r}) = \tanh(d(\mathbf{r})/\sqrt{2}\epsilon)$ in the phase-filed formalism. The sharpness of the membrane interface is determined by ϵ and $d(\mathbf{r})$ represents the signed distance from the membrane in a three dimensional space. It is straightforward to show [150]

$$\nabla^2_{ij} d(\mathbf{r}) = \frac{\sqrt{2}\epsilon}{1-\phi(\mathbf{r})^2}\left[\nabla^2_{ij}\phi(\mathbf{r}) + \frac{2\phi(\mathbf{r})}{1-\phi(\mathbf{r})^2}\nabla_i\phi(\mathbf{r})\nabla_j\phi(\mathbf{r})\right], \tag{A.1}$$

where i and j denote the different coordinates in 3D.

The sum of eigenvalues (trace) of the matrix constructed by (A.1) is related to the

mean curvature [45, 46, 48, 150]

$$\begin{aligned} H &= -\frac{1}{2} tr\left(\nabla^2 d(\mathbf{r})\right) \\ &= -\frac{\epsilon}{\sqrt{2}\left(1-\phi(\mathbf{r})^2\right)}\left[\nabla^2\phi(\mathbf{r}) + \frac{2\phi(\mathbf{r})}{1-\phi(\mathbf{r})^2}|\nabla\phi(\mathbf{r})|^2\right] \\ &= -\frac{\epsilon}{\sqrt{2}\left(1-\phi(\mathbf{r})^2\right)}\left[\nabla^2\phi(\mathbf{r}) + \frac{1}{\epsilon^2}\phi(\mathbf{r})[1-\phi(\mathbf{r})^2]\right], \end{aligned} \tag{A.2}$$

where we have used $|\nabla\phi(\mathbf{r})|^2 = \frac{1}{2\epsilon^2}(1-\phi(\mathbf{r})^2)^2$ to obtain a more familiar form.

The expression for the bending energy given by (4.1) can be rewritten by (A.2) and converted to a volume integral [52, 150]. Using $\int_{-\infty}^{\infty} \mathrm{d}\alpha(1-\phi(\alpha)^2)^2 = \frac{4\sqrt{2}\epsilon}{3}$ ($\phi(\alpha) = \tanh(\alpha/\sqrt{2}\epsilon)$) we have

$$\begin{aligned} E_b[\phi] &= 2\kappa\int_S H^2 \mathrm{d}S \\ &= \left(\frac{3}{4\sqrt{2}\epsilon}\int_{-\infty}^{\infty}\mathrm{d}\alpha(1-\phi(\alpha)^2)^2\right) 2\kappa\int_S H^2\mathrm{d}S \\ &\sim \frac{3\kappa}{4\sqrt{2}\epsilon}\int \mathrm{d}\mathbf{r}\left[\epsilon\nabla^2\phi(\mathbf{r}) + \frac{1}{\epsilon}\phi(\mathbf{r})[1-\phi(\mathbf{r})^2]\right]^2. \end{aligned} \tag{A.3}$$

The expression for the surface area of vesicle in terms of the phase field $\phi(\mathbf{r})$ can be formulated in a similar manner. Starting from a surface integral, we obtain a volume integral for the surface area as follows

$$\begin{aligned} A[\phi] &= \int_S \mathrm{d}S \\ &= \left(\frac{3}{4\sqrt{2}\epsilon}\int_{-\infty}^{\infty}\mathrm{d}\alpha(1-\phi(\alpha)^2)^2\right)\int_S \mathrm{d}S \\ &\sim \frac{3}{4\sqrt{2}\epsilon}\int \mathrm{d}\mathbf{r}[1-\phi(\mathbf{r})^2]^2 \\ &= \frac{3}{4\sqrt{2}}\int \mathrm{d}\mathbf{r}\left[\epsilon|\nabla\phi(\mathbf{r})|^2 + \frac{1}{2\epsilon}[1-\phi(\mathbf{r})^2]^2\right], \end{aligned} \tag{A.4}$$

where we have used $|\nabla\phi(\mathbf{r})|^2 = \frac{1}{2\epsilon^2}(1-\phi(\mathbf{r})^2)^2$ in the last step.

It should be noted that in the limit $\epsilon \to 0$ both (A.3) and (A.4) become precise [45, 52, 150].

The expression for the vesicle volume can be derived from the fact that in the interior $\phi(\mathbf{r}) \to +1$ and in the exterior $\phi(\mathbf{r}) \to -1$. Thus, by applying a shift and an appropriate scaling we end up with (4.4) for the volume.

The phase-field-formulated Helfirch model for the bending energy subject to constraints on surface area and volume can now be represented by an NN, which introduces a set of network parameters in the definition of the phase field that yields $\phi(\mathbf{r}; \Theta)$. A Lagrangian function with appropriate Lagrange multipliers is defined, which is then minimized to obtain the minimum energy shapes of vesicles. This function is the cost J given by (4.6), for which the volume integrals are carried out by (4.5) numerically.

Appendix B

Phase-field Formulation of the Local Mean Curvature

The content in this appendix complements the material developed in Chapters 2 and 4.

Here, we show that an expression for the mean curvature can be derived from a phase-field-based functional for the surface area of the vesicle.The expression for this functional is:

$$A[\phi] = C_1 \int \left[\epsilon |\nabla \phi(\mathbf{r})|^2 + \frac{1}{2\epsilon} \left(1 - \phi(\mathbf{r})^2\right)^2 \right] \mathrm{d}\mathbf{r}, \tag{B.1}$$

where C_1 is a dimensionless numerical coefficient that adjusts the value of the surface area and will be determined later. This expression is similar in form to the Ginzburg–Landau energy functional [71, 126], which, for instance, defines the free energy of a binary solution in the derivation of the Cahn–Hilliard equation [147]. The first term corresponds to the spatial gradient of the order parameter in the mixture, and the second term resembles the so-called double-well potential, representing the bulk free energy of the mixture [183, 184]. In this context, the order parameter is replaced by the phase field, and the binary solution is replaced by the 3D space containing the phospholipid vesicle and its surrounding environment. The goal is to model the vesicle and its environment using the phase field, which makes the interior and exterior regions distinguishable by an interface. The thickness of this interface, representing the position of the membrane—the transition layer from

$\phi = +1$ to $\phi = -1$—is controlled by ϵ.

The form of the function commonly assumed for the phase field is sigmoid in type, specifically $\phi(\mathbf{r}) = \tanh(C_2 d(\mathbf{r}))$, where the numerical constant C_2 controls the sharpness of the transition from $\phi(\mathbf{r}) = -1$ to $\phi(\mathbf{r}) = +1$. The first and second terms in (B.1) behave as delta functions, given this specific form of $\phi(\mathbf{r})$, as $\epsilon \to 0$ and $C_2 \to \infty$. Therefore, at the interface where $d(\mathbf{r}) = 0$, (B.1), which is a volume integral, can be used to evaluate the surface area of the vesicle shapes.

We can examine the first variation of (B.1) with respect to $\phi(\mathbf{r})$ to investigate whether an expression for the mean curvature can be extracted from this definition of the surface area. To do this, we first determine the functional derivative of $A[\phi]$ as follows (we have omitted the $\mathbf{r}$-dependence in the notation for brevity):

$$\frac{\delta A}{\delta \phi} = \frac{\partial A}{\partial \phi} - \nabla \cdot \frac{\partial A}{\partial (\nabla \phi)}. \tag{B.2}$$

Here, we truncate the functional derivative to the highest order of spatial derivatives present in the definition of $A[\phi]$. The partial derivative with respect to ϕ is:

$$\frac{\partial A}{\partial \phi} = -C_1 \frac{2}{\epsilon} \phi (1 - \phi^2). \tag{B.3}$$

In the same manner, we have

$$\frac{\partial A}{\partial (\nabla \phi)} = C_1 2 \epsilon \nabla \phi, \tag{B.4}$$

which is used to calculate

$$\nabla \cdot \frac{\partial A}{\partial (\nabla \phi)} = C_1 2 \epsilon \nabla^2 \phi. \tag{B.5}$$

Substituting (B.3) and (B.5) into (B.2), we obtain

$$\frac{\delta A}{\delta \phi} = -C_1 \left[\frac{2}{\epsilon} \phi (1 - \phi^2) + 2 \epsilon \nabla^2 \phi \right], \tag{B.6}$$

which is the expression for the functional derivative of the surface area in terms of the phase field and its spatial derivative in 3D.

Now, to show that an expression for the mean curvature H can be derived from (B.6), we substitute $\tanh(C_2 d(\mathbf{r}))$ for $\phi(\mathbf{r})$. The Laplacian term can be calculated as follows:

$$\nabla \phi = C_2 \nabla d(\mathbf{r}) \left[1 - \tanh^2 \left(C_2 d(\mathbf{r}) \right) \right], \tag{B.7}$$

and

$$\begin{aligned}\nabla^2\phi &= C_2\nabla^2 d(\mathbf{r})\left[1-\tanh^2\left(C_2 d(\mathbf{r})\right)\right] \\ &\quad -2{C_2}^2\tanh\left(C_2 d(\mathbf{r})\right)\left[1-\tanh^2\left(C_2 d(\mathbf{r})\right)\right], \end{aligned} \tag{B.8}$$

where we have used the property of the signed distance $|\nabla d(\mathbf{r})|^2 = 1$ [151]. Substituting the above into (B.6), we get

$$\begin{aligned}\frac{\delta A}{\delta\phi} &= -C_1\left[\frac{2}{\epsilon}\phi(1-\phi^2)+2\epsilon\nabla^2\phi\right] \\ &= -C_1\left[(\frac{2}{\epsilon}-4\epsilon{C_2}^2)\tanh\left(C_2 d(\mathbf{r})\right)+2\epsilon C_2\nabla^2 d(\mathbf{r})\right]\left[1-\tanh^2\left(C_2 d(\mathbf{r})\right)\right]. \end{aligned} \tag{B.9}$$

It is known from differential geometry that $\nabla^2 d(\mathbf{r})$ is the negative of the trace of the shape operator (whose matrix elements can be calculated using the Weingarten equations), i.e., the negative of the sum of the local principal curvatures of the surface [152, 153]. Therefore, it is related to the mean curvature by

$$H = -\frac{1}{2}\nabla^2 d(\mathbf{r}). \tag{B.10}$$

Using this definition of H, we can rearrange (B.9) to isolate an expression for the mean curvature. First, we note that for $C_2 = 1/\sqrt{2}\epsilon$, the coefficient $2/\epsilon - 4\epsilon{C_2}^2$ in (B.9) vanishes, giving us:

$$\frac{-1}{\sqrt{2}C_1\left[1-\tanh^2\left(\dfrac{d(\mathbf{r})}{\sqrt{2}\epsilon}\right)\right]}\frac{\delta A}{\delta\phi} = \nabla^2 d(\mathbf{r}), \tag{B.11}$$

which leads to

$$H[\phi] = \frac{1}{2\sqrt{2}C_1\left[1-\tanh^2\left(\dfrac{d(\mathbf{r})}{\sqrt{2}\epsilon}\right)\right]}\frac{\delta A}{\delta\phi}. \tag{B.12}$$

Using (B.6) and replacing $\tanh\left(d(\mathbf{r})/\sqrt{2}\epsilon\right)$ by ϕ, the final expression for H is:

$$H[\phi] = -\frac{\epsilon}{\sqrt{2}\left(1-\phi^2\right)}\left[\nabla^2\phi+\frac{1}{\epsilon^2}\phi(1-\phi^2)\right]. \tag{B.13}$$